AN EXPERIMENTAL INVESTIGATION OF THE VORTICES AND THE WAKE ASSOCIATED WITH A JET IN CROSSFLOW

A THESIS

Presented to

The Faculty of the Division of Graduate

Studies and Research

by

Dharmanshu L. Antani

In Partial Fulfillment

of the Requirements for the Degree

Doctor of Philosophy

in the School of Aerospace Engineering

Georgia Institute of Technology

August, 1977

AN EXPERIMENTAL INVESTIGATION OF THE VORTICES AND THE WAKE ASSOCIATED WITH A JET IN CROSSFLOW

Approved:

Howard M. McMahon, Chairman

Robin B. Gray

James C. Wu

Date approved by Chairman: August 11/77

ACKNOWLEDGEMENTS

I would like to sincerely thank Dr. Howard M. McMahon for his suggestion of the thesis topic and for his guidance and patience throughout the entire course of this investigation.

I am indebted to Dr. Robin B. Gray and Dr. James C. Wu for their careful reading of the original manuscript and for several invaluable discussions. I also express my thanks to Dr. P. V. Desai and Dr. W. Z. Black for their comments on the manuscript.

This investigation would not have been possible without the help of the wind tunnel staff. I am particularly indebted to Professor John J. Harper for his helpful suggestions, and to the late Mr. Hendrick R. Hudson for his guidance in the installation of the model and for operating the wind tunnel.

Mr. John Caudell helped in solving many instrumentation problems encountered during the tests. I am very grateful for his help. I also express my thanks to Mr. John Palfery, Mr. Dewey Ransom, and Mr. Harald Meyer for their aid in various phases of the experiments.

Fellow graduate students extended their assistance when needed, and I especially appreciate the help of

Mr. Ergun Oguz and Mr. R. Srinivasan.

I wish to gratefully acknowledge the financial support provided by the School of Aerospace Engineering, Georgia Institute of Technology.

My family and friends have always helped me towards achieving the successful completion of this investigation. I want to express deepest gratitude to my mother and late father who have provided encouragement throughout my education. I also want to thank my brothers for their moral and financial support. Finally, I wish to thank my wife, Vandana, for her patience and understanding.

TABLE OF CONTENTS

LIST OF TABLES

LIST OF ILLUSTRATIONS

NOMENCLATURE

a	- Radius of the Circular Jet
a_1, a_2, a_3	- Constants of Equation (7)
A	- Constant of Proportionality of Equation (19)
C	- Wing Chord, Appendix B
C_p	- Static Pressure Coefficient, $(p_s - p_\infty)/q_\infty$
C_P	- Specific Heat at Constant Pressure
C_V	- Specific Heat at Constant Volume
C_T	- Temperature Coefficient, $(T - T_\infty)/(T_j - T_\infty)$
d	- Diameter of the Circular Jet
E, E_1, E_2	- Entrainment Constants
h	- Half-Spacing between the Vortex Centers
I_{P_o}	- Integrated Total Pressure Loss
K	- Vortex Meter Constant
L	- Length of the Velocity Core for the Free Jet
m_T	- Mass Flux in the Turbulent Region of the Jet
M	- Mach Number
N	- Vortex Meter Output (Pulse Rate, Cycles/Sec)
p	- Pressure
p_a	- Ambient Pressure
p_s	- Static Pressure
P_o	- Total Pressure
$\bar{P}_o$	- Nondimensionalized Total Pressure, $(P_o - p_a)/(P_{o_\infty} - p_a)$

$P_1, P_2, \cdots, P_5$ - 5-Hole Pressure Probe Pressures

q - Dynamic Pressure

r - Radial Distance from the Vortex Center (X_v-Y_v-Z_v Coordinate System)

r' - Radial Distance from the Vortex Center (X'-Y'-Z' Coordinate System)

r_c - Vortex Core Radius

r_T - Equivalent Radius of the Turbulent Region of the Jet

R - Universal Gas Constant

R_{j_e} - Jet Exit Reynolds Number

s - Distance along the Jet Total Pressure Centerline

s_T - Distance along the Jet Temperature Centerline

t - Time

T - Total Temperature

T_s - Static Temperature

U_e - Entrainment Velocity

U_{max} - Maximum Velocity Component Parallel to the Jet Path

V - Velocity

$|\vec{V}|$ - Magnitude of Velocity Vector

X, Y, Z - Crossflow Coordinate System, Figure 12

X_v, Y_v, Z_v - Vortex Curve Coordinate System, Figure 12

X_j, Y_j, Z_j - Jet Total Pressure Centerline Coordinate System, Figure 12

X', Y', Z' - Wing Vortex Coordinate System, Appendix B

$Y_{w_{1/2}}$ - Half-Wake Width

ρ - Density

λ - Effective Velocity Ratio, $(\rho_j V_j^2 / \rho_\infty V_\infty^2)^{1/2}$

θ - Local Angle between Jet Centerline and Crossflow

θ_v - Local Angle between Vortex Curve and Crossflow

θ' - Radial Angle shown in Figure B-1

α - Upwash Flow Angle in the X-Z Plane (with Respect to the X-Axis)

Ψ - Yaw Angle of Flow in the X-Y Plane (with Respect to the X-Axis)

ω - Vorticity

β - Diffusion Constant

ν - Kinematic Viscosity

ν_T - Eddy Viscosity

Γ - Effective Strength of a Single Vortex

γ - Nondimensionalized Value of Γ, $\gamma = \Gamma/2dV_\infty$

γ' - C_P/C_V

Γ_o - Vortex Strength of a Vortex Considered as a Potential Vortex

γ_o - $\Gamma_o/2dV_\infty$

η - Frictional Efficiency of the Vortex Meter

SUBSCRIPTS

∞ - Freestream

j - Jet Exit

e - Jet Exit Plane Conditions

pl - Jet Plenum Chamber Conditions

f - Far-Field Conditions

SUMMARY

The interaction between a subsonic crossflow and a turbulent, subsonic jet which exhausts normally from a flat plate has been experimentally investigated. The primary objective of the present investigation is to study in detail the behavior of the contrarotating vortices and the wake associated with the jet in crossflow.

The tests, conducted in the Georgia Tech nine-foot low speed wind tunnel, emphasized the study of a circular jet. A preliminary investigation was also conducted for a slot-shaped jet. The effective jet to crossflow velocity ratio was kept constant at a value of eight for most of the tests.

The flow problem is first divided into two regions, the jet, which includes the contrarotating vortices, and the wake. The behavior of the jet is determined from temperature measurements which provide the extent and the shape of the jet starting from the jet exit. A vortex meter is used to make direct measurement of the vorticity distribution in the vortices. From these measurements, results are obtained providing parameters which specify the vortex location and variations in the strength and diffusion of the contrarotating vortices. The total pressure losses

in the wake are measured, along with the associated velocity distributions. The extent and shape of the wake are obtained from these data. The interactions between the vortices, the jet, and the wake are studied from the velocity and the total and static pressure measurements made near the interface of these flow-field segments.

Analysis of the results indicates that a substantial roll-up of the vortices takes place by three jet diameters travel of the jet. The core of the rolled-up vortex is of considerable size and occupies a region about three to four jet exit diameters in size on either side of the jet. Thus the contrarotating vortices are a major feature of the jet. The strength of each vortex reduces over most of the length of the jet because the vorticity field of each diffusing vortex in the pair interacts with the other. There is a wake region downstream of the jet exit which is of considerable size. The size of the wake is influenced by the velocity field associated with the vortex motion since the velocity field results in a lateral inflow of freestream fluid into the wake region. This mass flow is eventually entrained into the jet and hence increases the rate of entrainment of the jet as compared to the rate of free-jet type entrainment.

CHAPTER I

INTRODUCTION

The phenomenon of interaction between a turbulent, subsonic jet issuing from a body or a surface and a subsonic crossflow has drawn the attention of researchers for at least the last two decades. The phenomenon may occur in such different situations as the dispersion of exhaust products from a chimney stack and the cooling of combustors. The interaction is of primary importance in certain flight regimes of vertical and short take-off and landing airplanes since it causes a loss of lift and altered pitching moment characteristics during transitional flight. This problem of transitional flight associated with a jet in crossflow is the general motivation behind this investigation. Much work has been done in the past to study the resulting surface pressure distribution and the penetration of the jet in crossflow. However, it has been recognized recently that a dominant feature of the deflected jet is a pair of vortices and also that there is a considerable wake region downstream of the jet. Obtaining knowledge about these aspects of the interaction is the specific motivation behind this study.

Literature Review

References 1 and 2 are examples of research the primary purpose of which was to study the nature and magnitude of the aerodynamic interference effects of lift-jets for V/STOL airplanes of different configurations in transitional flight. The effect of a jet issuing from a wing alone into a crossflow has been studied in references 3 and 4. The motivation for these investigations was to study experimentally the lift, drag, and moment characteristics, the related pressure distributions on the surfaces of wings in the presence of the jet, and the effect of parameters such as the wing angle of attack, jet diameter, and location of the jet.

In order to simplify the complex interaction problem, initial investigations usually were studies related to a jet exhausting from a large flat surface rather than from a wing or a body. In these studies, certain factors such as the effect of surface pressure gradients, the three-dimensionality of the surface, the presence of neighbouring bodies, the wing circulation etc. are eliminated and the interaction between the jet and the crossflow can be studied without the effect of the above factors in order to achieve a basic understanding. Since the approach in the present investigation is the same, the detailed review of the literature presented here is essentially that for the jet exhausting from a flat plate. There are two major areas of research in this particular flow

problem. The first area concerns the study of surface pressures while the second is related to the investigation of the behavior of the jet itself. The present investigation is focused on the second area.

Surface Pressures

This aspect of the research is directly applicable to an understanding of losses in lift due to the jet interference.

References 5 through 9 are representative of experimental studies of surface pressure distributions on a flat plate. Surface pressures reveal regions of decelerated flow at the front of the jet, accelerated flow at the sides, and a wake behind the jet. In references 8 and 9, the shape of the jet exit was varied in combination with a variation in the effective velocity ratio, λ, defined as $(\rho_j V_j^2 / \rho_\infty V_\infty^2)^{1/2}$, to study mechanisms governing pressure distributions induced on the flat plate. Mosher[8] and other investigators concluded that the induced pressure is due to the combined effect of the jet's blockage and entrainment on the crossflow. To determine exactly how these effects arise, certain dominant features of the jet, namely, the vortices of the jet and the wake behind the jet, need to be investigated. Mosher[8] also found that for a given λ a slot jet (with the longer side parallel to the crossflow) interferes less with the crossflow than a circular jet of the same exit area. This favourable aspect can be explored

further by studying the differences in the behavior of the slot jet and the circular jet.

Oil pictures made of the flow on the surface of a flat plate given in references 8 and 9 show the presence of a region immediately behind the jet exit in which flow reversal occurs.

It is of considerable importance to be able to predict surface pressures theoretically. In order to achieve this goal, complicated interactions between the jet and the crossflow have to be understood and then modeled. Although there are not sufficient data available to describe the whole flow field and thus to accurately model the flow, a few models have been developed in which the jet is represented by potential flow elements. Examples are found in references 10 through 13. Most of these investigators (References 10 through 12) made use of a blockage-sink model to represent the jet interference. Reference 13 is an example of investigations in which the jet was replaced by vorticity elements to induce surface pressures.

Potential flow models cannot predict surface pressure distributions adequately in the wake region where the action of viscosity cannot be neglected, and these models are usually restricted to the prediction of the surface pressures outside the wake region. Moreover, Wright[10] noted that the blockage effect of the wake region can be simulated in a

potential flow model by placing an afterbody behind the jet exit. In order to accurately model the actual effect of the wake region on the surface pressure and on the flow field near the wake region, one needs to have data which describe the extent of the wake, the severity of the total pressure defect, and the influence on the wake of the flow field associated with the contrarotating vortices.

Jet

The second major area of research in the interaction problem concerns the behavior of the jet itself, together with the surrounding flow fields including the wake. Certain facts pertaining to the behavior of the jet have already been recognized. It is known that the jet, after it exhausts normally to the crossflow, deflects, increases in lateral size, distorts in shape, and evolves eventually into a flow field of which the dominatant feature is a pair of contra-rotating vortices. Some of these facts are known only in a qualitative manner from experiments using flow visualization. Figure 1 is a schematic diagram which shows different regions of the jet and the wake region.

The location of the centerline of the circular jet has been studied extensively. References 14 through 16 are examples of earlier experimental work which shed light on the importance of the velocity ratio, V_j/V_∞, as a primary parameter influencing penetration of the jet. Reference 17

describes recent tests of two circular jets which issue normally to the crossflow. The penetration of a circular jet issuing at various angles to the crossflow is reported in references 18 and 19 while references 8 and 20 cover the penetration of non-circular jets. It was found that a less bluff jet penetrates more than a circular jet of the same exit area.

One of the first quantitative studies of the behavior of a circular jet in crossflow was made by Jordinson[21] who conducted experiments to obtain total pressure distributions at various cross sections of the flow field. This investigation, along with the determination of the overall penetration of the jet, showed the deformation of the jet cross section from circular at the exit to a "kidney" shape downstream of the exit. Jordinson concluded that the pressure difference across the jet is mainly responsible for the initial deflection of the jet but that the entrainment of the crossflow fluid into the jet is the predominant mechanism which further deflects the jet after the first few diameters of jet travel. He also argued that the deformation of the jet cross section can be explained by considering that the mixing of the crossflow on the sides of the jet leads to regions of mixed fluid which move downstream more quickly than the central region of the core, which remains unaffected initially. Thus far, no data are available in the literature which show the development of the deformed regions very near

the jet exit. Similar measurements were made by Gordier[22] in a water tunnel for water jets and jets composed of an air-water mixture. His flow visualization experiments using dye released on the surface revealed a blockage effect of the jet on the crossflow and the entrainment of crossflow fluid into the jet behind the jet exit. The distortion in the shape of a hot circular jet in crossflow was deduced from temperature measurements by Kamotani and Greber[23]. They also concluded that the jet centerline location (based on measured maximum velocity points in the plane of symmetry) is determined solely by the effective velocity ratio, λ, which represents the jet to crossflow momentum ratio. More importantly, reference 23 states that the location of the temperature centerlines (based on measured maximum temperature points in the plane of symmetry) depends on both λ and the density ratio, ρ_j/ρ_∞, and that the temperature centerline penetrates less than the jet centerline for a constant λ in the case of hot jets. No temperature measurements are shown very near the jet exit in reference 23, which would have indicated the rolling up of the contrarotating vortices.

There are no quantitative measurements available in the literature describing the deformation of non-circular jets. The only available investigations are those of Reilly[24] and Mosher[8] who did smoke studies to obtain the deformation of elliptical jets. However, these studies are either limited to laminar jets or the actual visualization

is poor in the case of turbulent jets.

In the process of investigating the deformation of the circular jet, Jordinson[21] and Gordier[22] both noted a region behind the jet in which there were losses in the total pressure. The extent of this wake region can be seen in the total pressure contours of reference 21. However, it is difficult to infer the distinct, three-dimensional shape of the wake region between the flat plate surface and the jet. Moreover, there is a need to know the influence of the flow fields associated with the wake and the vortices on each other.

One of the most significant features of the deflected jet is the presence of the contrarotating vortices in the jet. Although the formation and the subsequent behavior of these vortices is not yet well understood, the deformation of the jet is attributed to the rolling up of these vortices[21]. Crawford[25] proposed a combined potential and momentum roll-up model of the jet in crossflow which can be used to predict the circulation of the vortices in their zone of development and decay. Pratte and Baines[26] argued that the strength of the vortices does not decrease in the zone of maximum deflection which is defined in reference 26 as $0 \leq X/d \leq 25$ downstream of the jet exit for $\lambda = 8$. However, this argument was based only on observations from smoke studies and lacks a quantitative foundation.

Some investigations have been made in order to give

a quantitative description of the vortices. Almost all the investigations (References 27 through 31) infer the strength of the vortices from velocity measurements. Margason and Fearn[32] measured the strength by obtaining vorticity distributions using a spinner-type vortex meter. These spinner measurements were preliminary in nature but showed the feasibility of using the vortex meter for the direct measurement of the vortices in the jet in cross-flow. No variation in the behavior of the vortices was obtained; the vortex strength was measured at one axial location for $\lambda = 4$.

The rest of the investigations (References 27 through 31) all required velocity measurements. Tipping[27] obtained the strength of the vortices at one axial location for $\lambda = 6.7$ and $\lambda = 10$ by using a claw-probe. Endo[28] determined the doublet strength of the contrarotating vortices by obtaining distributions of the streamwise component of vorticity from measured velocity vectors in cross sectional planes normal to the jet path.

Thompson[29] calculated the variation in the strength of the vortices along their path by measuring velocity vectors in a cross section normal to the vortex path and then using two methods to estimate the vortex strength. In the first method, the assumption was needed that the individual vortices are discrete and quasi two-dimensional; the circulation then was evaluated from the measured

circumferential velocity distribution for a single traverse through the vortex center. Variations in the vortex strength along the path were obtained by this method for λ = 2, 4, and 8. In the second method, the circulation was evaluated at one axial station for each λ by contour intergration of the tangential component of velocity around circuits of increasing size enclosing the vortex centers. The second method was more time consuming and therefore was used only as a spot check of the values obtained by the first method. Although the vortex strength can be measured accurately using the second method, details such as the distribution of the vorticity, the rate of diffusion of the vortices, etc. cannot be obtained. In general, the data of reference 29 showed that in the regions where measurements were made (for λ = 8, from X/a = 14 downstream), the strength of the vortices reduces along the vortex path for the range of λ (2, 4, and 8) covered. The data showed a reasonably good agreement with the vortex strength values reported in references 27 and 32.

Fearn and Weston[30] developed two vortex models which predict the location, the strength, and the diffusivity of the contrarotating vortices. In the first model, called the vortex filament model, the vortices in a cross section are replaced by a pair of two-dimensional potential vortices of an unknown strength and spacing, located on either side of the plane of symmetry (Y = 0). The values of the two unknowns are calculated by fitting the measured upwash

velocity components (taken on the line of symmetry of the cross section) with the velocity field induced by the filament vortices using the method of least squares. It is assumed that the component of freestream velocity in the plane of the cross section should be superimposed on the induced velocity field of the vortices. The second model of reference 30, called the diffuse vortex model, involves the same assumptions necessary for the filament model except that the vortices are considered as viscous and the vorticity distribution for each vortex is assumed to be Gaussian before the vortices interact. The core radius of the vortex is an additional unknown for this model, and upwash velocity data over the entire cross section are used to calculate the vortex strength, spacing, and core radius. One of the important assumptions involved in both the models is that the jet spread and the presence of the wake have a negligible effect on the velocity field. The discrepancy between the measured vortex strength values of Thompson[29] and the predicted values of reference 30 is not insignificant. A good check of the models of reference 30 can be made by obtaining direct measurements of the vortex strength and the core radius.

In reference 30, vortex strength distributions were obtained over a range of λ (3 to 10) using the two models proposed. One of the important conclusions of reference 30 is that, for the diffuse model, the strength of each vortex, before the mutual interactions begin, increases linearly

with λ. The data and the models from reference 30 were used by Sellers[31] to make a more thorough analysis of the models, and certain finer points were investigated.

The description of the overall behavior of the jet which can be obtained from the literature has been used by other investigators to formulate an analytical framework for the flow phenomenon. Crow and Riesebieter[33] used the drag as the only force causing the bending of the jet, whereas Keffer and Baines[34] and McAllister[35] used the entrainment as the primary mechanism. The process of entrainment of the crossflow fluid into the jet is not yet completely understood. In the case of free jets, entrainment occurs only by the spreading of the turbulent front. In the present case, the entrainment process is augmented considerably by the crossflow. Keffer and Baines[34] computed the entrainment rate from velocity measurements and used the information to derive an expression for the bending of the jet. References 18, 23, and 28 show that the entrainment in the jet in crossflow can be divided into two parts. The first part is due to a free-jet type of entrainment and the second part is considered to be due to the effect of the crossflow component normal to the jet path. In reference 18, it is argued that the physical mechanism underlying the second part is the pair of contrarotating vortices which sweep the freestream fluid into the jet. However, there have been no quantitative data to support the latter

hypothesis. There are other investigations in which the additional entrainment of the jet in crossflow is attributed to different causes. Fan[36] suggested that there is an additional entrainment of the jet because of the static pressure differences around the jet. Butkewicz[37] used a vortex street wake model for entrainment of the crossflow into the jet. Thus, there is a lack of agreement as to the physical mechanism causing the entrainment of the jet in crossflow.

The literature surveyed above demonstrates a need for a detailed study of the contrarotating vortices and the wake and their effect on the behavior of the jet. More experimental information is needed regarding the quantitative description of the vortices through direct measurement, the deformation of the jet near the jet exit, and the character and extent of the wake region. Furthermore, the effect of the shape of the jet exit on the behavior of the jet in crossflow merits further study.

Research Objectives and Scope

The primary research objective of the present investigation is to study in detail the behavior of the contrarotating vortices associated with a subsonic, turbulent, circular jet which exhausts from a flat plate in a subsonic flow. The formation of the pair of contrarotating vortices is of great importance because the associated circulatory

flow is the dominant feature of the flow field of the jet and the surrounding medium. Earlier investigations have examined the properties of the vortices in an indirect manner, either by obtaining the variation in circulation around a circuit enclosing the vortex center or by formulating vortex models which predict the vortex behavior based upon velocity measurements. The aim of this work is to study the vortices by direct measurement. This is accomplished by making use of a vortex meter to make measurements of the vorticity distribution. From these measurements, results are obtained which provide parameters specifying the vortex location and the variation in the strength and diffusion of the contrarotating vortices. It is hoped that these direct measurements will form a basis of comparison for future vortex models.

Because the contrarotating vortices are the dominant feature of the jet, a second major objective is to study the interactions between the vortices, the jet, and the wake. This is achieved by studying the qualitative and quantitative behavior of the jet and the wake. Thus, the present investigation begins by examining the behavior of the circular jet in terms of temperature fields which describe the extent and the shape of the jet and thus delineate the regions of the jet and the wake. The deformation of the circular jet very near the jet exit is also found so as to qualitatively picture the process of the rolling up of the

vortices. After obtaining the extent of the jet and studying the contrarotating vortices, the variation in the shape and size of the wake behind the circular jet and the associated velocity field and total pressure losses in the wake are determined in order to study the effect of the flow field associated with the vortices on the wake region. As a final step of the study of the interaction between the vortices, the jet, and the wake, flow-field data are obtained near the interface of these flow-field segments.

The quantitative behavior of the flow field very near the jet exit and in the very far field downstream region are not investigated in detail in the present study because of limitations in the measurement techniques employed. The literature also lacks specific measurements in these regions. However, some concepts have been put forward by different investigators. These ideas are explored further at the end of this study and synthesized by the writer with the data obtained in the present study in order to offer an overall physical picture of the flow field.

The present investigation is essentially for a circular jet in crossflow. However, some preliminary data are also obtained regarding the behavior of the streamlined jet.

The experimental set-up used in the present investigation is the same as that used by Mosher[8] and is described in the next chapter.

Except for a few cases, the experiments were limited to one particular value of the effective velocity ratio, namely eight, because of the availability of supporting data in the literature for that case.

CHAPTER II

EQUIPMENT AND INSTRUMENTATION

The experimental set-up described in this chapter consists of a jet which exhausts at right angles to the surface of a flat plate mounted in a wind tunnel. A description is also given of the probes and associated instrumentation required to measure the flow field.

Wind Tunnel

The crossflow was provided by the uniform free-stream of the Georgia Tech nine-foot wind tunnel. The wind tunnel is a single return, closed-throat, atmospheric type with a test section velocity continuously variable from 0 to approximately 160 mph. The test section has a length of 12 feet and a circular cross section nine feet in diameter. The turbulence factor of the wind tunnel is 1.2. An over-all sketch of the set-up is given in Figure 2.

Air Supply

The compressed air for the jet was supplied by a 100 H.P. centrifugal blower. A description of the blower performance and accessories is given in reference 8. The velocity of the jet was controlled by a butterfly valve. Before exhausting from the jet exit, the flow passed

through three screens and then entered a short supply pipe to the jet nozzle. The temperature of the air in the jet exit was approximately 170°F when the equilibrium condition was reached.

Flat Plate and Nozzles

The jet exhausted vertically upwards from the flat plate through the nozzle exit. Figure 3 shows a photograph of the nozzle exit and the flat plate. The plate is 48 inches x 66 inches in the chordwise and spanwise direction respectively, and is made from 0.375 inch thick aluminium. The leading edge of the flat plate is rounded to prevent seperation of the crossflow at the edge. The plate was installed so as to almost span the test section, with its center at a height of approximately 13 inches above the floor of the wind tunnel, and was supported by eight legs which could be adjusted to align the plate with the free-stream as required. In the present tests, the plate was set at approximately -1° (leading edge down) relative to the tunnel floor to obtain data comparable to that in reference 8. Mosher[8] found that this orientation produces a uniform pressure distribution on the plate. The turbulent boundary layer is approximately 1.0 inch thick at the middle of the plate.

The center 7.0 inch diameter of the flat plate is occupied by the jet nozzle and flange, which together

constitute the "nozzle block". The nozzle block is set flush with the flat plate and is fastened to the supply pipe with screws. Two different nozzle exit shapes, having the same exit area, were used in these experiments. Figure 4 gives the details of both of the exit shapes. Configuration (a) will be referred to as the "circular" jet and configuration (b) will be referred to as the "streamlined" jet. The detailed design of these nozzles is given in Appendix A of reference 8.

Actuator

The actuator serves the two-fold purpose of supporting any probe used and of positioning the probe in the flow field by means of remote control. Figure 5 gives a view of the actuator as installed in the test section. The distance from the vertical actuator guides to the center of the jet exit is 18 inches. A probe, held on a probe holder, can be traversed by remote control over an area of five feet by five feet in the X-Z plane. In the vertical direction, the probe holder cannot come closer than four inches to the surface of the plate because of the presence of the bottom support for the vertical guides. The actuator system also has the ability to rotate the probe about its longitudinal axis and hence change the pitch angle of the probe by 360^{o}. This degree of freedom is also controlled remotely. Changes of the probe position in the

Y direction are made manually.

Figure 6 shows the control panel for the actuator. Three toggle switches activate d.c. motors which drive the lead screws. The three read-out counters are driven by selsyn motors which are electrically coupled with the d.c. motors on the actuator. The resolution of the counters is different for all three remotely-controlled motions. Because different gearing is involved, the counters display 123 counts for one inch of travel in the X direction and 154 counts for one inch of travel in the Z direction. The rotary gear train provides 1 count for every 1^{o} change in the pitch angle. The selsyn motors for the counters require a 115 V, 400 cycle power supply which is provided by an auxiliary alternator in the wind tunnel room. The actuator repeatability was within ± 0.05 inch in X and Z, and ± 0.5^{o} in pitch angle.

Probes and Instrumentation

Kiel Probe Rake

Total pressure measurements above the plate surface in the wake region were made with Kiel probes mounted in the form of a rake. The rake consists of five Kiel probes hanging vertically from a wooden airfoil-section fairing of span 2.5 inches, as shown in Figure 7. The spacing between the probes is 0.5 inch and, when the rake is mounted on the actuator, the probes can touch the surface of the flat plate.

The Kiel probes are type KA, miniature style, with an outside diameter of 0.063 inch at the measuring end. These probes are made by United Sensor and Control Corp. According to the manufacturer, the total pressure as measured by the Kiel probes is insensitive to pitch angle in the range of $+47^{o}$ to -40^{o} and to yaw angle in the range of $\pm 52^{o}$ at a Mach number of 0.25.

The Kiel probe rake was mounted on the probe holder of the actuator and five vinyl leads (0.063 inch internal diameter) were connected to a scanivalve (Model 48J4, Scanivalve Corp., San Diego, California) located outside the tunnel. A pressure of 10 inches mercury below atmospheric was maintained in the scanivalve case to minimize oil migration into the interface between the rotor and stator.

Each Kiel probe pressure was read in turn by switching the scanivalve ports. The stepping of the scanivalve was accomplished by a solenoid controller (Scanivalve Corp., Model CTLR2/5xS4) (Fig.6) which was controlled by a Hewlett-Packard Automated Data Aquisition System based upon a Model 2114 B Computer with 8k memory. The pressure transducer used was a type 511 Barocel transducer (CGS, Datametric Inc., Waltham, Mass.), variable capacitance type, with a maximum differential range of 10 mm mercury. The Kiel probe pressures were read as a differential from the ambient pressure. The

pressure differentials sensed by the transducer were measured by a Barocel Electronic Manometer System consisting of a type 700 power supply and a Model 1015-S2 signal conditioner. The analog voltage signals from the signal conditioner were digitized by a Hewlett-Packard Model 2401 C Integrating Digital Voltmeter and fed into the memory of the computer. The calibration of the pressure measurement system is discussed in the next chapter.

5-Hole Pressure Probe

Velocity measurements above the flat plate surface were made with a three-dimensional probe which has five pressure sensing holes. The pressure measurements taken with this probe yield, through calibration curves, the dynamic head, total pressure, static pressure, pitch angle ($0^{\circ} \leq \alpha \leq 360^{\circ}$), and yaw angle ($-40^{\circ} \leq \Psi \leq 40^{\circ}$) of the local flow. The procedure is given in detail in the next chapter. The measuring portion of the probe is prism shaped as shown in Figure 8. The probe, type DA-250, manufactured by United Sensor and Control Corporation of Watertown, Mass., is made of 0.25 inch outside diameter stainless steel tube. The locations of the five holes are shown in the figure. The region of the flow field over which a single data point is obtained is about 1/64 of a square inch. The probe is 24 inches in overall length and it was cantilevered through a 0.25 inch diameter hole in the probe holder of the

actuator.

The pressure switching mechanism employed for the 5-hole probe was different than the one used for the Kiel probe rake because of the necessity of measuring certain pressure difference values across the probe measuring taps. The switching mechanism has a bank of four Model W1/2P-6T Scanivalve wafer switches. These wafer switches require the application of a back pressure which must be greater than any of the pressures being measured in order to keep adjacent moving surfaces sealed. This back pressure was set at a value of 10 psi in the experiments. The function of the first wafer switch in the pressure switiching mechanism is to provide four pre-selected differentials from the five probe pressures and the ambient pressure. This is achieved in steps by activating a push button on a control box. The control box has four channels and each channel operates an individual solenoid drive for each of the four wafer switches. Two pressure transducers of different capacity can be used to cover the range of pressure differentials encountered in the flow field. The second wafer module provides the ability to switch a pre-selected pressure differential reading to either of these pressure transducers. In the experiments, most of the pressure differentials were read by the same pressure transducer (Type 511 Barocel) used for the Kiel probe rake, but a type 501

Barocel transducers of 1000 mm mercury range was used to locate the jet centerline. Since the transducers were calibrated with higher pressure always on one particular side of the diaphragm in the transducer, hence giving positive voltage output, it is desirable to make measurements of pressure differentials such that the transducer is always operated in the same condition. For situations in which the differential input has a negative sign, the third wafer switch swaps the pressure on either side of the transducer, thus giving positive voltage output. The function of the fourth wafer in the bank is to make it convenient to rapidly check the zero of the transducer by dead-ending its input ports.

The output of the transducer was read by the Model 2401 C Intergrating Digital Voltmeter through the Model 1015-S2 signal conditioner and was recorded by the Hewlett-Packard Automated Data Aquisition System.

Thermocouple Probes

Temperature measurements in the flow field were made with a thermocouple probe. The probe was made of Chromel-Alumel thermocouple wires (Leeds and Northrup Co.) fused together to form a spherical tip of 0.04 inch diameter. The dimensions of the probe are given in Figure 9. The probe was supported by the actuator probe holder. Two other thermocouple probes were made in the same manner.

One of these probes was inserted about 2.5 inches through the tunnel wall into the freestream to measure the tunnel freestream temperature, T_∞. A second probe was inserted 0.5 inch into the jet plenum chamber to measure the jet stagnation temperature, T_j.

Thermocouple wires of all the three probes on the "cold" junction end were connected to a 12 channel Thermocouple Reference Junction (Model BRJ R13-12 TP-1531) manufactured by Pace Engineering Company, North Hollywood, California. This reference junction provides a precisely controlled stable temperature reference (150^{o}F), eliminating the necessity for cold-junction compensation and ice bath maintenance. For this reference junction temperature, the output of the Chromel-Alumel thermocouple is 0.0225 mv per degree F based on National Bureau of Standards tables. During measurement of the local temperatures in the jet, the thermocouple output was recorded on a Hewlett-Packard (Model 7001 A) X-Y plotter. The variations in T_∞ and T_j were recorded on a 2-channel Hewlett-Packard strip chart recorder (Model 770 2B). The next chapter discusses temperature measurement procedure and accuracy.

Vortex Meter

A "spinner" type vortex meter (Figure 10) was used to determine experimentally the strength of the rolled-up vortices. The vortex meter is manufactured by

Aero Engineering Associates, Inc., State College, Pennsylvania and is designed to measure mean flow vorticity in an airflow. The vortex meter consists of a spinner which has four unpitched blades set parallel to the axis of the vortex meter. The diameter of the spinner (tip to tip across the blades) is 0.378 inch. The spinner is press-fitted to a hardened steel shaft of varying diameter. This shaft is supported by two sapphire jewel bearings while fore and aft shaft movement is restricted by a flat cap jewel set into a rear adjustable plug. The bearings are set within a brass body which is enclosed by a cover of 0.5 inch outside diameter. The overall length of the meter is approximately 3.5 inches.

The meter is supplied with a calibrating device as shown in Figure 11. This device consists of a set of pitched blades which, when positioned ahead of the spinner, impart a known rotation to the flow. The calibrating device also serves as a protective cage for the meter when not in use. The next chapter discusses the use of the calibrating device and reliability checks performed on the instrument.

A miniature light bulb set on one side of a transparent segment of the shaft of the meter, with a photocell on the other side, provide a means of measuring the rate of rotation of the spinner. The bulb is powered

by a 4.5 volt battery and, when the hole in the shaft is in line with the bulb and the photocell, the light passing through the hole causes the photocell to generate current. The photocell thus provides two output pulses per revolution of the shaft. In the experiments, the pulses were first amplified by a Dynamics Differential Amplifier (Model 7514 B), then passed through a Kron-Hite Filter (Model 3203 R) and counted by a General Radio Counter (Model 1192-B). A Textronix (Type 502 A) Dual Beam Oscilloscope was used to display the quality of the pulses coming from the spinner both before amplification and after passing through the filter.

A more detailed description concerning the use of the vortex meter and the design aspects for the probe support are given in Appendix A. This Appendix also contains discussion regarding typical problems encountered during handling and lubrication of the vortex meter as well as details regarding the settings of the instruments.

CHAPTER III

TESTING PROCEDURE

General

The present experimental investigation is primarily for one particular value of the effective velocity ratio, λ. The value $\lambda = 8$ is that most frequently appearing in the literature, and, therefore, it was chosen for the majority of the tests so as to allow comparison with other investigations. In addition to this primary case, data were obtained for $\lambda \simeq 4$, 10.7, and 12.

The penetration, deflection, spread, and deformation of the circular jet in crossflow were studied by measuring temperature distribution using thermocouples. Similar measurements were also made for the streamlined jet to examine changes in these quantities with jet exit geometry. Pressure and vortex meter measurements were made only for the circular jet case.

It was assumed throughout the investigation that the flow field is symmetric about the $Y = 0$ plane, so that measurements were made only in the region $Y \geq 0$. It can be seen from the measurements of other investigations (e.g. references 21 and 30) that the assumption is valid. Velocity component data taken during this investigation also

supported this assumption.

Figure 12 shows the coordinate systems used. The jet centerline and the vortex curve both lie in the plane of symmetry (Y = 0), therefore, $Y = Y_j = Y_v$.

Test Conditions

Freestream

All the tests were run at V_∞ = 50 fps. The freestream velocity was monitored on a Betz water manometer (reading uncertainty of ± 0.03 mm H_2O) in terms of the freestream dynamic pressure, i.e.

$$q_\infty = \frac{1}{2} \rho_a V_\infty^2$$

where ρ_a is the ambient density. Ambient pressure, p_a, was read on an aneroid barometer and ambient temperature, T_a, was read on a standard mercury thermometer.

Quality of Freestream Flow. The freestream flow around the plate had been investigated previously by Mosher[8] and found to be satisfactory for the same plate location.

For the jet-off case, the thickness of the boundary layer on the flat plate was measured in the present tests using the Kiel probe rake and was found to vary from approximately one inch at X/a = 0 to 1.5 inches at X/a = 22. The turbulent boundary layer had a typical 1/7 power velocity

profile. The Kiel probe data showed about one percent variation in the total pressure in the freestream regions outside the boundary layer. No adverse effect of the presence of the actuator was noticed in the total pressure data obtained in the lateral region from Y/a = 0 to 7. No attempt was otherwise made to investigate the interference effect of the actuator on the freestream flow. For an actuator of a slightly smaller dimensions, Mosher[8] found that V_∞ varied by 1.5% and the yaw angle, Ψ, changed by 0.5° over the range from Y/a = 0 to 8.

In the present investigation, the freestream velocity was held within ± 0.5% of setting on the Betz manometer. Measurements of the freestream flow vector, made by the 5-hole pressure probe near the tunnel centerline, showed V_∞ to be within 1% of the value set, with flow angularity of about 1° in yaw and pitch.

Jet

As mentioned in the previous chapter, a butterfly valve controls the exit conditions of the jet by varying the plenum chamber pressure, $P_{o_{pl}}$. It is necessary to relate the desired effective velocity ratio, λ, and the freestream dynamic pressure, q_∞, to the plenum chamber pressure. This was done by using the relations for isentropic compressible flow as shown in reference 8. The resulting expression is

$$P_{o_e} - p_a = p_a \left\{ \left(1 + \frac{\lambda^2 q_\infty}{3.5\ p_a} \right)^{7/2} - 1 \right\}$$

where p_a is the ambient pressure and $q_{j_e} = \lambda^2 q_\infty$. In deriving the above expression, it was assumed that air is a perfect gas and that the static pressure at the jet exit is equal to the ambient pressure, p_a. (With the wind tunnel being an atmospheric type, $p_\infty \simeq p_a$.) In the tests under crossflow conditions, instead of $(P_{o_e} - p_a)$, the difference $(P_{o_{pl}} - p_a)$ was monitored on a mercury manometer. The difference between $P_{o_{pl}}$ and P_{o_e} was determined experimentally by Mosher[8] under free-jet conditions and the appropriate corrections were made in the expression for $(P_{o_e} - p_a)$. The value of $(P_{o_{pl}} - p_a)$, for any λ, used in the present investigation was the same as that used in reference 8. It took about 20 minutes for the plenum chamber temperature to stabilize and hence no data were taken during that period. After this, very small adjustments (± 0.005 inch mercury) were required to maintain a constant P_{o_e}.

In the present investigation, q_∞ was based on ambient conditions rather than on standard sea level conditions as used by Mosher[8]. This difference makes about 2% difference in the λ values used in the present investigation when compared with those of reference 8. Table 1 lists values of the true effective velocity ratio of the

present investigation compared to the nominal effective velocity ratio values of Mosher[8]. In the text of this work, the value of λ mentioned is the nominal value as a matter of convenience. However, the precise values are indicated in the figures. Table 1 also lists the jet exit velocity, V_{j_e}, values for different cases and the jet Reynolds number, R_{j_e} ($= V_{j_e} d/\nu$). The freestream Reynolds number, based on the jet diameter, was 0.5×10^5.

Figure 13 compares the jet centerline location obtained in the present investigation with the jet centerline of reference 8 for $\lambda = 8$. The jet centerline is defined as the locus of points of maximum total pressure in the plane of symmetry ($Y/a = 0$). The total pressure values were obtained using the 5-hole pressure probe in the present investigation and in reference 8. The figure shows that the slight difference in the value of λ does not affect the penetration of the jet.

Quality of Free Jet

The shape of the velocity profile at the jet exit was investigated by Mosher[8] for both the circular and streamlined jets and was found to be uniform within one percent in total pressure and within two percent in static pressure. In the present investigation, some sample total pressure profiles and free jet decay characteristics were obtained. The total pressure was measured with a 0.028 inch outside

diameter pitot tube. The jet dynamic pressure, q_j, was calculated from these data assuming that the static pressure at the jet exit equals the ambient pressure. Figure 14 is representative of the q_j profiles thus obtained. Figure 15 shows the decay characteristics of the circular jet along its length when operated as a free jet (i.e. $V_\infty = 0$). The distance along the jet centerline where the velocity has decayed by one percent of the exit value is defined as the length of the core, L. The value of L obtained in the present tests was 3.75 times the diameter of the jet ($L/d = 3.75$) for a Reynolds number of 3×10^5 based on the jet diameter. Comparison is made in Figure 15 with the decay characteristics of the jet used by Thompson[29]. In Chapter IV, results of the present investigation are compared with that of reference 29. Therefore, the intention here was to explore any possible differences in the quality of the two jets used. The jet Reynolds number reported in reference 29 was about one-half the value of R_{j_e} in the present tests and hence the jet decay was a little faster in the present case. Kamotani and Greber[23] also reported a core length (L/d) value of approximately 4 for a jet Reynolds number of approximately 0.25×10^5, with a turbulence intensity at the jet exit of about 0.2%.

Measurements, Calibration, and Accuracies

Thermocouples

Temperature measurements were made in the jet in crossflow for jet exit shapes having circular and streamlined profiles. The data obtained were used to get the extent and shape of the jets. The measurements were made in vertical planes for both of the jets at $\lambda = 8$. The Y-Z planes taken were at $X/a = 4, 7, 11, 15$ and 22 for the circular jet and at $X/a = 4, 7$, and 15 for the streamlined jet. Measurements were also made in the plane of symmetry for both the jets. Similar data were also taken in the case of the circular jet for $\lambda = 4$ and 12. In addition, traverses were made near the exit of the circular jet in order to obtain the behavior of the jet in that region.

The output of the thermocouples used to measure the local temperature (T), jet plenum temperature (T_j), and freestream temperature (T_∞) were checked at room temperature and at the temperature of boiling water. The National Bureau of Standards tables were used to convert voltages to temperature values. The agreement was good within the reading uncertainty ($\pm$ 0.5°F) of the thermometers used as a reference.

In the experiments, T was recorded on the X-Y plotter by starting the plotter and the probe traversing gear simultaneously. Because of the relatively fast response

of the thermocouple, this procedure should not lead to measurement errors greater than ± 1^{o}F. Any non-linearity in the actuator precision lead screw and the X-Y plotter should be small. It took a minimum of five seconds for the thermocouple to travel one inch.

Temperature measurement errors may arise because of compressibility. However, the errors are small (± 0.25% of the temperature value) for the maximum Mach number of 0.36 in the present case. Repeatability of the data was good (within ± 2^{o}F). It is estimated that the C_T contours are accurate within C_T = ± 0.02.

Kiel Probe Rake

The purpose of the Kiel probe rake measurements was to obtain the three-dimensional extent of the wake region. The half-width of the wake here is defined as the value of Y/a (lateral distance from the plane of symmetry, Y/a = 0) at any X/a and Z/a where the flow has recovered 99% of the freestream total pressure. The procedure followed was to first measure P_{o_∞}, using the Kiel probes, at points in the wake region with the jet-off and then to measure distributions of the local total pressure, P_o, along lines Z = constant for the jet-on case for any X station. Values of $\Delta P_o/P_{o_\infty}$, where $\Delta P_o = P_o - P_{o_\infty}$, were plotted as a function of Y/a for any X/a and Z/a. From these plots, the half-width of the wake was obtained by locating the points where

the total pressure came within one percent of the freestream value.

The Kiel probe rake measurements were made for the circular jet at λ values of 8 and 10.7. The measurements were made in the Y-Z plane at X/a locations of 7, 11, 15, and 22. The measurements were restricted to regions where no jet fluid had been found on the basis of the thermocouple measurements.

Before the experiments were conducted, the pressure measurement system was checked for leaks by individually pressurizing the pressure lines to nearly the maximum capacity of the pressure transducer; the pressure decay due to leakage then was monitored on a digital voltmeter. The pressure decay was found to be less than 0.1 percent of reading per minute in all cases and therefore the leakage rate was considered to be negligible. The 10 mm mercury Barocel transducers used to obtain the total pressure values were calibrated using a dead weight tester (Consolidated Electrodynamics Corporation, type 6-201-0001) which is accurate to within 0.025 percent of reading. It was found that the calibration substantiated the manufacturer's stated accuracy of from 0.1 to 0.25 percent of reading.

In the experiments, a sample period of one second was used for the Integrating Digital Voltmeter of the Data Aquisition System. Ten such integrated values were sampled

by the computer and the print-out was in the form of the average total pressure together with the maximum and minimum values out of the ten samples.

Figure 16 shows a typical distribution of average values of $\Delta P_o/P_{o_\infty}$ together with fluctuation bands determined from the maximum and minimum of the sampled values of P_o. It was estimated that the maximum uncertainty, because of fluctuations in P_o, in obtaining the half-width of the wake is $\pm$ 0.25a. Data taken later by the 5-hole pressure probe confirmed that, within the wake regions surveyed, the Kiel probes were not subjected to flows with yaw or pitch angles beyond their range of insensitivity.

According to the manufacturer, errors in total pressure measurement due to turbulence is much less for Kiel probes than for conventional pitot probes. However, large turbulence may cut down the yaw- and pitch-insensitive ranges. No attempt has been made to make turbulence intensity corrections in the data because of the lack of quantitative information concerning the turbulence intensities in the present flow problem.

5-Hole Pressure Probe

The 5-hole pressure probe was used to obtain velocity and pressure measurements for the circular jet at $\lambda = 8$. Data were obtained in vertical Y-Z planes at X/a values of 11 and 15. The area covered extended from

(a) yaw angle coefficient, $(P_4 - P_5)/(P_1 - P_2)$, versus Ψ;
(b) dynamic pressure coefficient, $q/(P_1 - P_2)$, versus Ψ; and
(c) total pressure coefficient, $(P_1 - P_o)/q$, versus Ψ.
The dynamic pressure coefficient is somewhat sensitive to Mach number due to compressibility effects. Therefore three sets of curves were obtained for freestream velocities of 50, 70, and 110 fps yielding a Mach number, M, of 0.044, 0.062, and 0.098 respectively. Figure 17 shows a set of calibration curves for M = 0.098. Although the three curves for all three Mach numbers were generated, only Figure 17(b) is shown with the calibration curves for M = 0.098 and M = 0.042 since the effect of Mach number on curves (a) and (c) is very small. Repeatability of the calibration was checked and found to be within ± 1.0%.

In the experiments, the value of α was obtained by nulling and then values of the differentials $(P_4 - P_5)$, $(P_1 - P_2)$, and $(P_1 - p_a)$ were read by the automated pressure measurement system described in the previous chapter. The computer printed out average and maximum and minimum values (for 10 samples, each sample being integrated over 1 second) of the differentials. The data reduction to obtain Ψ, q, and P_o (from the calibration curves) was accomplished on the UNIVAC 1108 computer. Knowing Ψ, α, and q, velocity components were calculated in both the X-Y-Z and X_v-Y_v-Z_v coordinate systems. Static pressure, p_s, values were calculated from q and P_o.

The uncertainty in nulling to get α was $\pm 0.5^{o}$ and the pitch angle was repeatable within the limits of uncertainty. The data reduction revealed maximum fluctuations in Ψ of $\pm 3^{o}$ due to flow unsteadiness. However, the repeatability of the yaw angle data was within $\pm 2^{o}$. Figure 18 illustrates the maximum velocity fluctuations encountered and the repeatability attained in a typical traverse. It is estimated that the maximum error in measuring $|\vec{V}|$ was about $\pm$ 2.5 percent of the measured value. The repeatability of the velocity data was within $\pm$ 2 percent of the measured value, which, on the average, would be about $\pm$ 1.5 fps. Errors in the absolute value of P_o are estimated to be about $\pm$ 0.5 percent of the measured value. The repeatability in the measurement of $(P_o - P_{o_\infty})$, was $\pm$ 0.03 mm Hg, i.e. $\pm$ 2 percent of the measured value of $(P_o - P_{o_\infty})$. Although static pressure values were repeatable within $\pm$ 8 percent in the quantity $(p_s - p_{s_\infty})$ (which would mean only $\pm$ 1% of the absolute value of p_s), it is difficult to estimate the maximum uncertainty because of the turbulence intensity corrections. The relationship between mean quantities P_o, p_s, and $|\vec{V}|$ with the turbulence intensity (T.I.) can be expressed[23], for isotropic turbulence, as

$$P_o \simeq p_s + \rho \{ 1 + 3 (T.I.)^2 \} \frac{|\vec{V}|^2}{2} .$$

Kamotani and Greber[23] reported that, for $\lambda = 8$, a maximum turbulence intensity of 20% of the maximum velocity for the cross section was obtained near the vortex center at a station 23 jet diameters downstream of the jet exit along the jet path. This value leads to an estimate of about ± 12% as the maximum error in $(p_s - p_{s_\infty})$ since no turbulence intensity corrections were made in the static pressure data.

Vortex Meter

The vortex meter measurements were made for one of the pair of vortices. The location of the vortex in the jet (i.e. the vortex line) was first obtained by making measurements in the Y_v-Z_v plane. In the first attempt, the information of reference 29 was used to define the vortex axis system (X_v, Y_v, Z_v). The center of the vortex was determined as the point with the maximum vorticity value for a cross section plane at any X_v station. Thus, once the vortex curve, defined as the projection of the vortex line (locus of the vortex centers) on the Y = 0 plane, was established, planes were taken normal to this new curve at various X/a stations and measurements were made again to obtain the distribution of vorticity in the X_v direction (which is normal to the planes). Measurements were made for the circular jet with the effective velocity ratio, λ, equal to eight. Three planes were taken corresponding to X/a locations of 11, 15, and 22. In each plane the vortex meter

measurements were made at about 300 points with 0.75 inch steps in the Y_v direction and 0.5 inch steps in the Z_v direction. Vorticity values were obtained for the half-plane $Y_v \geq 0$ and hence the direction of rotation of the spinner remained constant (clockwise). The vortex meter was positioned at a designated point by remotely shifting it in the X and Z direction by amounts proportional to the orientation of the plane, θ_v.

As mentioned in the previous chapter, rotation of the spinner was monitored on a counter. The maximum integration period of this counter was 10 seconds. It was found, by trial and error, that it was quite sufficient in the present investigation to record three such integrated values at any point and to use an average of the three as the value of the output pulses per second, N, of the spinner at that point.

The vortex meter output was also constantly monitored on an oscilloscope. In the region very near the plane of symmetry, the vortex meter was observed to simply oscillate about a zero, and in such cases the data were neglected.

The data as recorded in values of N were reduced to vorticity values by following the method suggested by the meter manufacturer. The equation for conversion is

$$\omega_{X_v} = 2\pi N/\eta \qquad (1)$$

where ω_{X_v} is the component of vorticity in the X_v direction and η is the frictional efficiency of the vortex meter defined as

$$\eta = \frac{1}{1 + K/V_{X_v}} \tag{2}$$

The value of the constant K was furnished by the manufacturer for the vortex meter used and is 27.6 for V_{X_v} in feet per second.

It is evident from the equation for η that it is necessary to know the value of the axial velocity, V_{X_v}, at any point in order to know the precise value of vorticity at that point. However, the dependence of ω_{X_v} on V_{X_v} is weak, i.e., a 10 percent error in the V_{X_v} value ($\sim$ 100 fps) implies only about a two percent error in the ω_{X_v} value. In the present investigation, since V_{X_v} values were not obtained at every point, an average value of V_{X_v} determined from restricted measurements of the distribution of V_{X_v} within the vortex was used. More detail is given in the next chapter regarding this approximation and its effect on the calculation of the vortex strength.

To verify the method of data reduction using Equation (1) and to evaluate the performance of the vortex meter, detailed measurements were made of a wing trailing vortex using the vortex meter, and the data were compared with measurements using the 5-hole pressure probe. The

results and discussion of this test are provided in Appendix B.

The calibrating device supplied with the vortex meter was used extensively to keep a check on the performance of the vortex meter. According to the manufacturer, the specified value of K is valid if the vortex meter rotates with a value of N approximately equal to 260 CPS with the calibrating device on and in a free-stream of 110 fps. The vortex meter bearings need lubrication periodically; in this experiment, approximately two hours of running was allowed between successive lubrications. For any traverse, at the completion of the measurements the repeatability was checked at some reference point in the traverse and was found to be ± 1 CPS which was considered acceptable. As discussed in Appendix A, it became very time-consuming and difficult to achieve an exact lubrication of the bearings such that when the calibrating device was installed the meter gave precisely 260 CPS. Hence, some data were taken with the frictional efficiency slightly lower. (The variation in η was about 0.73 versus 0.6.) The vorticity values calculated from the vortex meter data taken for a traverse with both the η values agreed well within the limits obtained from the maximum fluctuations in the average values of N.

Figure 19 represents a typical distribution of N

through the contrarotating vortices.

Since the vortex meter was operated during the experiments at an angle with respect to the horizontal, it was thought that there might be an effect on the shaft friction because of a variable load on the shaft thrust bearing. This concern was shown to be unwarranted by testing the meter with the calibrating device installed and the meter aligned in a flow which was generated by a portable blower which could be inclined at different angles to the horizontal (0^{o} to 45^{o}). It was concluded that the aerodynamic thrust on the spinner was larger than the gravity effect on the shaft since the friction was found to be unchanged over the range of angles covered.

CHAPTER IV

RESULTS AND DISCUSSION

The results to be discussed here are in terms of experimental measurements made in different parts of the flow field associated with a circular jet in crossflow. The flow problem is first divided into two regions: the jet, which includes its associated contrarotating vortices, and the wake. The quantitative and qualitative behavior of the jet is determined from temperature measurements which provide information on the shape and the size of the jet starting from the jet exit. The pair of contrarotating vortices in the jet is defined by giving quantitative measurements of the location of the vortices and of distributions of the vorticity, the core radius, and the vortex strength. These quantities, determined by using a vortex meter and a 5-hole pressure probe, are then compared with the values obtained by other techniques which have been reported in the literature.

Next, the wake region is defined, and data are presented which give its shape and extent. Losses in total pressure and velocity components in the wake are presented and discussed.

Additional measurements, including static pressures, then are presented for the regions where the jet and the

wake interact.

The velocity, pressure, temperature, and vorticity values measured using various probes in the present investigation represent time averages. Thus, no turbulence quantities were obtained. In addition, it should be recognized that the measurements were insensitive if the measurement devices were exposed to the jet fluid and the crossflow fluid in some intermittent fashion.

Finally, an overall physical picture of the whole flow field is offered, in which some ideas proposed by other investigators are explored concerning the behavior of the flow field very near the jet exit and in the very far field downstream region.

The qualitative behavior of the streamlined jet also has been obtained from temperature measurements and is included in Appendix C. The results presented and discussed in this chapter are solely for the circular jet.

Behavior of the Jet in Crossflow

Variations in the shape and size of the jet in crossflow are presented here by means of plots of contours of constant C_T,

$$C_T = (T - T_\infty)/(T_j - T_\infty)$$

where T is the local total temperature in the jet. The plots are given for cross sections in the X-Y, Y-Z and X-Z planes. These plots describe the behavior of the jet in terms of variations in its shape and size. Complete temperature surveys were made only for the $\lambda = 8$ case. However, the penetration of the jet is also presented for values of $\lambda = 4$ and 12.

Temperature Centerlines

Figure 20 compares temperature centerlines (defined as the loci of points of maximum temperature for any X-station in the plane of symmetry) with the jet centerlines based on maximum total pressure due to Mosher[8] for values of $\lambda = 4$, 8, and 12. Recall that the experimental set-up used in the present investigation is the same as that used by Mosher[8] and also that the jet total pressure centerline obtained here for $\lambda = 8$ agreed well with that of Mosher. Thus, the data of Figure 20 indicates that, for the circular jet, the temperature centerlines do not coincide with the corresponding jet centerlines. Although the locations of the corresponding contrarotating vortices will be presented later in this chapter, it is necessary to indicate here that the vortex centerlines are significantly below the temperature centerlines. Kamotani and Greber[23] have made similar observations and a comparison with their measurements is shown in Figure 20. The jet velocity centerline of reference 23 is identical with

that measured here. The temperature centerlines obtained in the present investigation were for an average value of $(T_j - T_\infty)$ of 80°F and therefore the data of Kamotani and Greber[23] with $(T_j - T_\infty)$ of 75°F is used for comparison.

It is of interest to examine the trend of the distributions of total and static pressure and total temperature in the plane of symmetry. Figure 21 shows a typical distribution of these nondimensionalized quantities.

The intention of the following analysis is to obtain the conditions prevailing when P_o or T maximize at the jet or temperature centerline location.

Consider the energy equation for a perfect gas applied at some point in the plane of symmetry

$$C_p T = C_p T_s + \frac{V^2}{2} \quad .$$

Eliminating T_s from the energy equation using the equation of state, $p_s = \rho R T_s$, and substituting $\frac{1}{2}\rho V^2 = P_o - p_s$,

$$\rho T = \frac{p_s}{\gamma' R} + \frac{P_o}{C_p} \quad .$$

Differentiating this equation with respect to $z = Z/a$,

$$\rho \frac{dT}{dz} + T \frac{d\rho}{dz} = \frac{1}{\gamma' R} \frac{dp_s}{dz} + \frac{1}{C_p} \frac{dP_o}{dz} \quad . \qquad (3)$$

Assuming isentropic conditions at a point, $p_s/\rho^{\gamma'}$ = constant, differentiating with respect to z, and eliminating $\frac{d\rho}{dz}$ from Equation (3),

$$\rho\frac{dT}{dz} - \frac{1}{C_p}\frac{dP_o}{dz} = -\left[\frac{1}{\gamma' R}\left(\frac{\gamma' - 1}{2} M^2\right)\right]\frac{dp_s}{dz} \quad . \qquad (4)$$

Now, consider two situations. The first occurs when P_o maximizes at the jet centerline. Setting $\frac{dP_o}{dz} = 0$ in Equation (4), then at the jet centerline,

$$\frac{dT}{dz} = -\left(\frac{\gamma' - 1}{2\gamma' R\rho} M^2\right)\frac{dp_s}{dz} \quad . \qquad (5)$$

In Equation (5) the quantities within the parentheses are always positive, implying that at the point where P_o maximizes the gradient in the static pressure, P_s, is positive and the corresponding gradient in T is negative. Such a behaviour is observed in Figure 21.

Similarly, taking the second case as the point where T maximizes, then at the temperature centerline location

$$\frac{dP_o}{dz} = \frac{M^2}{2}\frac{dp_s}{dz} \quad . \qquad (6)$$

Again from Figure 21, at the point where the temperature maximizes, because of the positive gradient in the static pressure distribution, the total pressure also has an

increasing trend as indicated by Equation (6).

The above analysis suggests that the reason that the jet temperature centerlines do not match is because of gradients in the static pressure distribution in the jet. Data will be given later in this chapter (Fig. 46) which show that the vortex centers in the jet have the lowest value of the static pressure and therefore are a possible element causing the gradients.

Extent and Shape of Jet

The extent of the jet is defined as being the region within which the temperature is greater than one percent of the difference between the jet exit temperature and the freestream temperature. The contours of constant temperature define the shape of the jet.

Figure 22 shows the behavior of the jet in crossflow in the plane of symmetry (plane X-Z, Y = 0) for $\lambda = 8$. Near the jet exit there are two salient features. The first is the existence of a core of constant temperature having a length of about 2.3 jet diameters. As discussed in Chapter III, the velocity core for the jet in the $V_\infty = 0$ condition had a length of about 3.75 jet diameters. With the same $V_\infty = 0$ condition, if measured, the corresponding temperature core would have been found to be smaller than the velocity core, but the difference would have been very small. Therefore, the large

reduction in the length of the temperature core is attributed to the increased shearing action on the edges of the jet near the exit because of the crossflow velocity. The reduction by 40% in the length of the core for $\lambda = 8$ is reasonable in comparison with similar data reported in reference 26. Moreover, as is expected for the case of λ greater than four[34], no bending of the temperature core is found in the present investigation for $\lambda = 8$.

The second salient feature observed near the jet exit is the "hump" shape of the jet on the downstream side. Such a shape indicates some localized mixing phenomena occuring in the region.

As the jet bends downstream, the rapid decay of temperature in the jet is seen in Figure 22. The extent of the jet increases considerably within a short distance from the jet exit, increasing to a size of 6 to 7 jet exit diameters within 10 diameters along the jet path. The extent of the jet in the plane of symmetry obtained from the total pressure profiles of reference 21 is about one-half that of the present investigation.

The wake region behind the jet does not seem to contain any appreciable amount of jet fluid because no temperatures in excess of T_∞ were measured there.

Figure 23, (a) through (e), shows the successive behavior of the jet in the Y-Z plane as Z increases. It can be seen that the deformation of the jet for $\lambda = 8$

becomes significant after the jet fluid travels about one jet diameter. A distinct "kidney" shape is forming by two jet diameters (station located about at the end of the core) and the jet has deformed fully to a kidney shape by three jet diameters. Figure 23(e) shows the relative location of the rolled-up vortex as obtained in reference 30. The deformation of the jet is attributed to the rolling up of the vortices. Figure 23 shows that there is no significant roll-up of jet fluid upto one jet diameter, but the process has already begun at two jet diameters. Reference 23 obtained the jet cross section shapes for stations three and seven jet diameters downstream of the jet exit. No roll-up can be seen for the station at three diameters in the data of reference 23.

Two cross sections of the jet in Y-Z planes are shown in Figure 24. Again, the kidney shape and the growth of the jet are noticed, with progressively higher temperatures in the vortex region rather than in the center of the main body of the jet. The gradients in the temperature distributions are more severe near and between the pair of contrarotating vortices.

The results of this section will be used later in the chapter as a basic for defining the extent of the jet region. Additional data for the circular jet are given in Appendix C for comparison with the behavior of the streamlined jet.

The Contrarotating Vortices of the Jet

It is observed that the dominant feature of the jet in crossflow is a pair of contrarotating vortices. The region containing these rolled-up vortices is a large portion of the jet. Direct measurements were made with a vortex meter and a 5-hole pressure probe in the half-plane ($Y/a \geq 0$) to study the physical characteristics of one of these vortices. Results such as the location of the vortex, the vorticity distribution, the diffusion rate, and the circulation are provided in this section. The axial and circumferential velocity distributions in the vortex region and the procedures used in calculating the vortex strength are also discussed in detail. A comparison is made of the results obtained in the present study of the vortices with other available experimental measurements and vortex models.

Vortex Centerline

The location of the contrarotating vortices is defined by projecting, on X-Z and X-Y planes, the locus of centers of one of the vortices (vortex centerline). The projection on the X-Z plane ($Y = 0$) is called "the vortex curve" and the projection on the X-Y plane ($Z = 0$) is "the vortex spacing".

Vortex Curve. The vortex curve was obtained by two methods in the present investigation. In the first method, which is more direct than the other, the vortex centers

obtained from the vorticity measurements made with the vortex meter are projected on the plane of symmetry (Y = 0) to obtain the vortex curve. The second method makes use of the distributions of velocities in the plane of symmetry to infer the vortex curve. Tipping[27] recognized that the upwash velocity, V_Z, and the upwash angle, α, reach a maxima between the centers of the contrarotating vortices for any traverse in the Z direction on the plane of symmetry. Hence, for the second method, the vortex curve is defined as the locus of points on the plane of symmetry where the α-distribution has a maximum for any traverse in the Z direction. (It was easier to get α from probe null in the present tests, and therefore this criterion is used here.)

Figure 25 shows the distributions of α obtained using the 5-hole pressure probe. The distributions are for several traverses in the Z direction on the plane of symmetry for the circular jet with $\lambda = 8$. The distributions, for any X/a, reveal that the upwash angles reach a maxima at a certain Z/a value. In the second method, this Z/a value is taken to be the location of the vortex curve for the particular X/a. It is clear (from the curves for X/a = 11 and X/a = 22) that the maxima are attained at a Z/a value lower than that for the jet centerline location (points of maximum total pressure). The jet centerline location can be recognized in the figure as being where $\frac{d\alpha}{dZ}$ remains

essentially zero because the flow field of the main body of the jet is not significantly affected by the velocity field associated with the vortex. This behavior of the upwash angle distribution near the jet centerline is apparent for X/a = 11 in the present data and in the data of Jordinson[21] plotted on the same figure. However, it can be seen that the upwash angle distribution for X/a = 22 does not have a very flat character near the jet centerline location. This indicates that, at this station, the magnitude of the velocities associated with the vortex motion near the main body of the jet is significant in comparison with the velocity in the main body of the jet which has been decreasing because of mixing. A quantitative check is made next to see how well the vortex curve obtained by the second method compares with the curve obtained using the vortex meter.

Figure 26 shows the vortex curve obtained by the two methods for the case of $\lambda = 8$. The jet centerline is also shown to illustrate the relative location of the contrarotating vortices and the main body of the jet. The figure reveals a maximum discrepancy of less than 0.5a between the predictions by the two current methods. The vortex curve obtained in the present investigation using the vortex meter is considered to be the more correct one.

The data both for the vortex curve and for the jet

centerline are in good agreement (within 0.5a) with reference 29 except that a lower location of the vortices is obtained in the present investigation with the vortex meter at an X/a location of four. Although the vortex curve predicted by the vortex models of Fearn and Weston[30] lies slightly above both the data of reference 29 and the vortex meter data of the present investigation, it may be that this is because the jet centerline obtained in reference 30 is also above that of reference 29 and the present investigation. Hence, the relative location of the contrarotating vortices with respect to the jet centerline predicted in reference 30 is in satisfactory agreement with both the data of the present investigation and that of reference 29.

Thus, it is concluded that the vortex curve obtained from the velocity measurements is in good agreement with the vortex meter data and that the vortex models of reference 30 predict the vortex curve adequately. Also, the upwash velocity and angle do maximize between the vortex centers.

Figure 26 further reveals that, for $\lambda = 8$, the location of the pair of contrarotating vortices is significantly different from that of the main body of the jet having essentially axially moving fluid. The explanation for this difference is apparent from the figure if the slope of the vortex curve is compared with that of the jet centerline at various values of X/a. The initial

deflection of the vortex curve very near the jet exit is much greater than that of the jet centerline. In explaining the origin of the contrarotating vortices, Crawford[25] commented that as the jet enters the crossflow it produces a region of very turbulent shear flow and this vortex-generating shear flow occurs along the sides of the jet. According to Jordinson[21], the vertical momentum (in the Z direction) of this mixing region will be less than that of the core and consequently the mixing region will be deflected more than the core. After this major initial deflection, the rate of change of the subsequent deflection of the vortex curve is about the same as that of the main body of the jet.

Vortex curves for values of λ other than eight are presented in references 29 and 30 for the circular jet. The effect of λ on the general behavior of the vortex curve and on the relative locations of the vortex curves and the jet centerlines seems to be insignificant. Both of these investigations report a curve-fitting to the vortex curve and the jet centerline in a power-law form

$$Z/a = a_1 \lambda^{a_2} (X/a)^{a_3} \tag{7}$$

where a_1, a_2, and a_3 are constants to be evaluated by the method of least squares fit. In the present investigation,

the value of λ is constant and hence cannot be taken as a parameter in the least squares fit. However, the power of λ, a_2, is found to be close to unity in references 29 and 30, and therefore the other constants are derived in the present investigation with $a_2 = 1$. With this assumption, the constants are obtained for the jet centerline and the vortex curve (vortex meter method only) and are compared with those obtained by references 29 and 30 in Table 2. The table also lists the coverage of λ for which the vortex curves were obtained. Figure 26 shows the vortex curve calculated using Equation (7) with the present constants.

The significance of representing the vortex curve and the jet centerline by empirical relationships similar to Equation (7) lies in the fact that, in the literature, the jet centerline for a circular jet is extensively reported for many cases. Therefore, the vortex curve in such cases can be estimated by subtracting the amount $\Delta(Z/a)$ from the Z/a value of the jet centerline. $\Delta(Z/a)$, as a function of λ and (X/a), can be evaluated by using the constants of any one of the three experimental sets. From the values of the constants in the present investigation,

$$\Delta(Z/a) = \lambda\left[\ (X/a)^{0.4}\ \left\{1 - \frac{(X/a)^{0.1}}{2}\right\}\ \right] \quad . \qquad (8)$$

This relationship can be used to deduce the approximate difference between the vortex curve and the jet centerline for any λ.

Vortex Spacing. Once the contrarotating vortices develop and get rolled up on both sides of the jet, the spacing between the centers of the vortices varies along the length of the jet. To complete the definition of the location of the vortices in the flow field, knowledge about the spacing is needed in addition to the shape of the vortex curve. Figure 27 shows the variation in the half-spacing (projection of one of the vortex centerlines on the X-Y plane, Z = 0) obtained in the present investigation using the vortex meter. In the figure, a comparison is made of the vortex spacing obtained by other investigators with that of the present results. The maximum discrepancy between the present data and the data (using velocity measurements) reported in reference 29 is 0.25a, with the half-spacing being less in the present tests. The figure also shows that the diffuse vortex model (described in Chapter I) of Fearn and Weston[30] predicts the vortex spacing accurately.

The vortex spacing for values of λ other than eight are also reported in references 29 and 30. The data of

reference 29 show that increasing the value of λ from four to eight increases the spacing between the vortices by about one jet diameter. Moreover, the analysis of reference 31 shows that the vortex spacing is a weak function of λ and, in particular, the effect of λ on the vortex spacing is small for large values of X/a.

Velocity Distributions

In this section the axial and circumferential velocity distributions in the vortex region, obtained with the 5-hole pressure probe, are discussed. It is necessary to know the variations in the axial (X_v) velocities through the vortex to be able to reduce the vortex meter data, while the circumferential velocity distributions provide important information regarding the diffusion of the vortices and variations in the vortex core radius as the vortices decay.

Axial (X_v) Velocity Distributions. Figure 28 shows the distribution of velocity in the X_v direction (parallel to the vortex curve) for two stations, X/a = 11 and X/a = 22. The traverses in the Z_v direction, in the plane of the vortex, were made approximately through the vortex centers. It can be seen that the axial (X_v) velocity values do not remain constant through the vortex. For both X/a stations, the axial (X_v) velocity component has a peak at the center of the vortex and the values of V_{X_v} are found to be higher than the freestream velocity, V_∞. Away from the center of the vortex, V_{X_v} diminishes; however, in the region where the vortices

interact with the main body of the jet (i.e. Z/a > +3 in Figure 28), V_{X_V} increases again because of the presence of the main body of the jet.

Recall from the previous chapter that to convert the vortex meter data (as recorded in values of N) to vorticity values it is necessary to know the velocity component along the vortex filaments intercepting the vortex meter (Equations (1) and (2)). It was also pointed out that the dependence of the calculated vorticity values on axial (X_V) velocity is weak. Moreover, the primary aim behind the measurement of vorticity distributions is to estimate the total strength of the vortex. Hence, if some average value of the axial (X_V) velocity distribution were taken as a constant value for any particular plane of the vortex, it is expected that the error in calculating the vortex total strength would be less than the error in calculating local vorticity because of cancellation rather than accumulation of errors in the process of integration. Obtaining axial velocity values at every point where measurements were made with the vortex meter would have been a very time-consuming process; only single traverses were made for each vortex plane in order to have some basis for taking an average axial velocity in that plane. Thus the axial velocity is assumed to have a constant value which is the average of the axial (X_V) velocity at the center of the vortex and the freestream velocity. It can be interpreted

from the results of Fearn and Weston[30] that this constant value is a reasonable average value for the whole vortex excepting regions near the main body of the jet where the value of vorticity was found to be small in any event. Further discussion of the errors associated with this assumption follows in the sections describing the calculation of the vorticity and the vortex strength.

Figure 29 illustrates the behavior of the axial velocities at the jet and vortex centerlines as a function of distance from the nozzle exit. To clarify the variables, V_{X_j} is the axial velocity at the jet center and is parallel to the jet centerline; V_{X_v} is the axial velocity at the vortex center and is parallel to the vortex curve. It can be seen that the axial velocity in the main body of the jet decays monotonically, and it is expected that the decay of velocity V_{X_j} would continue (although the rate of decay may reduce) until the main body of the jet is moving almost parallel to the freestream and with the freestream velocity, V_∞. The figure also shows that the axial velocity, V_{X_V}, at the vortex centers has a magnitude which is at least as large as the corresponding jet centerline axial velocity for the Y-Z cross sections between station X/a = 11 and station X/a = 22. The jet is usually imagined as having a high velocity plume, and it is conventional to locate the jet in the crossflow by finding points with maximum velocity in the

plane of symmetry (Y = 0). Figure 29 shows that the velocity in the vortex core can be higher than at the jet velocity centerline. Finally, the rate of change in V_{X_v} is not the same as that of V_{X_j}. Unlike the monotonic decay of velocities in the jet, the core of the vortex gains axial momentum in its initial phase of development[23], and thereafter V_{X_v} decays because of viscous diffusion.

Circumferential Velocity Distributions. Figure 30 shows the circumferential (rotational) velocity distribution for two traverses through the vortex. Strictly speaking, the velocity component, V_{Y_v}, which is shown is not exactly equal to the circumferential velocity because the traverses were not made precisely through the vortex centers. However, since the traverses were within 0.5a of the vortex centers, the distributions of V_{Y_v} in the figure correctly represent the variations in the circumferential velocity distribution for traverses through the vortex centers.

It can be seen in the figure that in the lower portion of the vortex (negative Z_v/a) at station X/a = 11 the circumferential velocity distribution shows a behavior similar to that of the Rankine combined vortex consisting of an interior core rotating like a solid body and a surrounding free ("potential") vortex for which the circumferential velocity diminishes with radius. However, such a well-defined behavior of the vortex is not found in the upper

regions (positive Z_v/a) for station $X/a = 11$. A likely cause of this behavior is that the velocity field of the vortex interacts with that of the main body of the jet (the jet center is located about 6a above the vortex center), and hence the characteristics of the vortex flow field are altered in this region of interaction. Such an interaction would diminish by station $X/a = 22$ since the velocity associated with the main body of the jet decays along the length of the jet.

In a later section in which the vortex core radius distribution is discussed, values of the core radius are obtained from the circumferential velocity distribution for the lower portion of the vortex (negative Z_v/a) where the core is well defined.

Vorticity Distributions

In this section, the vortex meter data (as recorded in values of the output pulses per second, N) are discussed first, and then results are presented giving distributions of vorticity calculated using these vortex meter data.

As mentioned in Chapter III, planes normal to the vortex curve were taken at three different locations and the output of the vortex meter, N, was recorded at several locations in the planes. Figure 31 shows typical distributions of N obtained in these tests for traverses made in the Z_v direction. It can be seen that as X_v/a

increases (i.e., going downstream along the length of the vortex), the vortex is more diffused. Moreover, for any X_v/a station, the distribution of N does not show any similarity between the lower (negative Z_v/a) and the upper (positive Z_v/a) portions of the vortex. The flat regions of the distributions are obtained where the vortex mixes with the main body of the jet. Recall that the axial (X_v) velocity in this region of mixing also increases locally (Figure 28). Equations (1) and (2) show that, for a given vorticity value, the vortex meter rotates at a higher rate (i.e. N is greater) for higher axial velocity values. Thus, one of the possible reasons that the values of N do not drop off in the upper region at the same rate as in the lower region is the added contribution of the higher axial velocities to the vortex meter rate of rotation. Using the correct local value of V_{X_v} along a traverse will change the vorticity distribution in comparison to the distribution of N shown in Figure 31.

Because it was not possible to measure values of V_{X_v} at every point at which the vortex meter measurements were made, an average value of V_{X_v} was used to calculate vorticity distributions as was discussed in the previous section. Equations (1) and (2) were used to convert the vortex meter data (as recorded in values of N) to vorticity values. Figure 32 illustrates contours of constant vorticity

radius of the vortex core is not well defined in the region of mixing between the velocity fields of the main body of the jet and the vortex.

The Core Radius Distribution

In this section results are presented which give the variation in the radius of the vortex core along the length of the vortex. The core radius distribution first is obtained from the velocity measurements and then is calculated from the vorticity distributions discussed in the previous section.

The core radius, r_c, of the vortex is defined as the radial distance from the center of the vortex to the point where the circumferential velocity is a maximum. It was pointed out earlier in connection with the discussion concerning the circumferential velocity distributions that the core radius is well defined for the lower portion of the vortex (negative Z_v/a), and therefore the core radius distribution is calculated using that portion of the data. From the velocity measurements, the distribution of r_c is calculated along the length of the vortex curve and the result is presented in Figure 33. It can be seen that the vortex is large, with the diameter of the core varying from about 3.3 to 4.5 jet exit diameters over the region in which the velocity measurements were made. The maximum circumferential velocity at the core edge was found to vary from

about 50 to 70 percent of V_∞ (Figure 30), so that the contrarotating vortices are strong as well as large. They truly may be said to be the dominant feature of the flow field associated with the jet in crossflow.

The core radius distribution was also calculated from the vorticity distributions discussed in the previous section. However, certain assumptions are required to be able to relate the measured vorticity distribution to the circumferential velocity distribution from which r_c can be obtained using the definition given in the previous paragraph. It is assumed that each vortex in the pair is a two-dimensional, symmetric vortex, and that the vorticity distributions of each vortex are independent of the effect of the other vortex. Then, for such a vortex, the vorticity distribution is a Gaussian

$$\omega_{X_v} = \omega_{X_{vo}} e^{-\beta^2 r^2} \tag{9}$$

where r is the radial distance from the center of each vortex and β is the diffusion constant for the vortex.

The circumferential velocity distribution for the vortex with the vorticity distribution of Equation (9), and the maximum point of that circumferential velocity distribution, can be obtained analytically. Following this procedure, one can relate r_c and β as

$$r_c = \frac{1.121}{\beta} \quad .$$

Then, r_c can be obtained by fitting the Gaussian distribution of Equation (9) with the measured vorticity distribution for the lower portion of the vortex. The comparison of these r_c values with the values obtained from the measured circumferential velocity distributions is shown in Figure 33. As discussed in the previous section, the vorticity values which are calculated from the vortex meter data contain errors associated with a lack of detailed knowledge of the V_{X_V} distribution. The error bands shown in Figure 33 represent the uncertainty in the r_c values because of the uncertainty in the vorticity for the reason explained above. The agreement between the r_c values calculated by both of the methods is deemed satisfactory considering the assumptions required for the second method (vortex meter data).

Figure 33 also shows a comparison between the r_c values from the present tests with those predicted by the diffuse model of Fearn and Weston[30]. The diffuse model makes use of velocity measurements and contains the assumption of the two-dimensionality of each vortex. From the good agreement with the present values, calculated using the vortex meter measurements with the same assumption of the two-dimensionality of the vortex, it can be concluded that the diffuse model of reference 30 predicts the core radius

accurately.

Sellers[31], in analyzing the data of reference 30, noted that for a jet in crossflow the core radius of the vortex predicted by the diffuse vortex model varies parabolically with the length of the vortex and that this observation can be related to an eddy viscosity for turbulent flow. However, no analysis is presented in reference 31 to validate the above argument.

In the present investigation, the aim of the following analysis is to find such a relation between the variation in r_c and an eddy viscosity.

The first step is to obtain an empirical expression relating the present r_c values (from velocity measurements) with X_v. The required expressions is

$$\frac{r_c}{d} = 0.541 \left(\frac{X_v}{d}\right)^{1/2} . \qquad (10)$$

There is an assumption inherent in obtaining Equation (10), namely that right at the jet exit ($X_v/d = 0$) the vortex is a filament type with no core and all of the vorticity concentrated at the center of the vortex.

Now, it is known (Reference 40) that for a single, rectilinear, viscous vortex with constant axial velocity the vortex core expands with time as $t^{\frac{1}{2}}$, a characteristic of viscous diffusion. Then, if the vortex is turbulent,

r_c varies with time as $r_c \sim (\nu + \nu_T)^{\frac{1}{2}} t^{\frac{1}{2}}$, where ν is the kinematic viscosity and ν_T is an eddy viscosity. For most practical purposes, for example, in trailing vortices behind aircraft, ν can be neglected in the presence of ν_T. Instead of the time scale, the core radius can be expressed as a function of a length scale and, using the expression for r_c presented in reference 40 for a single, rectilinear vortex,

$$\frac{r_c}{C} = 2 \left(\frac{\nu + \nu_T}{C U_o} \right)^{1/2} \left(\frac{s}{C} \right)^{1/2} \tag{11}$$

where U_o is the constant axial velocity of the vortex, s is the distance downstream from the origin of the vortex, and C is the fixed length scale parameter of the flow (for instance, the chord length at the root of a finite wing). Now, for the purpose of analogy, and using appropriate variables, Equation (11) can be converted for application to the growth of one of the contrarotating vortices in the jet in crossflow as

$$\frac{r_c}{d} = 2 \left(\frac{\nu + \nu_T}{d \, V_{X_v}^*} \right)^{1/2} \left(\frac{X_v}{d} \right)^{1/2} \tag{12}$$

where $V_{X_v}^*$ is some representative axial velocity of the vortex. $V_{X_v}^*$ varies along X_v, and therefore Equation (12) is assumed to be applicable for the growth of the vortex

in the jet at a local station. However, the important aspect of this analysis is the similarity between the two Equations (10) and (12). The comparison gives

$$0.541 = 2 \left(\frac{\nu + \nu_T}{d\, V_{X_V}} \right)^{1/2} . \qquad (13)$$

Now, for instance, at $X_V/d = 10$ if the value of V_{X_V} is taken at the center of the vortex and substituted into Equation (13), the result is that $(\nu + \nu_T) \simeq 1$ ft^2/sec. Since the kinematic viscosity of air is $\nu \simeq 2\text{x}10^{-4}$ ft^2/sec, then for the vortex at $X_V/d = 10$, $\nu_T/\nu \simeq 5000$. This value of the ratio ν_T/ν is not unexpected because the turbulence intensity in the vortex core is very high. Kamotani and Greber[23] reported that the turbulence intensity is as high as 20% of the maximum mean velocity for a cross section at $X_V/d = 20$ and that it is concentrated in the core of the vortex in the jet.

The above discussion reveals that the contrarotating vortices in the jet in crossflow are governed by turbulent processes and that viscous diffusion of the vortices is mainly controlled by the eddy viscosity. The parabolic growth of the vortex along its length indicates that the rate of growth of each of the contrarotating vortices in the jet in crossflow is nearly the same as the growth of a single, rectilinear, viscous vortex.

The Strength of the Contrarotating Vortices

In this section, the determination of the vortex strength is discussed first and then a comparison is made with the findings of other investigators.

Vortex Strength Calculation. The strength of each vortex in the pair at a particular location along the length of the vortex curve is defined as the flux of the vorticity component, ω_{X_v}, through the area bounded by a half-plane, either $Y_v \geq 0$ or $Y_v \leq 0$.

Mathematically, one can write,

$$\Gamma = \iint_S \omega_{X_v} \, dS \tag{14}$$

where S is the area bounded by the half-plane. Non-dimensionalizing, $\gamma = \Gamma/2dV_\infty$.

In the present experiments, the cross-section planes were taken normal to the vortex curve (i.e., normal to the X_v direction) and the value of the vorticity component, ω_{X_v}, was measured at various data points on the cross section. By means of numerical integration over the area S (which is finite as is discussed next) in Equation (14), using Simpson's rule, vortex strength values were calculated. The lower curve in Figure 34 shows the distribution of the vortex strength obtained by this method.

There are two major sources of error in calculating

the vortex strength by the above procedure. The first is the uncertainty with which local vorticity values are measured. The second major cause of error in the vortex strength calculation is the possibility that the integration may not have been carried out over a large enough area. In the experiments, time did not allow the measurement of vorticity over the entire Y_v-Z_v plane and this may have resulted in the omission of some flux of vorticity. Even though vorticity values are not large in the regions where measurements were not made, the cumulative flux of vorticity over a large area may not be insignificant. Therefore it is necessary to discuss these two sources of error.

The uncertainty with which local vorticity values were measured is due to uncertainties in the frictional efficiency of the vortex meter, fluctuations in the vortex meter readings, and errors introduced because of the lack of knowledge of the complete axial (X_v) velocity distribution. The uncertainties in the local vorticity values due to the frictional efficiency and the fluctuations in the vortex meter readings lead to about a ± 4% uncertainity in the values of Γ calculated using Equation (14). It is recalled that an average axial (X_v) velocity value was used (for each cross section) in calculating the vorticity distribution. It is estimated that by considering V_{X_v} as a

constant for a cross section the value of the flux of vorticity is overestimated by about 1.5 to 2 percent for the lower portion of the vortex which does not interact with the main body of the jet. However, when the entire vortex (upper and lower portion) is considered, the error in the vortex strength is about 4 percent (overestimation) for station X/a = 11 where the axial (X_v) velocity values change significantly (Figure 28). The error in the vortex strength is not more than 1.5 percent (overestimation) at station X/a = 22.

The second major source of error in the vortex strength calculation is unavoidable in a real flow situation. That is to say, since in a viscous medium vorticity diffuses with time, theoretically one has to cover an infinite space to contain all of the vorticity passing through a plane to be able to obtain the total flux. In practice, one attempts to cover as large an area as possible and relies on predictions made by extrapolation in order to obtain an estimation of the vorticity which is not measured. In the present investigation, the vorticity distribution was assumed to vary as a Gaussian and it was found that the flux of vorticity outside of the areas where measurements were made was about five percent of the total flux for the station X/a = 11. Thus, the vortex strength value shown in Figure 34 for the most upstream station is about 95% of the total

vortex strength. However, the vortex becomes more diffused as it travels along its length and hence the error increases for stations further downstream. For the most downstream station, only about 80% of the total vorticity flux was contained within the region in which measurements were made. The region within which the vorticity flux was measured, for all three X/a stations, had a coverage of 7x15 jet radii in the Y_v-Z_v plane. Figure 34 shows extrapolation bands which represent the estimated magnitude of the flux of vorticity not contained in the above regions of measurement. Consideration of this second source of error in the vortex strength values led to attempts at a better estimation of the strength then the one obtained by using Equation (14).

In order to get a better measure of the strength of the vortex it is necessary to have a method which allows for the integration of the vorticity flux over the entire Y_v-Z_v cross section. Consideration of the physical picture of the interacting pair of vortices is necessary to accomplish this. In the flow, both contrarotating vortices of equal strength are spaced apart by some finite distance and both are diffusing, with the vorticity associated with each being of the opposite sense. Hence, when the vortices interact with each other they diminish one another's strength.

Now, if it is assumed that each vortex in the pair is two-dimensional in the plane normal to the vortex curve,

then the vorticity distribution for each vortex is given by a Gaussian, as shown earlier,

$$\omega_{X_v} = \omega_{X_{vo}} e^{-\beta^2 r^2}$$

where $\omega_{X_{vo}}$ is the vorticity in the center of each vortex, β is the diffusion constant, and r is the radial distance from the center of each vortex.

The strength of each vortex integrated over an infinite space, before considering the presence and the interaction of the other vortex, is given as

$$\Gamma_o = \frac{\pi}{\beta^2} \omega_{X_{vo}} \quad . \tag{15}$$

When the mutual interaction is taken into account, the flux of vorticity for each vortex in the half-plane, i.e., the effective vortex strength, is given as

$$\Gamma = \Gamma_o \, \mathrm{erf}(\beta h) \tag{16}$$

where 2h is the spacing between the vortex centers. The value of the error function, erf(βh), is always less than unity and represents losses in the vorticity flux because of the restriction of the integration to only a half-plane.

The factor also includes the reduction of vorticity in that half-plane because of vorticity of the negative sense, created by the other vortex, diffusing into the half-plane. Equation (16) is valid for the diffuse vortex model of reference 30.

Now, in the present investigation, the spacing between vortices has been obtained (Figure 27) and the diffusion constant, β, is given for the two-dimensional case as

$$\beta = \frac{1.121}{r_c} \tag{17}$$

where r_c is the radius of the vortex core. The distribution of r_c was obtained earlier as shown in Figure 33. Using the experimental value of $\omega_{X_{vo}}$ in the following expression, which is obtained by combining Equations (15) and (16),

$$\Gamma = \frac{\pi \omega_{X_{vo}}}{\beta^2} \operatorname{erf}(\beta h) \ , \tag{18}$$

the effective vortex strength of each vortex can be calculated. Figure 34 gives a comparison of the vortex strength values obtained using this method and the previous procedure using Equation (14). Figure 34 shows that the vortex strength values obtained by the latter (Equation (18)) method of calculation are higher than the values obtained

by the former (Equation (14)) method. This is expected, since the method using Equation (18) integrates the vorticity distribution over the complete half-plane and the only knowledge required to get the strength is the measured vorticity in the center of the vortex, the diffusion constant, and the spacing between the vortex centers. However, in the first method the integration of Equation (14) was limited to a finite region.

It can be seen in Figure 34 that if the strength values of Equation (14) are incremented by the estimated vorticity flux outside the finite area of measurement (obtained by Gaussian extrapolation methods), the agreement between the corrected values and the values obtained using Equation (18) is within 5%. The small difference may arise because of the assumption of the two-dimensionality of each vortex used in the latter method. However, the discrepancy is also within uncertainties (discussed next) in the strength values associated with the use of Equation (18).

Inspection of Equation (18) shows that the error in Γ is related to errors in $\omega_{X_{vo}}$, β, and h. The uncertainties in $\omega_{X_{vo}}$ because of the frictional efficiency of the vortex meter and the fluctuations in the vortex meter readings give about a $\pm$ 4% uncertainty in Γ. Since the axial velocity was measured at the vortex centers and the correct V_{X_v} values were used in calculating $\omega_{X_{vo}}$, no error is introduced because

of this factor. The diffusion constant, β, is found by using Equation (17). The error in β is due to the uncertainty in the r_c values, which varies from about $\pm$ 0.125a at X/a = 11 to about $\pm$ 0.25a at X/a = 22. This introduces from $\pm$ 4% to $\pm$ 6% uncertainty in β. Similarly, the uncertainty in the value of the vortex spacing, h, is about $\pm$ 0.25a along the length of the vortex.

The overall uncertainty in the vortex strength values as calculated by Equation (18) was estimated by taking the R.M.S. value of the errors contributed by the factors discussed above. Figure 34 shows the vortex strength distribution obtained using Equation (18) together with the error bands based upon these estimates. The figure shows that the 5% discrepancy between the two methods is well within the error bands of the method of Equation (18).

From the comparison of the two calculation methods described above, it is concluded that the vortex strength can be calculated quite accurately (within 5%) by using the procedure of Equation (18); one need not measure vorticity over the entire Y_v-Z_v plane. It is important that the radius of the vortex core be measured accurately, since Γ varies approximately as r_c^2. It is suggested that, after locating the vortex center, r_c be obtained by measuring the circumferential velocity distribution along a traverse through the vortex center together with a point measurement

of the vorticity (using a vortex meter) at the vortex center. The vorticity value obtained from the vortex meter data is more accurate if V_{X_v} at the vortex center is also known.

Next, a comparison of the vortex strength distribution obtained in the present investigation will be made with the findings of other investigators. Note that in Figure 35, where this comparison is made, the values of Γ using Equation (14) are incremented with the extrapolation corrections shown in Figure 34.

Comparison with Other Investigations. In Figure 35 the vortex strength distribution obtained in the present investigation is compared with the distributions reported by Thompson[29], Fearn and Weston[30], and Sellers[31]. However, the work of reference 31 is not independent of the work of reference 30. Rather, it is a more detailed investigation of a model proposed in reference 30. Basically, the difference between the present method of determining the vortex strength and the methods used by the other investigators (References 29, 30, and 31) lies in the fluid-dynamical quantity measured. All of the other investigations involved measurements of velocities in the flow field, and then the vortex strength distribution was inferred from the kinematic relations between velocity and vorticity. Vorticity values were measured directly in the present investigation and then the total flux of vorticity was

calculated.

Thompson[29] calculated the vortex strength from velocity measurements by two methods. For both methods, the velocity measurements were made in planes normal to the vortex curve. In the first method, circumferential velocity distributions were obtained on traverses through the vortex centers. Then, considering each vortex in the pair as an isolated, two-dimensional vortex, the vortex strength was calculated from the measured circumferential velocity distribution through the vortex centers. Thompson obtained the variation of the vortex strength along the vortex curve for three values of λ = 2.3, 4.0, and 8.1. These vortex strength values were checked at a single location on the vortex curve for each λ by using another method which is more general. In this second method, the circulation was evaluated by contour integration of the tangential component of velocity around rectangular contours of increasing size enclosing the vortex center. The circulation around the largest circuit was considered as the correct value, and this value was within five percent of that obtained using the first method for λ = 8. Single data point measurements of the vortex strength by Tipping[27] (obtained from the line integral of the tangential component of velocity) at λ = 6.7 and 10, and by Margason and Fearn[32] (obtained using a vortex meter) at λ = 4 fall well within the

pattern of the data of Thompson[29]. Thompson stated a maximum possible error in calculated vortex strength of 10%, this representing an underestimation in the vortex strength values at $\lambda = 8$ because of an inability to enclose the vortex completely within the contour used in the second method. Figure 35 shows that the vortex strength values calculated in the present investigation for $\lambda = 8$ are about 5% higher than those reported by Thompson[29]. However, if the 10% underestimation noted above were to be added to the values of Thompson[29], the agreement then is within the region covered by the error bands shown in the figure. Hence, whether or not one corrects the vortex strength values of Thompson[29], the values found in the present investigation are within 10% of those reported in reference 29, and the agreement with reference 29 is judged to be adequate.

The recent work of Fearn and Weston[30] consists of two simple, two-dimensional models for a pair of contra-rotating vortices. The basic quantities required for these models in order to predict the vortex strength are again the velocity components in planes normal to the vortex curve. In the first model, each vortex of the pair is considered as a filament with vorticity concentrated at the centers. In the second model, the vortices are considered to be viscous and diffusing. The individual vorticity distributions within each of the contrarotating vortices are

assumed to be Gaussian and are taken to be interacting with each other. For the filament model, which is simpler, one needs to measure only the upwash velocity, V_{Z_v} (velocity component in the Z_v direction), in the plane of symmetry. In the case of the diffuse model, one needs to measure V_{Z_v} at data points throughout the particular cross section for which the vortex strength value is to be determined. In both the vortex models, it is assumed that the measured upwash velocity field is due to the induced velocities of the pair of vortices plus the component of the crossflow velocity in the Z_v direction. The vortex strength, Γ, and the spacing, 2h, between the vortex centers are the unknowns for the filament model. The diffusivity of each vortex expressed in terms of the diffusion constant, β, is an added unknown for the diffuse model. For a particular model, assuming the two-dimensionality of the velocity field induced by the vortices, the unknowns are calculated for a cross section by least squares fitting the measured V_{Z_v} distribution with the component of velocities (in the Z_v direction) induced by the vortices plus the component of V_∞. The degree to which the models fit the measured velocity data is calculated in terms of the standard deviation, and the aim is to obtain the unknowns which minimize the standard deviation. Equations (15) through (18) used in the present investigation to calculate the vortex strength

represent physically the diffuse vortex model of reference 30.

Fearn and Weston[30] compared the vortex strength distributions obtained from both of the vortex models for λ = 3, 4, 6, 8, and 10. Their results show that the maximum difference, at a certain point X/a, between the vortex strength value obtained from the simpler filament model and that obtained from the diffuse model is about 12% for λ = 8. As a test, Fearn and Weston[30] took the velocity measurements of Thompson[29] and Kamotani and Greber[23], each for a single cross section at $\lambda \simeq 8$, and then applied their diffuse model to obtain corresponding vortex strength values. The agreement of the strength values obtained by Fearn and Weston[30] (diffuse model) with the strength values resulting from the application of the diffuse model to the velocity data of references 29 and 23 is within 12%, with the values of reference 30 being higher. Fearn and Weston[30] used this method as a test of the diffuse model because the vortex strength value obtained from the application of the diffuse model to the velocity data of Thompson[29] is within 5% of the value that he estimated from the contour integration of the velocity field for the same cross section of the vortex. However, Figure 35 shows that, over the length of the vortex curve covered in the present investigation, the vortex strength values predicted by both of the models of

reference 30 are higher than the measured values of the present investigation and those of reference 29. The diffuse model, which is the more exact of the two, predicts about a 25% higher value. This discrepancy is not insignificant, and it is desirable to discuss possible uncertainties in the vortex strength values reported by Fearn and Weston[30], together with an examination of the validity of certain assumptions involved in their models.

Recall that Fearn and Weston[30] calculated the unknowns Γ, h, and β by minimizing the standard deviation of the predicted upwash velocity distributions. One of the major conclusions of reference 30 is that the value of γ_o, the nondimensionalized Γ_o of Equation (15), obtained from the diffuse model may be taken as a constant along the length of the vortex for a particular λ. Furthermore, it was observed that γ_o increases linearly with λ and that the constant of proportionality, A, is about 0.72, i.e.,

$$\gamma_o = A\lambda \quad . \tag{19}$$

For $\lambda = 8$, regardless of whether the constraint is put on γ_o to be a constant in the analysis or not, reference 30 showed that the diffuse model predicts upwash velocities for any cross section with a standard deviation ranging from 3 to 5.8 percent of the maximum upwash velocity induced by the

vortex system. Using the data of reference 30, Sellers[31] later made a thorough investigation of the diffuse model of reference 30 for the $\lambda = 8$ case. Sellers[31] examined Equation (19) in detail and stated the following conclusion regarding the value of the constant, A :

> "In summary, this investigation did not find an error in the value of A = 0.72 given by Fearn and Weston, since the overall fit for $\lambda = 8$ does have a physical minimum in this region (figure 7). This study does show that any value of A > 0.6 will work almost as well."

The "figure 7" in this quotation is a figure which shows the relationship between A and the standard deviation of the predicted upwash velocity distributions. The above paragraph indicates that the standard deviation remained within the limits obtained by Fearn and Weston[30] even if the value of A were taken as low as 0.6.

Reference 31 provides data for the distribution of the vortex strength with varying A for $\lambda = 8$. In Figure 35, the vortex strength distribution of Sellers[31] is plotted for A = 0.6 and shows a reduction in the vortex strength values by about eight percent compared to those of reference 30 with A = 0.72. The conclusion by Sellers[31] seems to indicate that, based solely on the argument of minimizing the standard deviation in the diffuse model, the lower values of γ obtained is a reasonable lower limit for the γ values reported in reference 30. However, the values of γ in the

present investigation are still lower (by about 16 to 17%) than those of Sellers[31] with A = 0.6. The following observations are made concerning certain assumptions involved in the vortex models of reference 30.

As mentioned earlier in this section, Fearn and Weston[30] assumed that the component of the freestream velocity in the Z_V direction must be superimposed on the induced upwash velocity due to the vortices in order to obtain the measured upwash velocity. Therefore, because the direction of the component of the freestream velocity is always along the negative Z_V-axis, the upwash velocity induced by the vortices equals the measured upwash velocity plus the freestream velocity component in the Z_V direction. This is the case for both of the vortex models of reference 30. A question arises regarding the validity of this assumption, since it is known that a large portion of the vortex is embedded in the wake and, because of the defect in the axial (X) velocity within the wake, the fluid elements in the wake are not moving as fast as the crossflow. Therefore, if the correct local wake velocities were used in the vortex models instead of a larger constant crossflow velocity, the vortices would be required to induce smaller upwash velocities and this in turn would reduce the strength of the vortex necessary to generate the induced upwash velocity.

In order to obtain an estimate of the reduction in the vortex strength which results from using the more correct wake velocities, test cases were calculated using data taken from figure 3 of reference 30 for $\lambda = 8$ and $X/a = 16$. The results, to be presented later in this chapter, show that, over the length of the vortex curve covered in the present investigation, the wake has a defect in the magnitude of the velocity vector (total velocity) of about 10% of the free-stream velocity. Using Fearn and Weston's[30] filament model, it can be shown that the reduction in the predicted vortex strength is approximately the same as the percent defect in the wake velocity. It is expected that a reduction in the vortex strength of approximately the same order will be realized using the diffuse model, because the assumption of constant crossflow velocity is also used by Fearn and Weston[30] for this model.

In light of the above, it seems reasonable to consider that the vortex strength values predicted by Fearn and Weston[30] and by Sellers[31] are too high by from 5 to 10%. It is interesting to note that no such uncertainty arose for Thompson[29] because one of his models required as input the V_{Y_V} component (circumferential velocity) induced by the vortices, and there is no component of the freestream in the Y_V direction. In his second model, the circulation was calculated by simply taking the line integral of the measured

tangential component of the velocity on a circuit enclosing the vortex.

With increasing streamwise distance from the jet exit, the wake grows with a decreasing defect in the wake velocities. Thus the overprediction inherent in the vortex models of Fearn and Weston[30] should decrease with increasing X/a. The vortex strength values of references 30 and 29 begin to agree at a distance, along the vortex curve, of about 30 jet diameters from the jet exit. To sum up, it seems reasonable to conclude that the correct vortex strength distribution, for $\lambda = 8$, falls near the upper limit of the error bands indicated on the data from the present investigation.

This completes the description of the contrarotating vortices associated with the jet in crossflow. Some further discussion about the interactions between the flow fields associated with the vortices, the jet, and the wake will be discussed in a later section.

Wake Region

Results are discussed in this section concerning the wake region behind the circular jet in crossflow. In this work, the wake is defined as the region within which the total pressure is lower than that of the freestream, and it is also the region where no significant jet fluid was

noted from the temperature measurements. The region extends from the flat plate to the jet plume, where it is affected by the flow field associated with the two contrarotating vortices. The interaction between the jet and the wake is discussed in the next section of this chapter; the wake region alone is discussed here.

The edge of the wake is defined as the contour inside of which the total pressure is at least one percent lower than the freestream total pressure. As mentioned in Chapter III, the Kiel probe rake measurements were used to obtain the edge of the wake. Figure 36 shows the wake edge at different X/a stations for λ = 8 and 10.7. As pointed out in the previous paragraph, the wake region in this work is defined as the region exclusive of the jet region, and, therefore, the surveys for the wake edge were limited in the positive Z/a direction to lie below the lower edge of the jet. It should be noted that station X/a = 22 is very near the end of the flat plate and hence the wake edge for that station may have been affected by possible three-dimensionality of the flow.

Figure 36 shows that, for any X/a station, the wake width gets smaller towards the jet (increasing Z/a). This is because the importance of the velocity field associated with the vortices increases as one approaches the jet. Thus, there is an increased entrainment of the high total pressure

freestream fluid into the wake region near the jet. Increasing λ by 30% does not affect the width of the wake, at least in the regions where the measurements were made; the height of the wake, however, does increase. Although increasing λ moves the vortex center away from any point in the wake, the vortex strength also increases (by about 30%) and therefore the influence of the flow field associated with the vortices at that point in the wake remains about the same.

Data points were taken very near the flat plate (between $Z/a = 0$ and 2) but, because of the total pressure loss in the plate boundary layer in this part of the region of the wake, no conclusions can be drawn about the wake width. However, in what follows, some typical total pressure profiles very near the flat plate surface are reported along with the total pressure profiles in the wake region away from the surface. The velocity distributions in the wake are presented after the total pressure distributions are discussed.

Total Pressure Profiles

Figure 37 shows typical profiles of the total pressure (obtained with the Kiel probe rake) very near the flat plate. With the jet off, a turbulent boundary layer with an approximate thickness of one inch exists in the region downstream of the jet exit. With the jet on, the boundary layer thickness increases to about 1.8 inches outside the wake

region (X/a = 7, Y/a = 3.5). The total pressure within the wake edge is lowest near the plane of symmetry (Y/a = 0) and, if one goes near the jet exit (X/a = 4, Y/a = 0), a separated or reverse flow is indicated in the profile. The oil pictures of Mosher[8] indicated regions of separated flow up to about Y/a = 3 for $\lambda = 8$.

Figure 38 shows typical total pressure distributions obtained using the 5-hole pressure probe in the wake region. In order to estimate the overall total pressure loss in the wake, these profiles were integrated. If I_{P_o} denotes the integral of the deficit in total pressure along Y/a, then

$$I_{P_o} = \int_0^{Y_{w\frac{1}{2}}/a} (\bar{P}_o - 1)\, d(Y/a) \quad .$$

Figure 39 shows the variation of the integrated total pressure loss, I_{P_o}, with Z/a for two X/a stations. It is seen that as the wake nears the domain of the jet (i.e. larger Z/a) the integrated losses within the wake reduce because of the increased entrainment of freestream fluid as argued earlier. Furthermore, for the regions where data were available, it was found that the integrated losses in the wake are not necessarily smaller if one goes further downstream (X/a = 15) at a given Z/a. In the present flow configuration, the low energy fluid in the wake has a tendency to travel upwards

(away from the flat plate and towards the jet) along with its travel downstream (as indicated by the data of Jordinson[21] and results to be presented next). Therefore, at a given Z/a, the defect in the total pressure is greater at station X/a = 15 than at X/a = 11.

Velocity Distributions

The distribution of the magnitude of the velocity vector (the total velocity, V) for the plane of symmetry in the wake is presented in Figure 40. A value of V/V_∞ greater than unity represents a region in the jet, whereas V/V_∞ less than unity indicates the wake region. Near the flat plate (Z/a = 4) in the wake region, the rate of recovery of the total velocity with increasing X/a is very low. However, the rate of recovery increases for larger values of Z/a in the region near the jet exit. The decrease in total velocity with increasing X/a for the vertical station Z/a = 10 represents a transition from a jet region to a wake region.

The distribution of the axial (X) velocity component of the flow in the wake, for the plane of symmetry, is shown in Figure 41. The corresponding velocity vectors in the plane of symmetry are shown for the wake region in Figure 42. The axial velocity, V_X, increases in the wake with increasing X/a. The value of V_X is lower near the jet than near the flat plate for X/a < 18 because the component of the velocity

in the Z direction (V_Z) increases with increasing Z/a due to the increasing dominance of the vortex flow field on the velocity field in the wake.

The results presented above concerning the wake edge and the total pressure and velocity distributions complete the description of the wake in the present investigation. Next, the size of the wake as inferred from the present data is compared with the wake region seen in the surface oil pictures of Mosher[8].

Comparison with Oil Pictures

In the oil pictures taken on the flat plate by Mosher[8], downstream of the jet exit one can see a darkened area which increases in size with increasing X/a. These pictures represent the behavior of the boundary layer on the flat plate. It can be seen in Figure 36 that, for $\lambda = 8$, if one extrapolates the wake edge of the present investigation to Z/a = 0 they closely match with the half-widths of the darkened region obtained from the oil pictures[8]. This implies that, for $\lambda = 8$, the extent of the darkened region, within which the behavior of the boundary layer on the flat plate is different from the behavior of the freestream boundary layer, is about the same as that of the wake region found off the plate surface. However, as shown earlier, increasing λ from 8 to 10.7 does not increase the width of the wake off the surface whereas the width of

the darkened regions of the oil picture[8] for any X/a station increases as $\lambda^{\frac{1}{2}}$. Thus, it may be concluded that the width of the darkened regions in the oil picture is not necessarily the same as the width of the wake region outside of the boundary layer. However, the width of the wake region outside of the flat plate boundary layer is not greater than the width of the darkened regions seen in the oil pictures taken on the flat plate surface.

General Interacting Flow Fields

In what has preceded in this chapter, the extent and the shape of the jet region were first determined, along with a measure of the parameters describing the contrarotating vortices. Secondly, in this chapter, the wake region was defined and its extent obtained as a region independent from, but considered not unrelated to, the jet region. A typical cross section of the jet in a Y-Z plane, illustrating the extent of the different regions (with the prior assumption of them being independent), is shown in Figure 43. In what follows, the assumption of the regions being independent is removed, and further results are presented and discussed for the overall flow field containing the jet and the wake.

Figure 43 and the next four figures represent the typical behavior of the jet at various X/d stations. The data shown in Figures 44 through 47 are for an X/d station

of 5.5, and were obtained using the 5-hole pressure probe. Figure 44 shows the projection of the local velocity vectors in the Y-Z cross section. The figure essentially covers the region between the rolled-up vortices and the wake. It is evident from the figure that the lateral flow (in the Y direction), primarily associated with the vortices, passes through the wake region. It is also apparent that there is no significant blockage to the lateral flow because of the wake. This is in contrast to the indications from the oil pictures (Reference 8) where the streamline patterns in the oil on the plate surface show significant blockage due to the wake.

The flow field within the wake region also has a velocity component towards the jet (i.e. in the positive Z direction) which seems to persist down to at least a height of the order of the boundary layer thickness on the flat plate. This can be seen in Figure 42 and also in Figure 45, which shows contours of constant upwash angle, α, in the same Y-Z cross section. This upwash in the wake is attributed to the nature of the velocity field associated with the contra-rotating vortices. As might be expected, the maximum upwash occurs in the region between the vortex centers.

Figure 46 shows contours of constant total and static pressure, while contours of constant total and axial velocity are shown in Figure 47. These two figures, in conjunction with Figure 43, reveal that within the jet region the total

velocity is higher than the freestream velocity, as would be expected. However, the total pressure contours show that there is a region within the jet where the total pressure is lower than the freestream. (It can be as low as the total pressure levels in the wake for corresponding axial stations; however, the severity of the total pressure defect within the jet diminishes at a faster rate than for the wake for downstream X/a stations.) It is obsereved that this region of low total pressure in the jet is situated under the main body of the jet (i.e. under the jet center) and above the vortex centers. Furthermore, it can be seen that, in this region, the total velocities are lower than for the surrounding regions in the jet. It is the combination of low total velocity in that local region and low static pressure in the whole jet which leaves a pocket of low total pressure in that region of the jet.

The maximum total velocity is attained near the vortex centers rather than in the main body of the jet after the jet travels a few diameters from the exit, whereas the total pressure is higher in the main body of the jet than it is within the vortices. The static pressure distribution shows that the static pressure in the jet is lowest around the vortex centers (because of the higher total velocities) and the static pressure levels are much lower in the jet than in the wake. Axial velocities are lowest between the vortex

centers, the region where maximum upwash occurs, and highest in the vortex cores.

The total velocity and total pressure contours indicate that the effect of the vortex motion is the dominant mechanism by which the mixing of the jet and the crossflow occurs. The region of total pressure (within the jet) which is lower than the freestream value seems to arise from the mixing of the jet fluid in the vortices and the fluid in the wake region. The wake region, as defined in the present investigation, has a flow field which is influenced by the velocity field of the vortex motion. In the jet region the velocity and the temperature are always higher than that of the freestream. This is not true of the total pressure.

Entrainment

The jet entrains the crossflow fluid as it expands along its length, and one of the problems of interest is to find the rate of entrainment and the principal mechanisms.

From reference 23, if m_T is the mass flux in the turbulent region of an axisymmetric free jet and r_T is the radius of the turbulent region, then the rate of change of the mass flux along the length, s, of the jet is given as

$$\frac{dm_T}{ds} = 2\pi\rho r_T U_e \tag{24}$$

where U_e is the mean velocity at which the turbulent front of the jet is advancing into the non-turbulent region of the freestream flow. U_e is called the entrainment velocity and represents the rate of entrainment due to the free-jet type expansion.

For free-jets and wakes, U_e varies as

$$U_e = E(U_{max} - V_\infty) \tag{25}$$

where U_{max} is the maximum velocity component parallel to the jet path for a jet cross section (normal to the s direction) and E is the entrainment constant which has a value of 0.045 for free jets.

For the jet in crossflow, Equation (24) can be applied to represent the entrainment process (with r_T considered as some equivalent radius of the turbulent region of the jet)[23]. However, if one attempts to obtain an equation for U_e of a form similar to Equation (25), no constant value of E can be obtained even for a constant value of the effective velocity ratio, λ, (Reference 23) and the values of E which are deduced are much higher than the value for the free jet. Therefore, references 23 and 18 have both suggested that the entrainment process should be represented by two modes, namely, the free-jet type of entrainment and an entrainment due to the action of the

crossflow component normal to the jet path.

Kamotani and Greber[23] assumed a form for U_e as

$$U_e = E_1(U_{max} - V_\infty \cos \theta) + E_2 V_\infty \sin \theta \qquad (26)$$

where θ is the local angle between the jet velocity centerline and the crossflow. The first term in the entrainment velocity represents the action of the parallel component of the crossflow on the jet and hence the free-jet type of entrainment. The second term is due to the normal component of the crossflow acting on the jet, and it is assumed by the $\sin \theta$ dependence that this portion of the entrainment velocity is maximum at the jet exit and reduces along the length of the jet. The authors[23] attempted to obtain the values of the constants E_1 and E_2 by measuring the mass flux increment along the jet path and then using Equations (24) and (26). The difficulty encountered was to define the extent of the turbulent region of the jet. Since the major aim had been only to obtain the variations in E_1 and E_2 which represent the variation in U_e along the jet path, the turbulent region was defined as the region bounded by a contour which had 10% of the axial (along the jet path) velocity compared to the maximum axial velocity for a cross section normal to the jet path. It was found that the empirically determined values of E_1 and E_2 remained constant

along the jet path for a particular value of λ. It was reported that for, $\lambda = 8$, $E_1 = 0.067$ and $E_2 = 0.18$ are probably close to the correct values because the jet region occupies nearly the whole turbulent region.

Platten and Keffer[18] noted that the physical mechanism behind the second mode of entrainment is the circulation pattern of the jet flow field sweeping the crossflow fluid first into the central region of the wake and then into the jet.

The physical mechanism of the second mode of entrainment of the crossflow fluid into the jet has been sought in the present investigation. If the argument of Platten and Keffer[18] is true, E_2 can be calculated from the mass flow rate associated with the vortex flow field. Using the measurements made in this study, this concept can be evaluated by assessing the capability of the vortex motion to entrain the additional freestream fluid over and above the free-jet type of entrainment.

In the analysis, the first step is to estimate whether, for any Y-Z cross section, the measured lateral (in the Y direction) inflow (towards the plane of symmetry) of freestream fluid from outside the jet region can be related to the flow field associated with the pair of vortices whose strength has been measured. The regions of freestream fluid affected are well outside the cores of the

vortices. Thus, neglecting the effect of the flat plate, the lateral inflow velocity due to the vortex flow field may be calculated by using the Biot-Savart law for a two-dimensional, potential vortex pair whose strength and position are known from measurement. Figure 48 shows a comparison between the measured and calculated lateral velocity distribution for a cross section in the Y-Z plane for which the necessary data are available. It can be seen that a major portion of the measured inflow can be attributed to the vortex velocity field alone. The small difference might be either because of the three-dimensionality of the vortex system or because of some momentum transfer related to the pressure forces prevailing in the actual case but neglected in the analysis.

The second step is to calculate the mass flux of the lateral inflow of the freestream fluid per unit length of the jet. The mass flux was calculated from the lateral inflow measured at two stations, $X/d = 5.5$ and 7.5. Notice from Figure 48 that no data were available for Z/a less than 4, so the measured distribution was extrapolated up to the edge of the flat plate boundary layer ($Z/a = 2$). The calculated mass flow rate was then used in the next step.

The third step is to see what happens to the lateral inflow of the freestream fluid. Assuming that there is no mass transferred across the plane of symmetry, the total

lateral mass inflow in the wake region between the two stations X/d = 5.5 and 7.5 either has to go through the wake and up towards the jet or be carried along in the wake, thus increasing the axial (X) mass flow rate in the wake. In order to find out what happens to the mass flow coming into the wake, a control volume was constructed in the wake region whose surface consisted of X/d of 5.5 and 7.5, Y/d = 0 and the half-spacing of the vortex, and Z/d = 1 and 9 (wake height at X/d = 5.5). The mass flow rate was calculated across the different surfaces using the velocity measurements. It was estimated that about 10% of the mass inflow of the freestream fluid into the wake region is carried along (increases the axial mass flow rate) in the wake and about 90% of the mass goes up through the wake and enters the jet in the form of a V_Z component of velocity. This means that 90% of the lateral mass inflow of the freestream fluid into the wake region, which is related to the flow field associated with the vortices, gets entrained in the jet. If E_2 is calculated from this approach (first using Equation (24) to obtain U_e due to the vortex and then comparing that value of U_e to the second part of Equation (26)), a value of 0.14 is obtained for $\lambda = 8$ which is slightly smaller than that reported in reference 23. No conclusion can be drawn as to whether E_2 remains constant along the jet because of

the limited data available in the present investigation.

It is concluded that in the jet in crossflow, the entrainment process should be represented by two modes: namely, a free-jet type and a crossflow type. The second mode can be represented mathematically by Equations (24) and (26). However, the physical reason behind the second mode is the presence of the vortex flow field which enhances the entrainment of the freestream fluid into the jet. The above analysis represents only a simplistic approach with the assumptions that the vortex is two-dimensional and potential, and with the goal of understanding the complex phenomenon of entrainment. It has been suggested that the real physical model consists of a pair of vortices which entrain the freestream fluid by means of sheets of vorticity rolling up and enclosing the freestream fluid between them.

Physical Picture of the Flow Field

In this section, the experimental information presented in the previous sections of this chapter is used in conjunction with findings of other investigators to formulate a general description of the behavior of the entire flow field of the circular jet in crossflow. For convenience, the discussion is divided into three sub-sections. These sub-sections describe the following :

1) Initial region near the jet exit,

2) Intermediate region,

3) Far-field region.

For sub-sections 1 and 2, very little experimental information is available, and therefore some hypotheses are made to describe the behavior of the flow field associated with the jet. The present investigation essentially covers the intermediate region of the jet. The physical picture is based on findings for $\lambda = 8$. Hence, the application of the physical picture to other cases with different λ values should be made with caution, particularly in the cases with low λ values (~ 2) in which the effect of the flat plate on the flow field may be significant. Statements including reference number are the ideas suggested by other investigators. The follow-up arguments represent the author's opinions.

Initial Region

Near the exit of a jet which exhausts normally to the crossflow, a stagnation region in the front of the jet[8], acceleration of the crossflow around the jet[8], and flow reversal[8] leading to entrainment of the crossflow fluid behind the jet[22] are present. Within the jet, a core of constant velocity is present whose length depends on λ (Reference 23) but which is less than that for a free jet. At the end of the core, the velocity and total pressure in the center of the jet start decaying sharply. No distortion

in the shape of the jet can be seen, at least upto one exit diameter of jet travel. However, a definite distortion can be seen at about two jet diameters along the length of the jet, which is approximately the length of the core for $\lambda = 8$. A pronounced distortion of the shape of the circular jet into a "kidney" shape takes place within three jet diameters travel of the jet.

Unfortunately, almost no experimental information is available which would help to predict the initial formation of the contrarotating vortices. However, there are some observations, based on theoretical calculations, which can provide some insight regarding the behavior of the vortices in the initial region.

For a two-dimensional, potential flow around a circular cylinder of diameter d, the circulation on semi-circles (split about the diameter parallel to the freestream) is $2dV_\infty$[29, 32]. Considering the similarity in the observed flow field, it is possible that the initial circulation of each vortex in the pair for a circular jet in a crossflow might also be equal to that generated by a circular cylinder with d as the jet exit diameter[29, 32]. Therefore, in such a case, the nondimensional vortex strength, γ, would be equal to unity right at the jet exit for any λ. However, in a real flow situation, because of a free-streamline separation about the initial part of the jet producing the wake region, and

because the real flow is truly three-dimensional, the correct value of the nondimensional initial vortex strength will not be exactly unity but should be of order unity[29].

Regarding the initial spacing between the contra-rotating vortices, there are no well defined trailing vortex patterns in the initial region, but a "center of gravity" of vorticity can be obtained from the potential flow theory (for a flow around a circular cylinder) which is at a distance $\pi/2$ from the center of the jet[29]. In the real flow situation, it should always be equal to or greater than the radius of the jet. How much the vortices are diffused right at their initiation is unknown but the diffusion is probably negligible.

The above represent predictions about the status of the contrarotating vortices very near the jet exit where no experimental information is available.

Measurements show that the nondimensional vortex strength, γ, of the contrarotating vortices does have a value greater than unity after a certain distance from the jet exit. Excepting regions very near the jet exit, γ decreases along the length of the vortex. If $\gamma \simeq 1$ is a true initial condition for the circulation of the vortex near the jet exit, γ will increase from unity to a maximum value at some point along the length of the vortex and then it will decrease. The region of the jet beyond the maximum point of γ is essentially

the intermediate region as it is defined in this section. No specific investigations have yet been reported which would aid in understanding the physical mechanisms governing the initial increment and then decrement in the vortex strength. However, some arguments are advanced here to help explain such a behavior. It should be borne in mind that these arguments may represent only one of the possible phenomena occuring in the complex flow situation.

The turbulent shearing action of the crossflow on the jet near the exit appears to begin at the lateral sides of the jet and, because of this action, there is entrainment of the crossflow fluid into the jet[21], the crossflow being entrained into the lateral and downstream edges of the jet. The mixing region deflects more than the core of the jet because there is more freestream fluid entrained into the former region. This process leads to the distortion in the shape of the jet[21]. Data show that the centers of the rolled-up vortices are located in the middle of the legs of the kidney shape of the distorted region. Thus, it can be assumed that the mixing region on the sides of the jet rolls up into a pair of contrarotating vortices. Secondly, if the circulation associated with these vortices is due to the blockage effect of the jet, then the initial circulation at the jet exit may be considered equal to that generated for a flow around a circular cylinder, as explained earlier in this

section. As long as the jet blockage effect is significant along the length of the jet, the circulation associated with the vortex motion may continue to increase. However, the rolled-up vortices also begin to diffuse (the size of the core radius increases), the vorticity in each vortex spreads outwards, and the vorticity field of each vortex interacts and, hence, cancels with that of the other[30]. For a certain distance, which seems from available data to be less than about 10 jet diameters for $\lambda = 8$, the increase in the circulation because of the additional generated vorticity is greater than the cancellation of vorticity because of the mutual interaction between the vortices; at distances greater than 10 diameters the opposite is true. Thus, a maximum in γ should be attained where there occurs a balance between addition and cancellation. After the maximum, the cancellation effect dominates because the vortices have diffused significantly while the jet has deflected by a large amount. A gradual weakening of the vortices on both sides of the jet ensues.†

After about 3 jet diameters, and onwards, the contrarotating vortices are the dominant feature of the flow field associated with the jet. The maximum total velocity

---

† Subsequent to the writing of this dissertation, a paper by Moussa, Trischka, and Eskinazi appeared in the Journal of Fluid Mechanics (Reference 50) which provides additional information on the origin of the pair of contrarotating vortices.

is attained near the vortex centers rather than in the main body of the jet after the jet travels a few diameters from the exit[23]. However, in the initial region, the main body of the jet maintains the maximum total pressure.

Behind the jet exit, downstream of the region of flow reversal, a flow with a total pressure lower than that of the freestream exists because of the viscous effects arising from the presence of the solid wall (the flat plate). This wake region is of considerable height (in the Z direction) and the flow field within the wake is significantly affected by the vortex flow field.

Intermediate Region

The results of the present investigation essentially describe the behavior of the flow field in this region. Within the jet, the contrarotating vortices gradually become larger, each vortex core being greater than three jet diameters in extent and increasing at a rate $X_v^{\frac{1}{2}}$. Initially, the vortex core is not well defined near the regions where the vortex and the main body of the jet mix. However, the contrarotating vortices soon become distinct and represent a dominating feature of the flow field. Because of the diffusion of the vorticity, the strength of the vortex reduces at the rate of erf(βh) along the length of the vortex. The maximum circulation associated with each vortex of the pair can have a value as large as four to five times that of

the initial circulation, $2dV_\infty$, before it reduces slowly in the intermediate region. The spacing between the vortex centers increases slowly because of the growth of the jet region.

The overall extent of the jet has already grown to a considerable size at the end of the initial region, and the jet maintains a distinct "kidney" shape because of the presence of the vortices. The flow angles, with respect to the freestream, within the main body of the jet remain essentially constant for a short distance in the intermediate region, and the main body of the jet retains its own character. However, by about 20 jet diameters the effect, near the jet center, of the velocity field associated with the vortices is comparable with the velocity field associated with the main body of the jet. By 30 to 40 jet diameters along the length of the jet, it becomes very difficult to recognize the main body of the jet because no large total pressure is observable.

In the intermediate region, the wake grows slowly in width and height. The width is smaller near the jet than near the flat plate. The maximum defect in total pressure in the wake is about 30% of the freestream total pressure, and the changes in total pressure in the downstream direction within the wake are small. The velocity field in the wake away from the flat plate is very much dominated by the flow

field associated with the contrarotating vortices. The upper portion of the wake mixes with the jet primarily through vortex action. Near the flat plate within the wake, some vortices, of rather small strength, are shed from the jet near the exit and some periodicity in the fluctations in the flow exists[39]. Because of the three-dimensionality of the flow in the vicinity of the flat plate and the jet near the jet exit, the wake region may also have some streamwise vortices lying along the flat plate.

Far-Field Region

At a large distance from the exit, the jet asymptotically approaches a state in which it has deflected completely. The main body of the jet and the wake lose their individual character completely, and the contrarotating vortices are the only observable features in the entire flow field. It is of interest to estimate the magnitude of the circulation of the contrarotating vortices in such a limiting case. Theoretically, this situation is reached only in the limit as the jet length approaches infinity and the vortices diffuse and vanish completely. However, in order to estimate the parameters associated with the contrarotating vortices, assume that the limiting situation is one in which the vortices are beginning to move parallel to the crossflow and are travelling at the crossflow velocity. A reasonable criterion would be that the limiting case is effectively

reached when the jet has deflected to within one degree with respect to the crossflow and the only character of the jet remaining is the contrarotating vortices. This criterion allows one to study the behavior of the vortices at a finite, but large, distance from the jet exit.

Assume that the equivalent lift of an imaginary wing replacing the pair of vortices in the limiting case should be equal to the initial jet momentum[27]. From the conservation of momentum in the vertical (Z) direction[27]

$$\rho V_\infty \Gamma_f (2h) = \frac{\pi}{4} d^2 \rho_j V_j^2$$

where Γ_f is the final effective strength of each vortex and 2h is the spacing between the vortex centers in the limiting case.

Consider a nondimensionalized version of the above equation for the purpose of discussion, namely,

$$\gamma_f = \frac{\pi}{16} \frac{1}{(h/d)} \lambda^2 \quad . \tag{27}$$

Observe that the final vortex strength, γ_f, is inversely proportional to the spacing, as is expected. However, the parabolic dependence of γ_f on λ is noteworthy because the vortex strength varies linearly with λ (Reference 30) near the end of the initial region. In

contrast, h/d varies only slightly with λ in the intermediate region, the variation being weakly dependent and going as $\lambda^{0.3}$ according to the measurements of reference 30. Then, assuming the same dependences in the limiting case, γ_f would vary approximately as $\lambda^{1.7}$.

For $\lambda = 8$, an h/d value of 16.5 is obtained as a measure of the limiting case from the empirical relationship between h/d, X/d,and λ (Reference 31). This is about 1400 jet diameters along the length of the jet, where the jet makes an angle of 1° with the freestream. At that location, γ_f is calculated to be about 0.76 from Equation (27) compared to the initial value of unity. It can also be determined from the above equation that $\gamma_f = 1$ is attained at about 900 diameters downstream of the jet exit. At that station the flow field is not too far away from the limiting situation, because the jet is deflected only about 1.3° with respect to the crossflow. Hence, for a very large distance along the jet, from very near the jet exit onwards, the vortex strength is higher than the circulation, $2dV_{\infty}$, associated with a two-dimensional, potential flow around a circular cylinder.

With increasing λ the jet deflects to the limiting case (i.e. within a degree to the crossflow) at an increasingly longer distance. Therefore, if the flow field associated with the contrarotating vortices is considered significant until the limiting situation is reached, then

such a region of significance is larger for larger values of λ. Secondly, the $\lambda^{1.7}$ dependence of γ_f suggests that, even though the vortex strength near the end of the initial region is directly proportional to λ, once the vortex strength attains a maximum the subsequent decay process will be slower for larger λ values than one would expect judging from the linear relationship which holds in the initial region.

CHAPTER V

CONCLUSIONS AND RECOMMENDATIONS

On the basis of the present experimental investigation of the jet in crossflow, the following conclusions are drawn :

1. The roll-up of the contrarotating vortices distorts the shape of the circular jet to a kidney shape. No significant roll-up occurs for at least one jet diameter of travel of the jet. A substantial roll-up of the vortices has taken place by three diameters travel.

2. The location of the contrarotating vortices measured with the vortex meter is in close agreement with that predicted from velocity measurements.

3. The distributions of vorticity show that the contrarotating vortices interact significantly with the main body of the jet. The regions of interaction begin near the edge of the vortex core and, as a result of this, the core of the vortex is not well defined near the main body of the jet.

4. The magnitude of the vortex core radius and, hence, the rate of diffusion of the vortices predicted by the diffuse vortex model of reference 30 is in good agreement

with the values measured with the vortex meter. However, an assumption of two-dimensionality of the vortex is needed to obtain the core radius in both cases.

5. The vortex core is of a considerable size and occupies a region about three to four jet diameters in extent on either side of the jet. Thus the contrarotating vortices are a major feature of the jet flow field.

6. The vortex strength values obtained in this study using the vortex meter agree well with the values of Thompson[29], who made use of the velocity measurements to calculate the vortex strength. The discrepancy between the strength values predicted by the vortex models of Fearn and Weston[30] and the values measured in the present investigation is not insignificant.

7. It is confirmed through the present study that, over a majority of the length of the vortex, the strength of each vortex reduces because the vorticity field of each diffusing vortex in the pair interacts with the other.

8. Downstream of the jet exit there is a wake region of considerable size; this region does not contain any appreciable jet fluid. The width of the wake increases with increasing X/a. Because the significance of the velocity field associated with the vortices increases nearer the jet region (larger positive Z), the wake is narrower near the jet than it is near the flat plate.

9. The velocity field in the wake is considerably influenced by the flow field associated with the contra-rotating vortices. There is no indication that the wake has a blockage effect on the lateral inflow of the free-stream fluid.

10. In the jet region, the velocity and the temperature are always higher than their freestream values. This is not true of the total pressure. The static pressure is lower near the vortex center than anywhere else in the flow field, including the wake.

11. The physical mechanism behind the added entrainment (over and above the free-jet type entrainment) in the jet in crossflow is the presence of the vortex flow field which enhances the entrainment of freestream fluid into the jet.

12. The temperature centerlines of the circular jet do not coincide with the corresponding jet velocity or total pressure centerlines because of gradients in the static pressure across the jet caused by the vortex flow field.

13. Even though vortices can be seen to be present in the temperature field of the streamlined jet, the temperature and the jet total pressure centerlines in this case are very close to each other.

Regarding the measurement technique employed to study the contrarotating vortices in the present tests, the following conclusions are drawn :

1. For an extensive study of a jet in crossflow in which the aim is to find the effect of parameters like λ and the jet exit shape on the behavior of the contra-rotating vortices, a limited use of a vortex meter and a velocity probe is sufficient to provide the basic information about the vortices. More specifically, the vortex curve can be obtained from velocity measurements in the plane of symmetry. Then, in planes normal to the vortex curve, the center of the vortex be found initially by trial-and-error. After locating the vortex center, the value of vorticity at the center can be obtained using the vortex meter and the vortex core radius can be obtained by measuring the circumferential velocity distribution along a traverse through the vortex center. Knowing the value of the axial velocity at the vortex center improves the accuracy of the vortex meter data. These limited measurements, along with an assumption of two-dimensionality of each vortex, are sufficient to provide adequate information regarding the parameters of interest for the contrarotating vortices.

2. The vortex meter is a very useful tool to investigate detailed distributions of vorticity. In the jet in crossflow, the axial velocity values should be obtained

along with the vortex meter data to get more precise vorticity distributions. This type of data should help to explain the areas of the interaction between the vortices and the main body of the jet. The drawback of the vortex meter is the time-consuming process involved with lubrication of the meter and the frequent checks needed to assure its accuracy.

Based upon knowledge gained in the present study, the following recommendations are made :

1. For the circular jet, a detailed investigation of the jet in the region near the jet exit to study the origin of the pair of vortices should be made. Because of the very high turbulence intensity in that region, use of a probe capable of measuring time-varying quantities is required.

2. The behavior of the flow field in the wake region very near the flat plate should be studied.

3. For the streamlined jet, temperature measurements should be made near the jet exit to study the vortex roll-up in the X-Y plane. The area of particular interest is the downstream side of the jet, where the behavior is found in the present investigation to differ from that of the circular jet.

Table 1. Jet Velocities and Reynolds Number for Nominal and True λ (V_∞ = 50 fps)

λ		V_{j_e} fps	R_{j_e}
Nominal	True		
4.0	4.08	214.4	1.5×10^5
8.0	8.16	428.8	3.0×10^5
10.7	10.92	562.3	4.0×10^5
12.0	12.24	643.2	4.6×10^5

Table 2. Constants for Jet Centerline and Vortex Curve Equations

Reference	λ Coverage	Jet Centerline			Vortex Curve		
		a_1	a_2	a_3	a_1	a_2	a_3
Present	8.16	1.00	1.00	0.40	0.50	1.00	0.53
29	2.3,4.0,8.1	1.46	0.93	0.34	0.66	0.94	0.46
30	3-8, 10	0.98	0.91	0.33	0.52	1.13	0.43

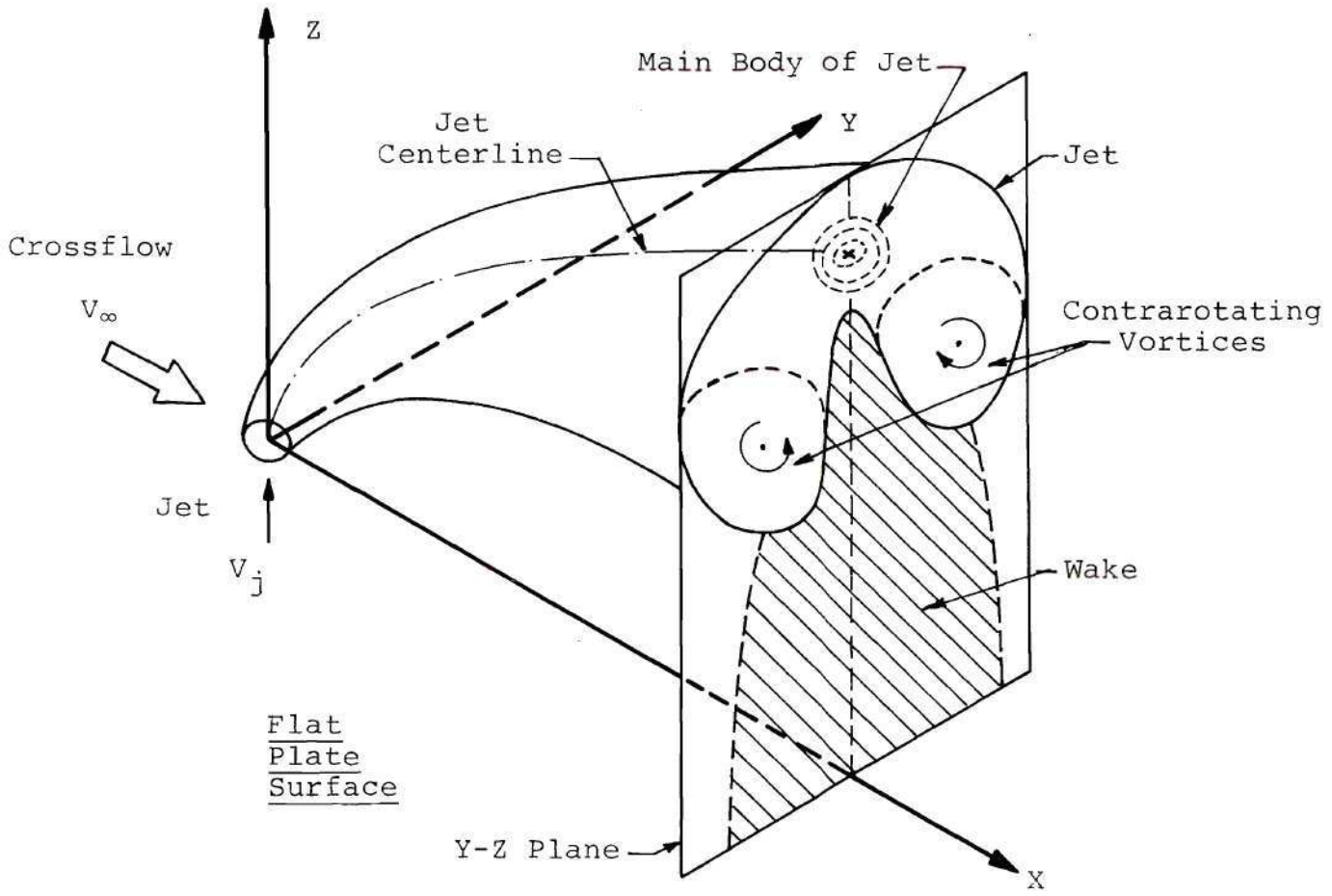

Figure 1. Schematic Diagram of Jet and Wake Regions.

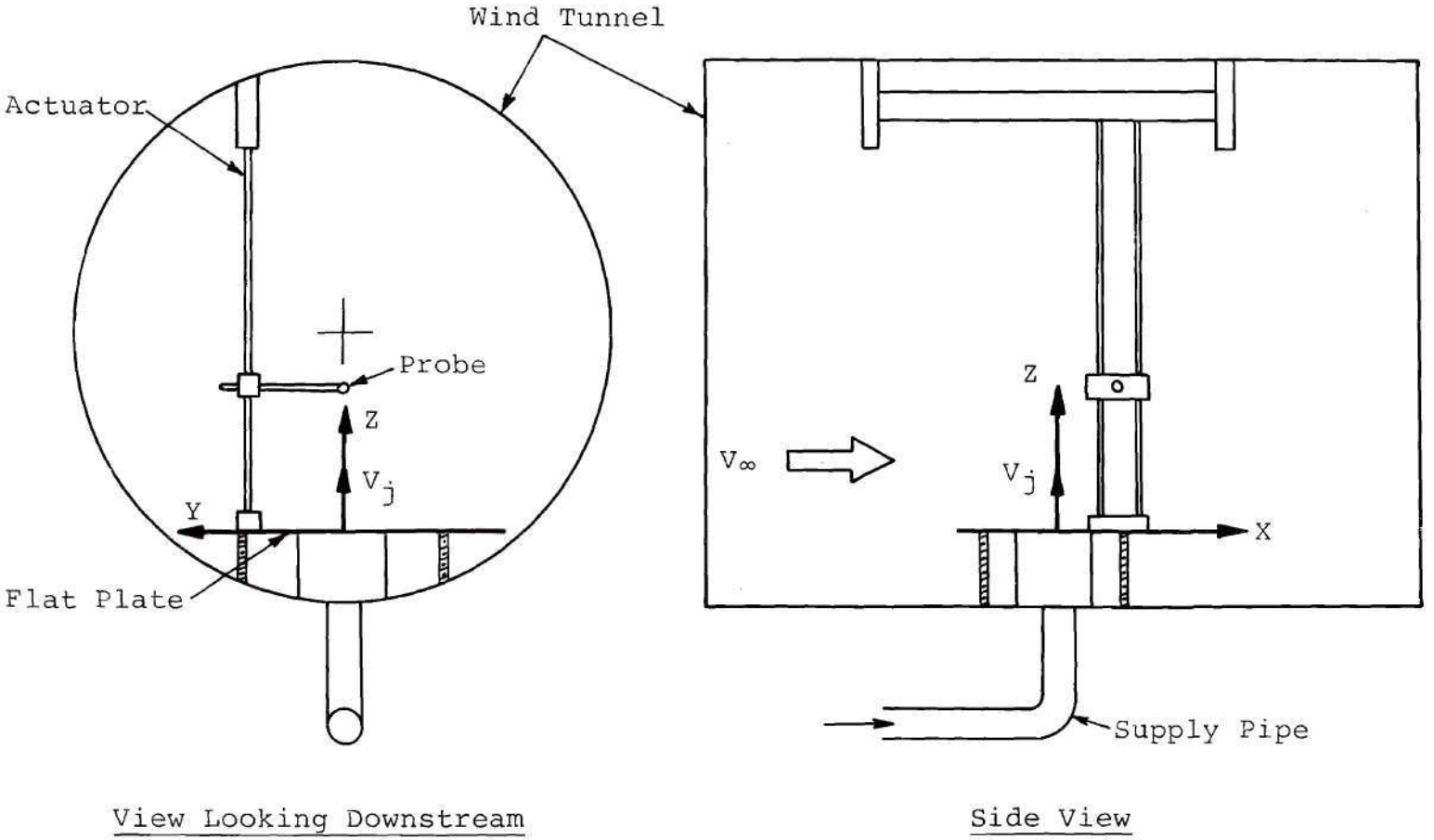

Figure 2. Schematic Diagram of Test Apparatus in the Wind Tunnel.

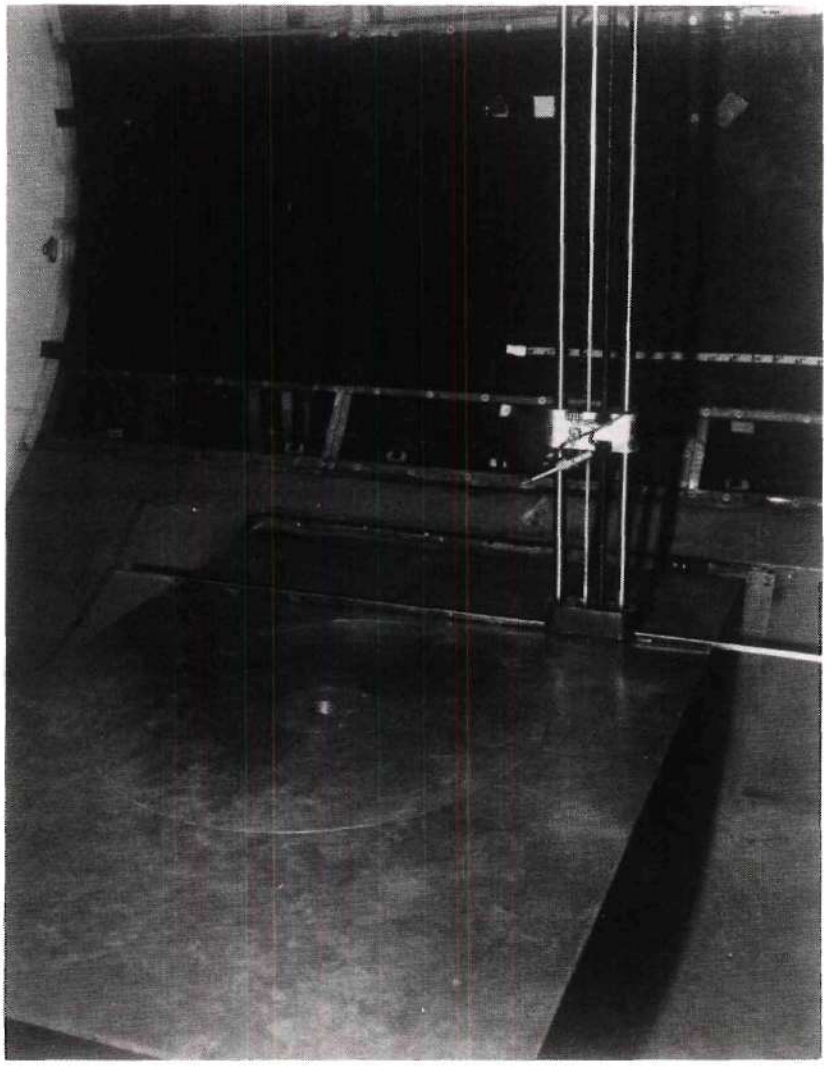

Figure 3. View of Flat Plate and Nozzle Block.

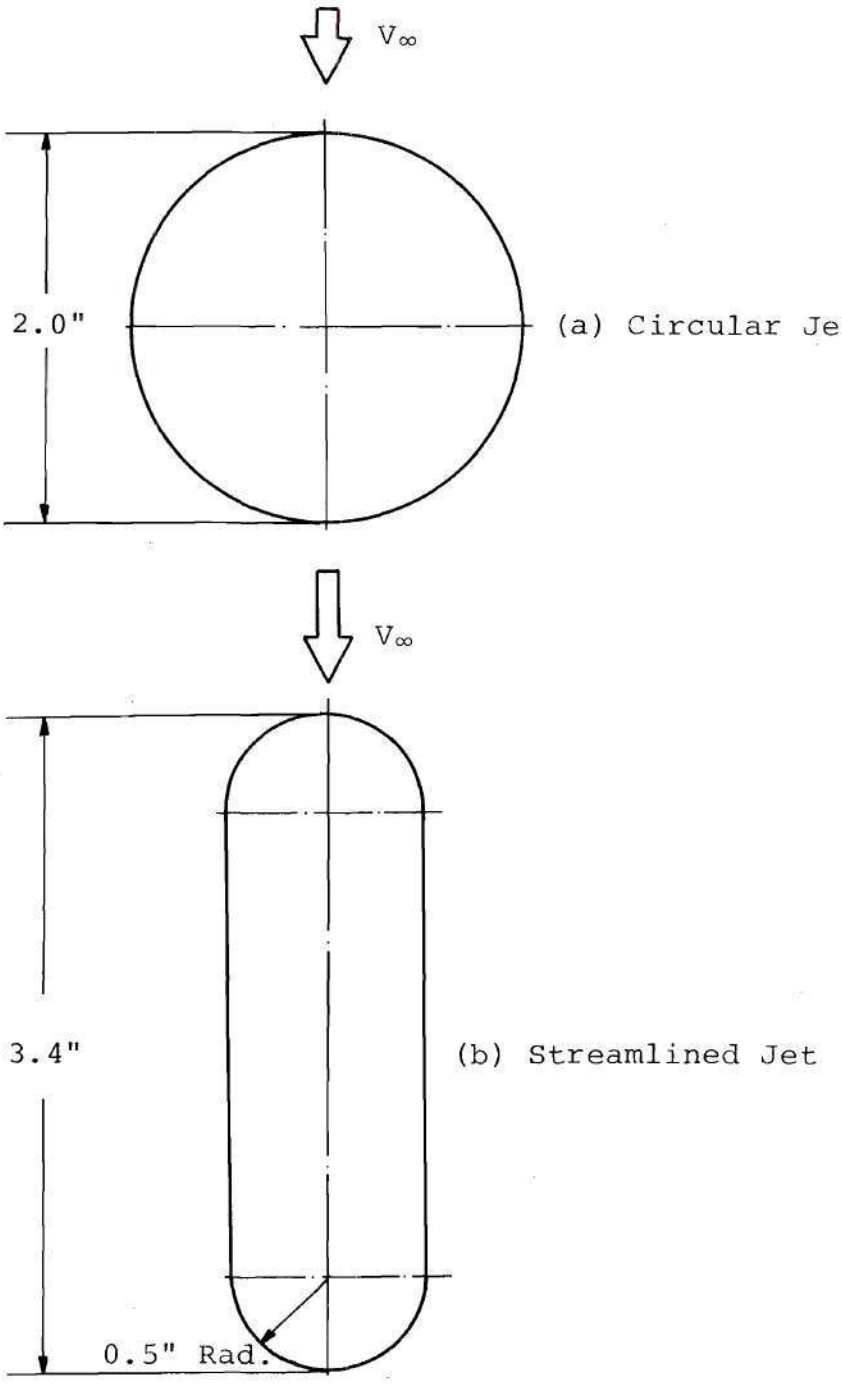

Figure 4. Jet Exit Configurations.

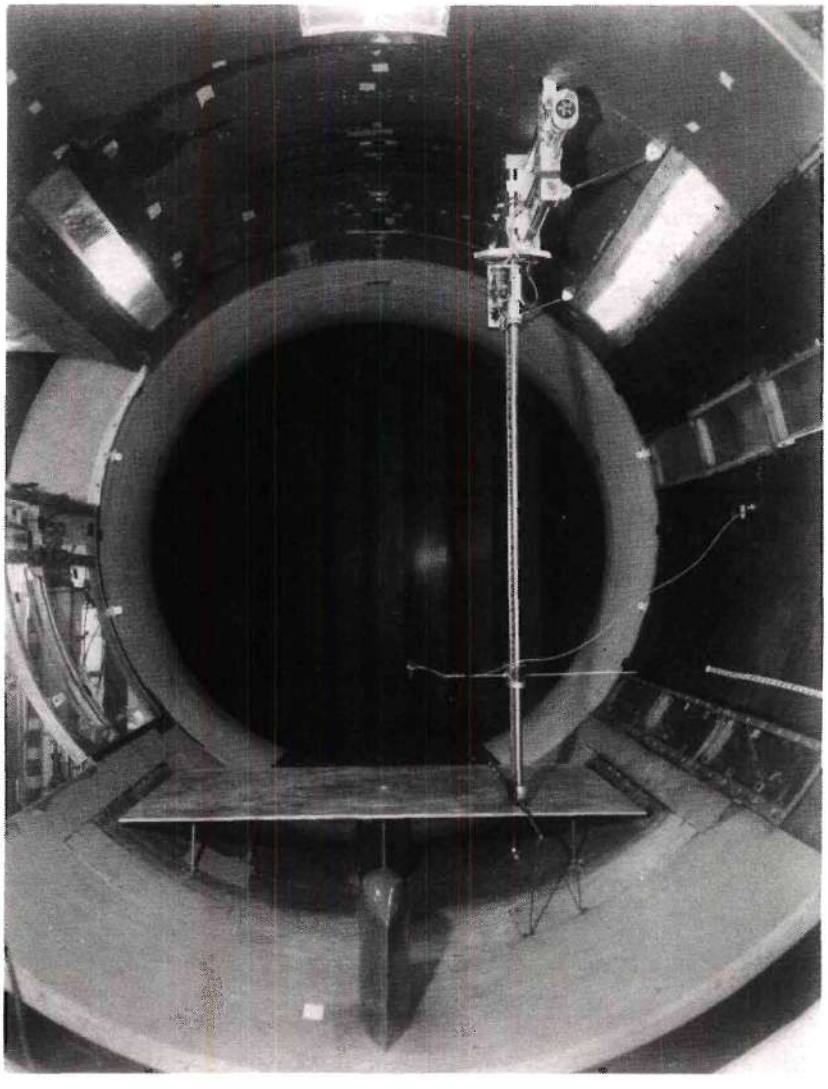

Figure 5. Flat Plate and Actuator Installed in Wind Tunnel (View Looking Upstream).

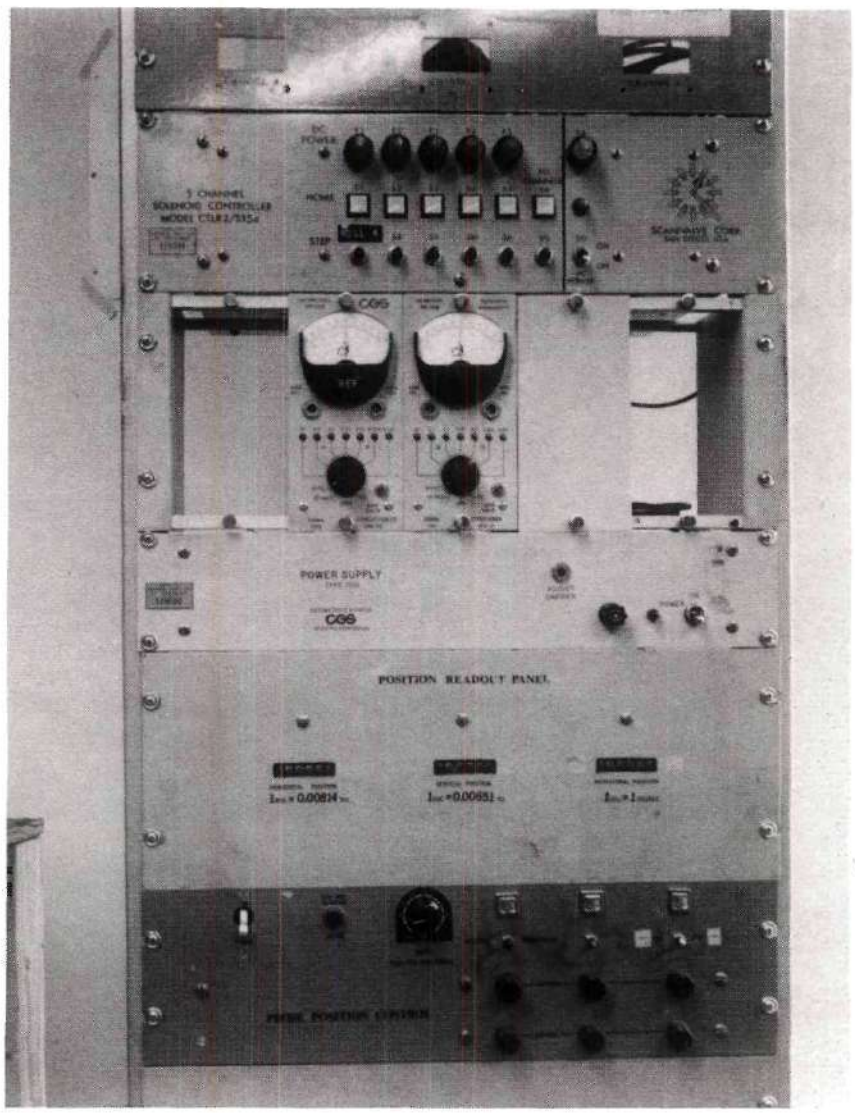

Figure 6. Instrument Panel with Actuator Control and Read-Out Counters.

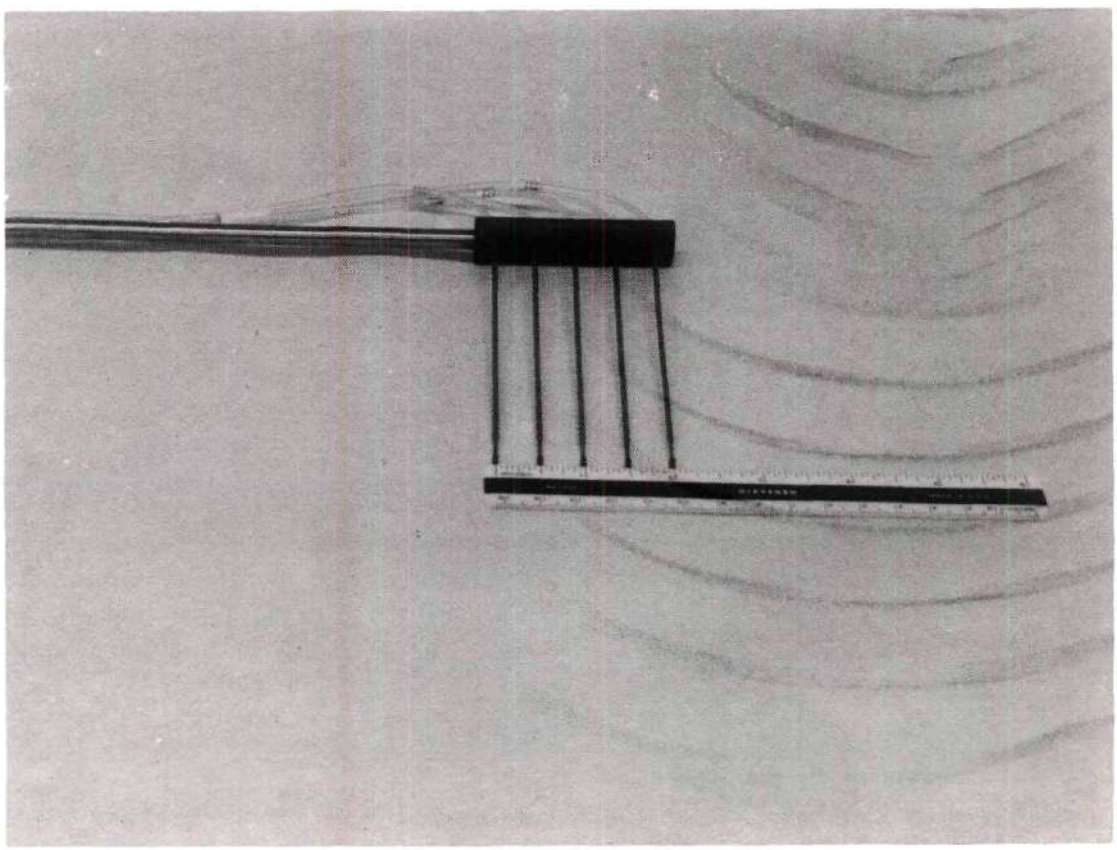

Figure 7. Kiel Probe Rake.

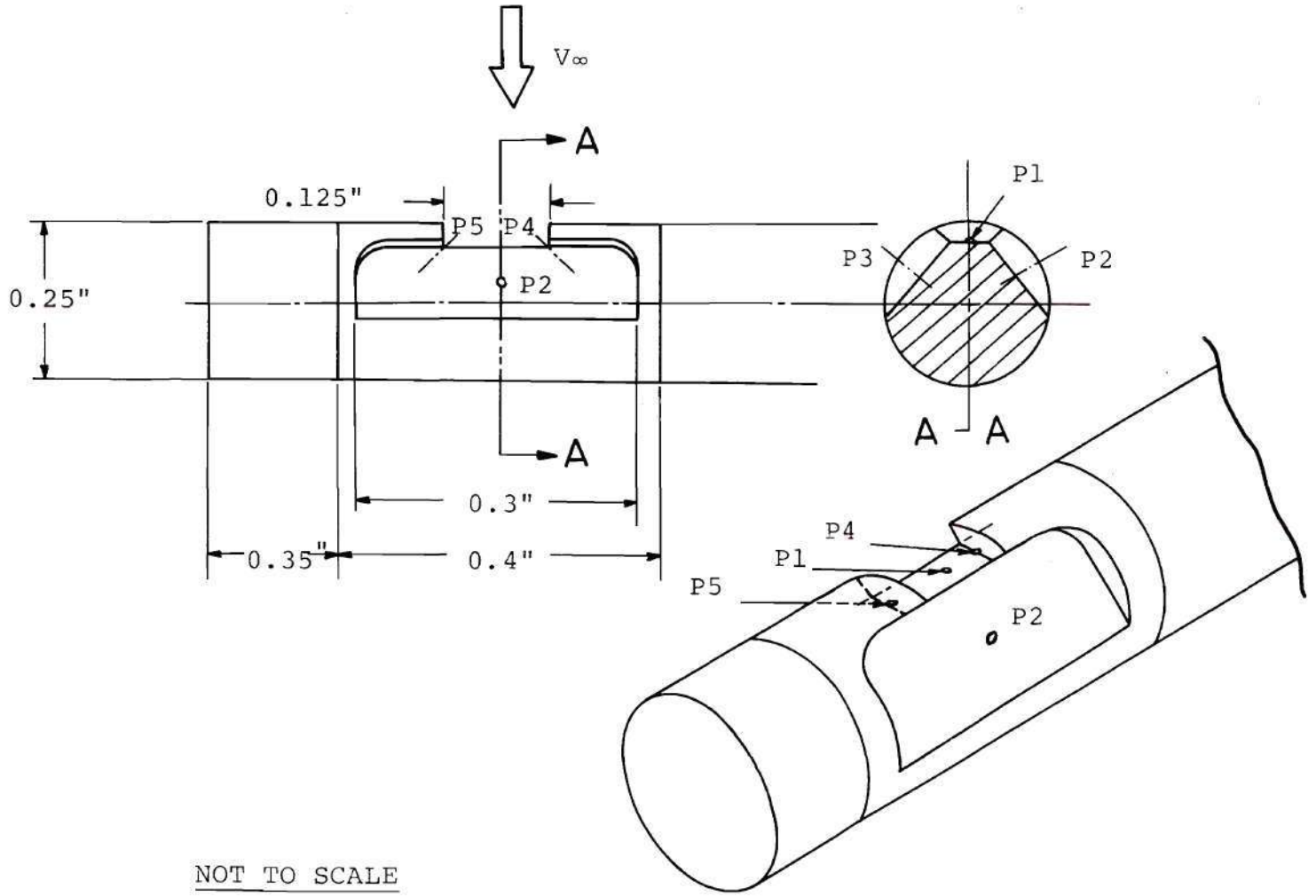

Figure 8. 5-Hole Pressure Probe.

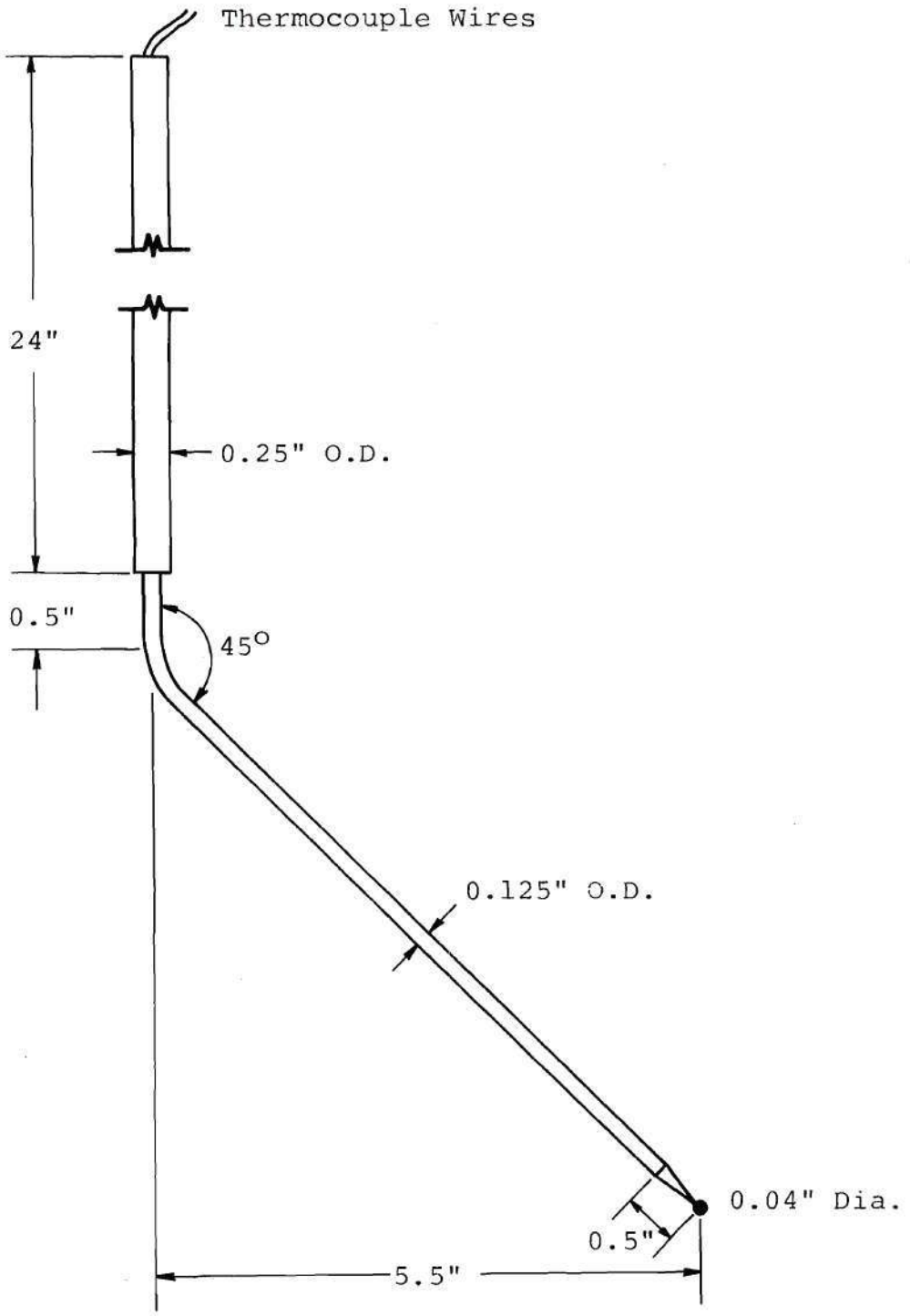

Figure 9. Thermocouple for Measurement of Local Jet Temperature.

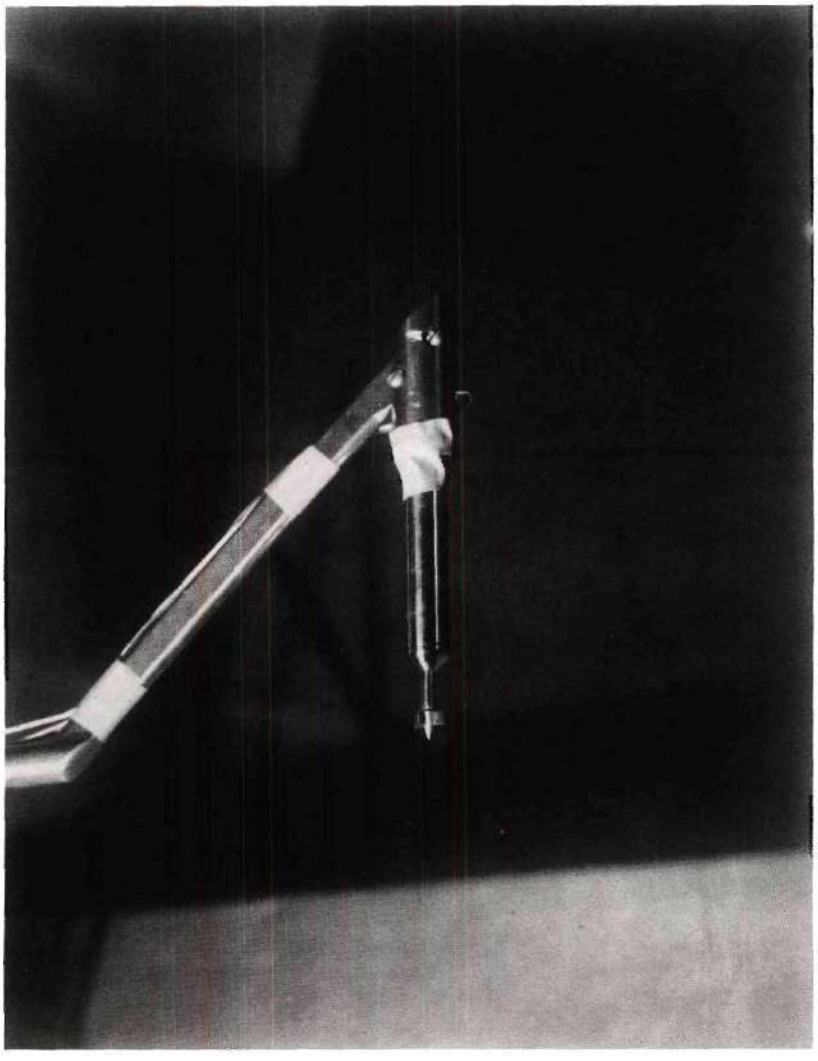

Figure 10. Vortex Meter and Support.

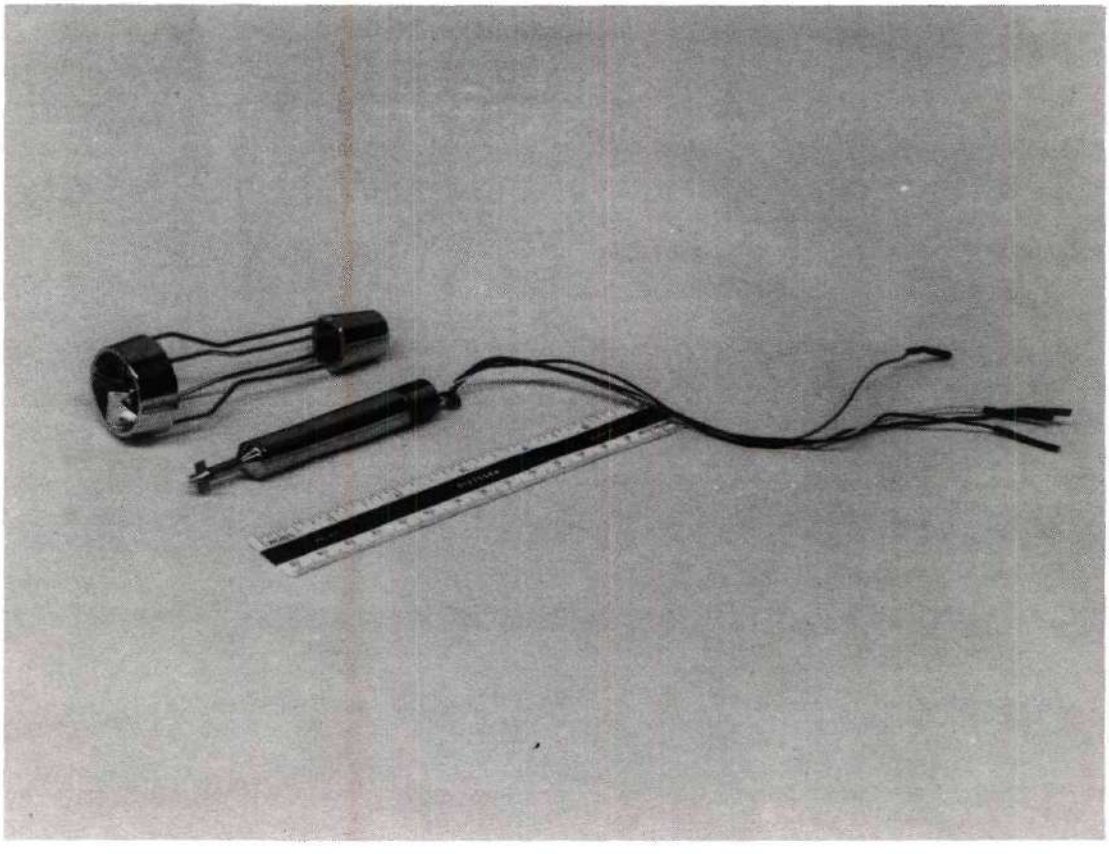

Figure 11. Vortex Meter and Calibrating Device.

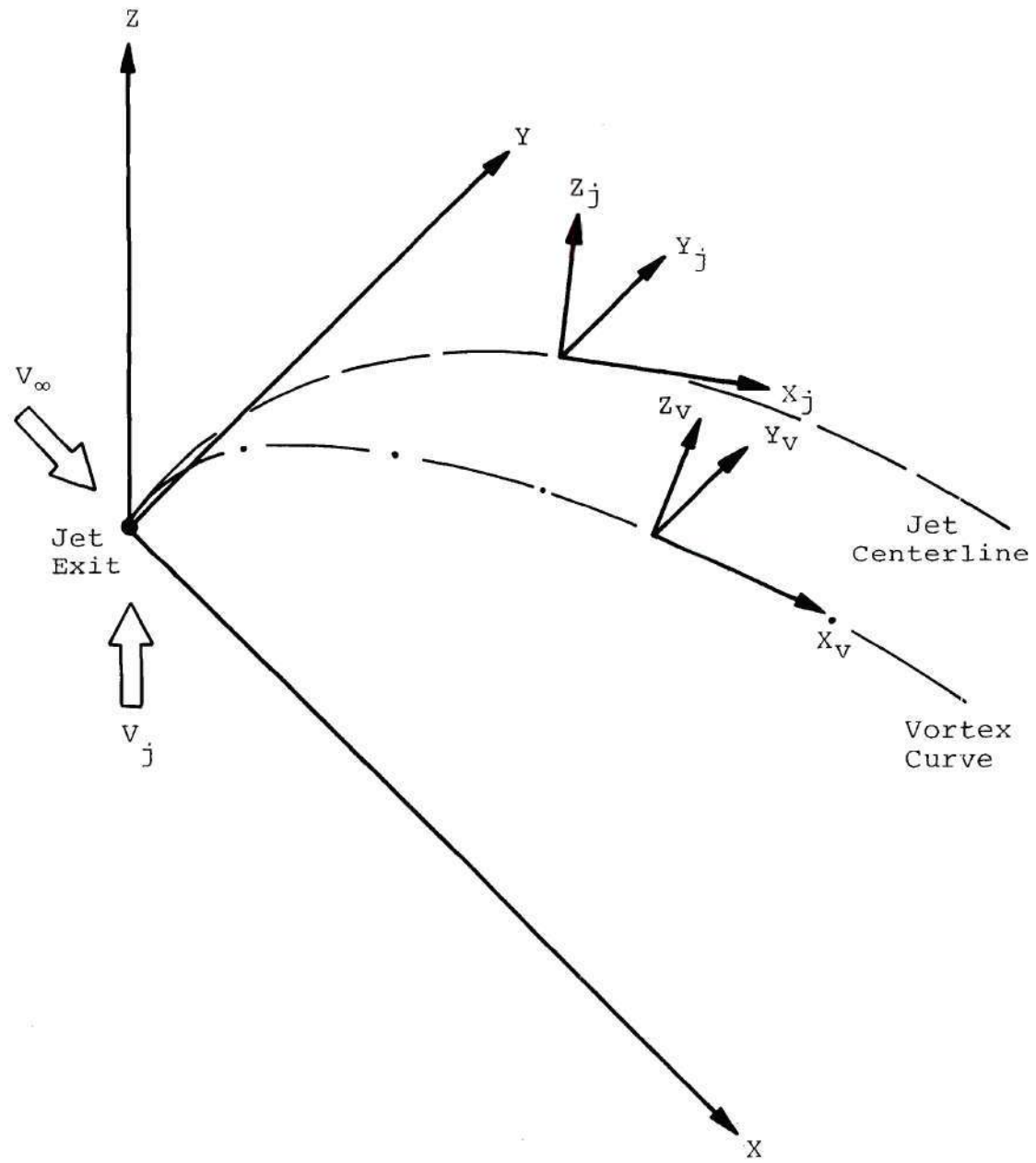

Figure 12. Coordinate Systems.

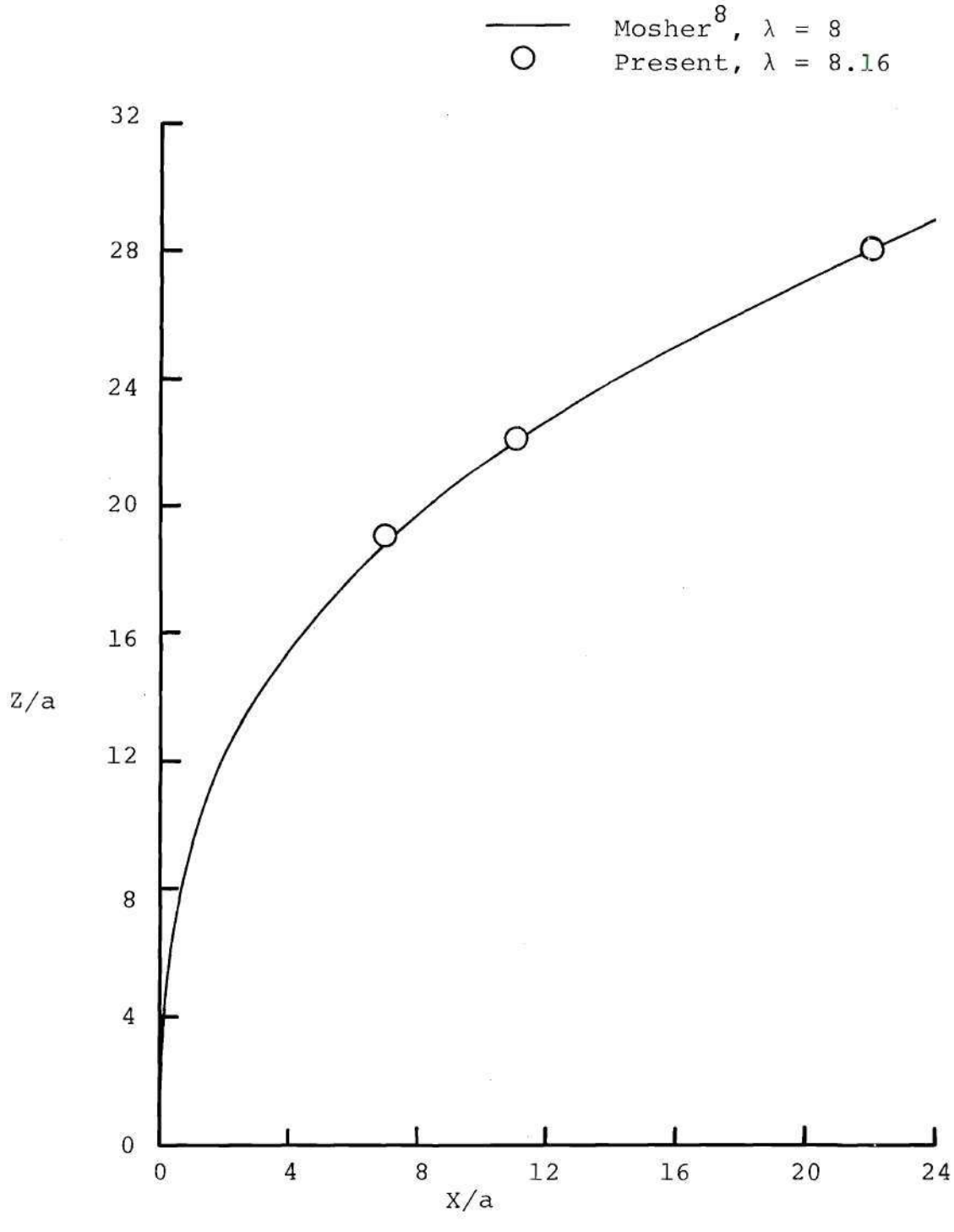

Figure 13. Jet Centerline for Circular Jet.

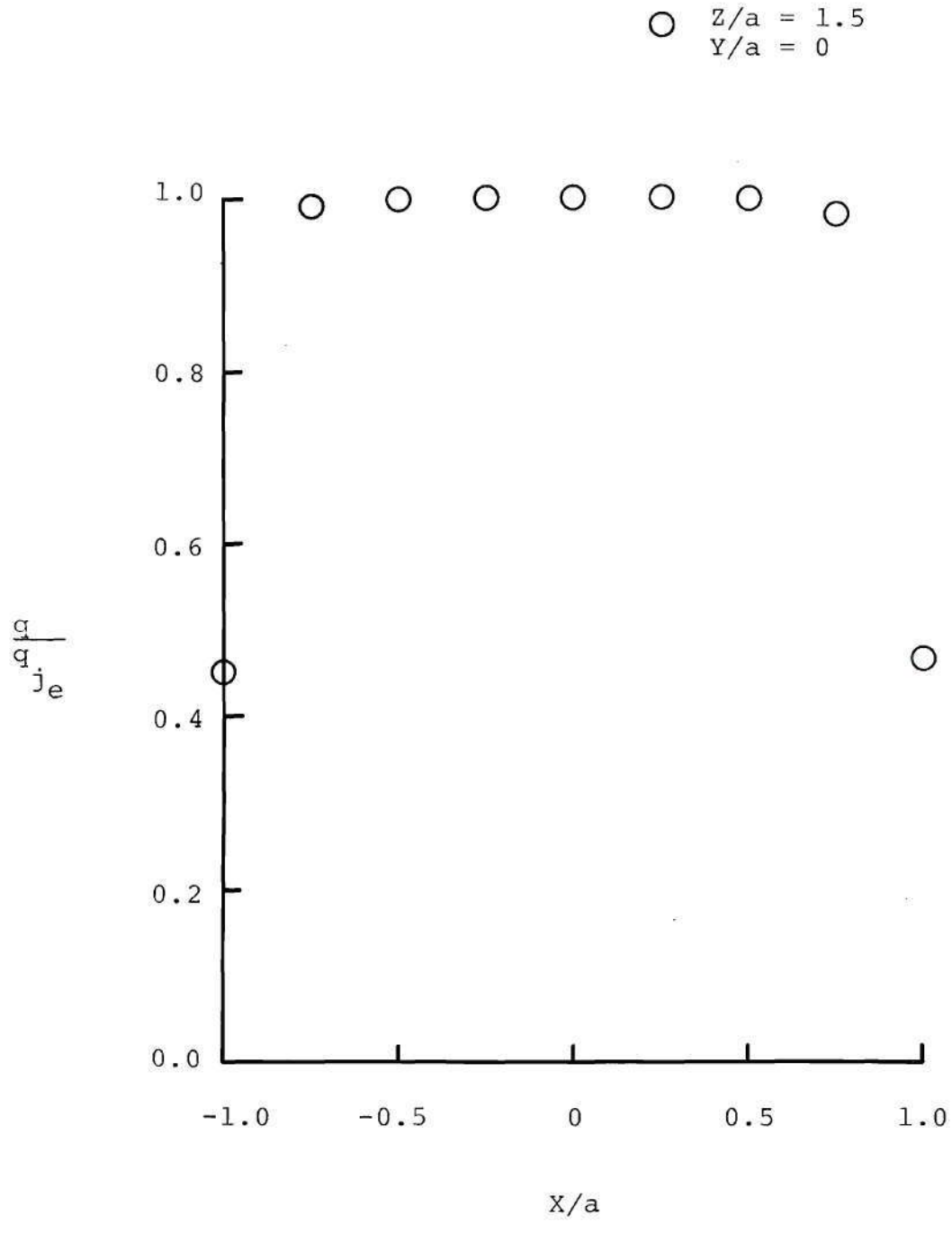

Figure 14. Representative Jet Dynamic Pressure Profile, Circular Jet ($V_\infty = 0$).

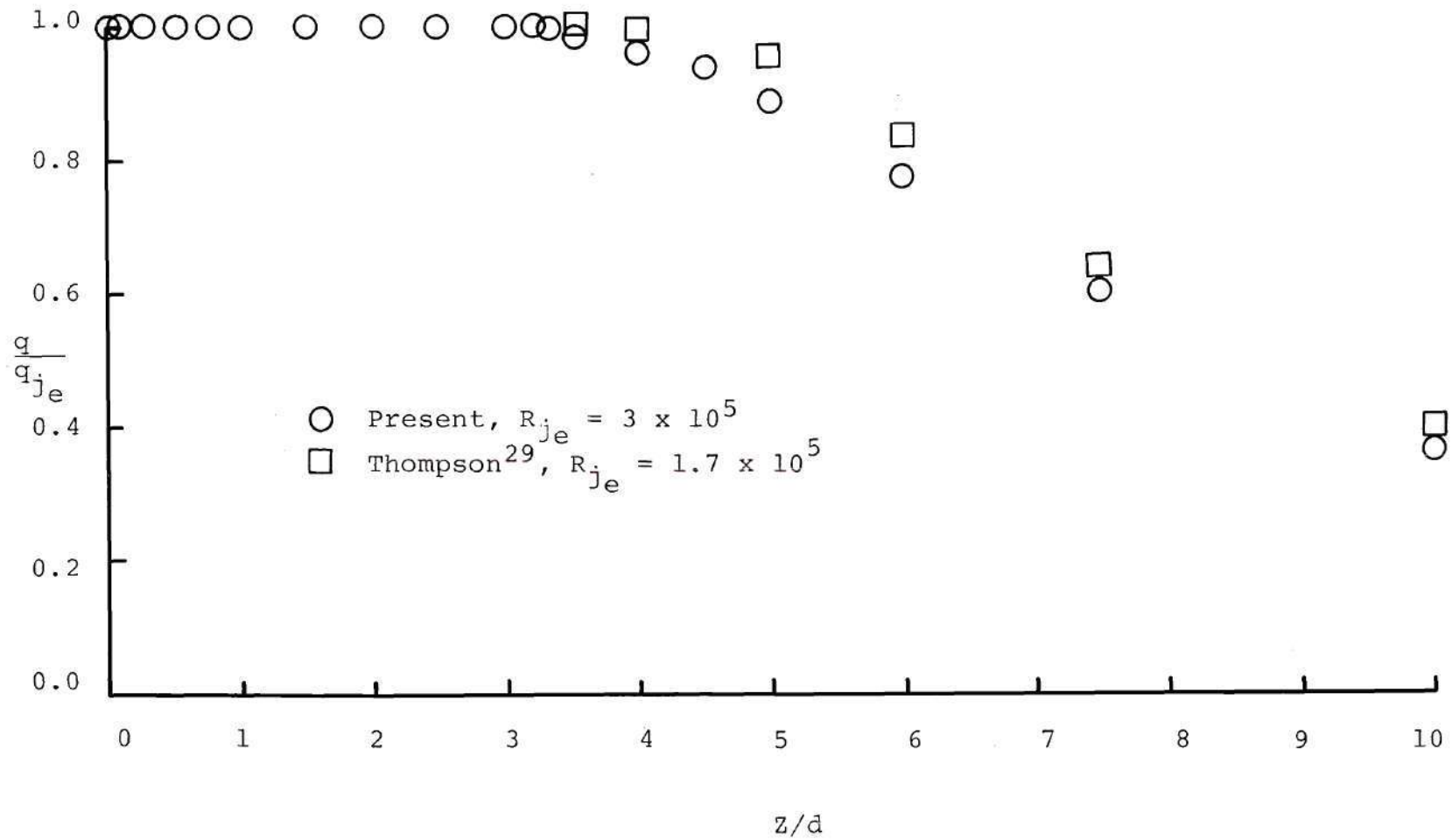

Figure 15. Free-Jet Decay Characteristic, Circular Jet, X/d = 0, Y/d = 0.

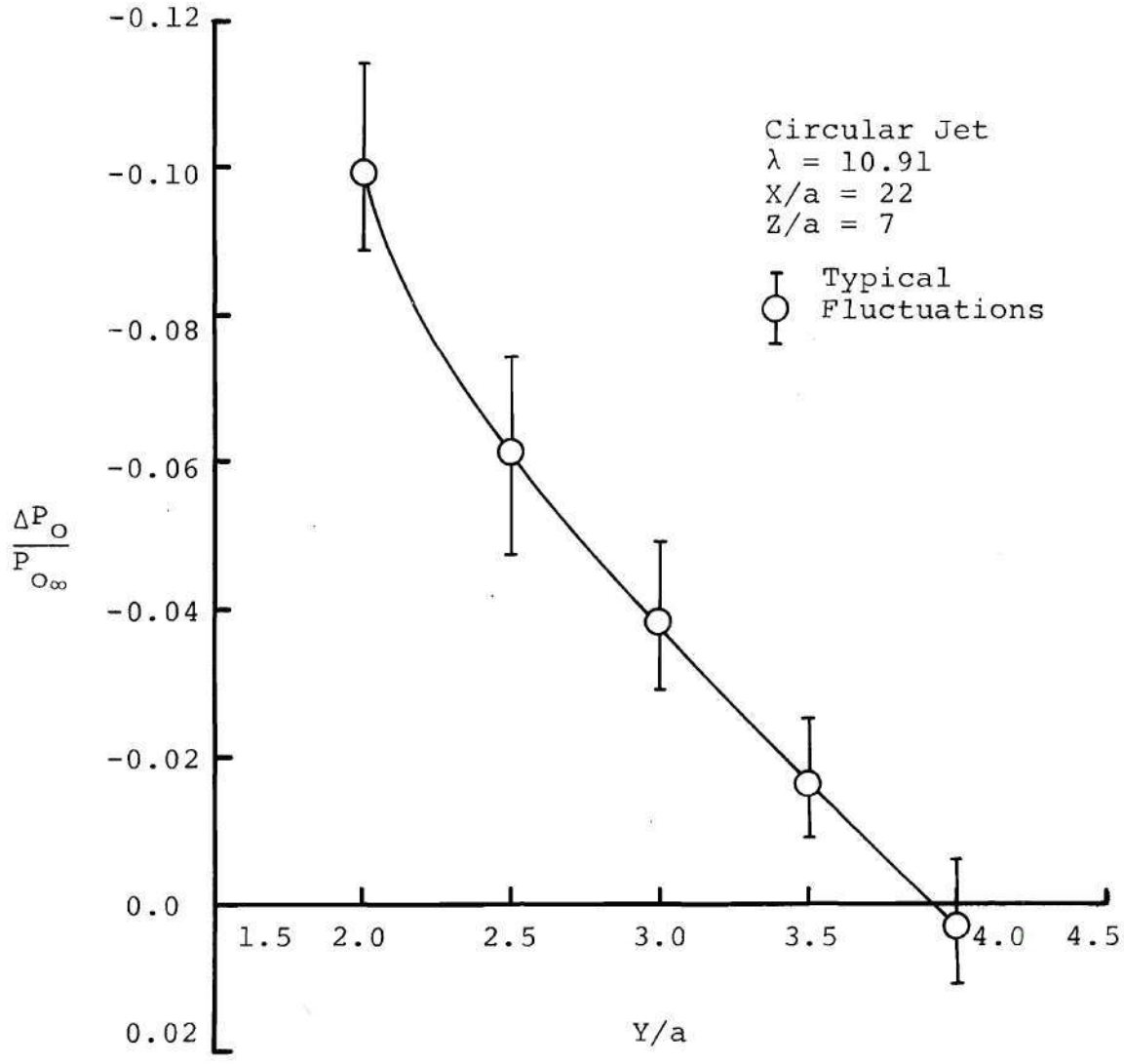

Figure 16. Typical Fluctuations in Kiel Probe Data.

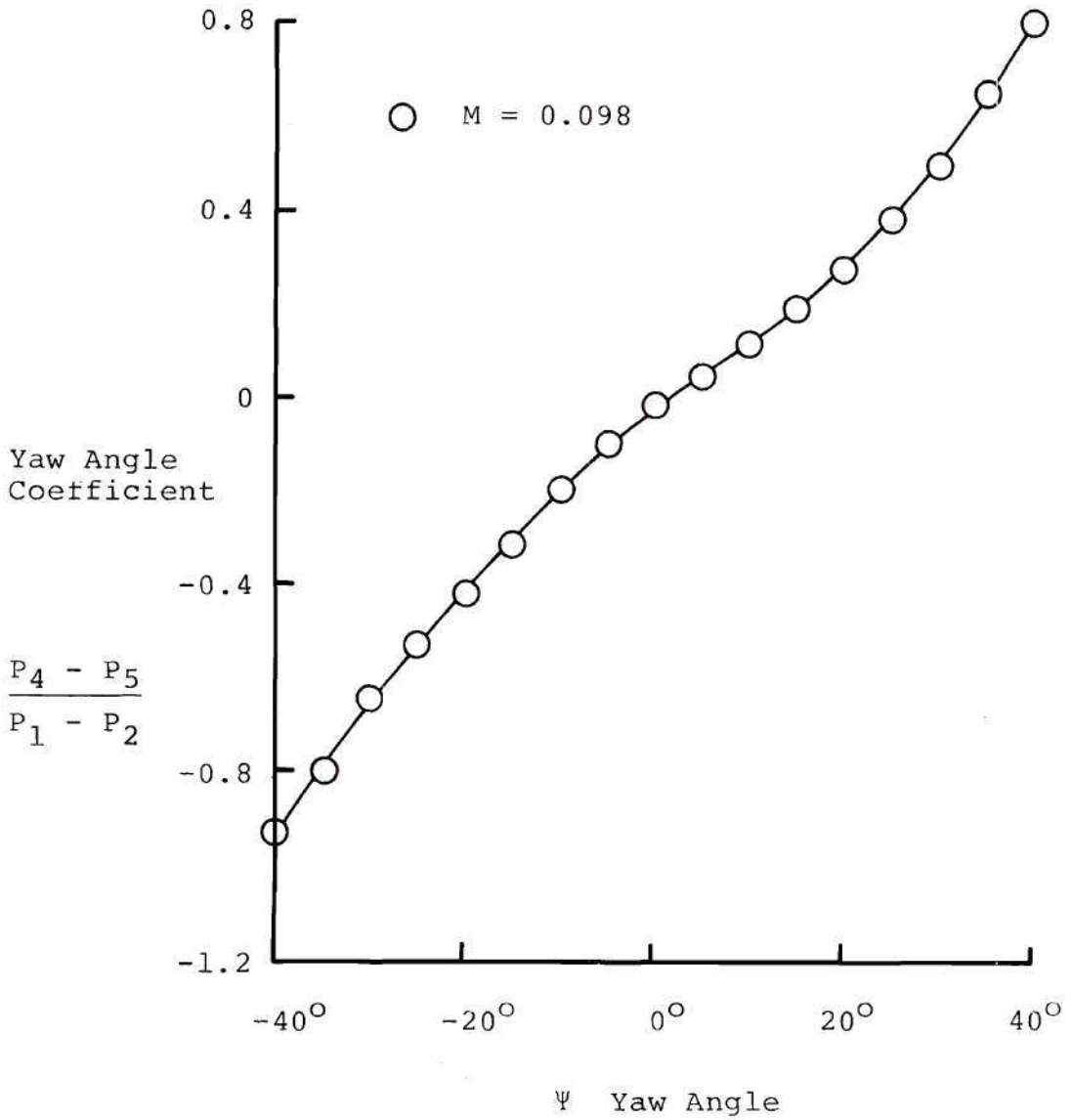

(a) Yaw Angle versus Yaw Angle Coefficient

Figure 17. 5-Hole Pressure Probe Calibration Curves.

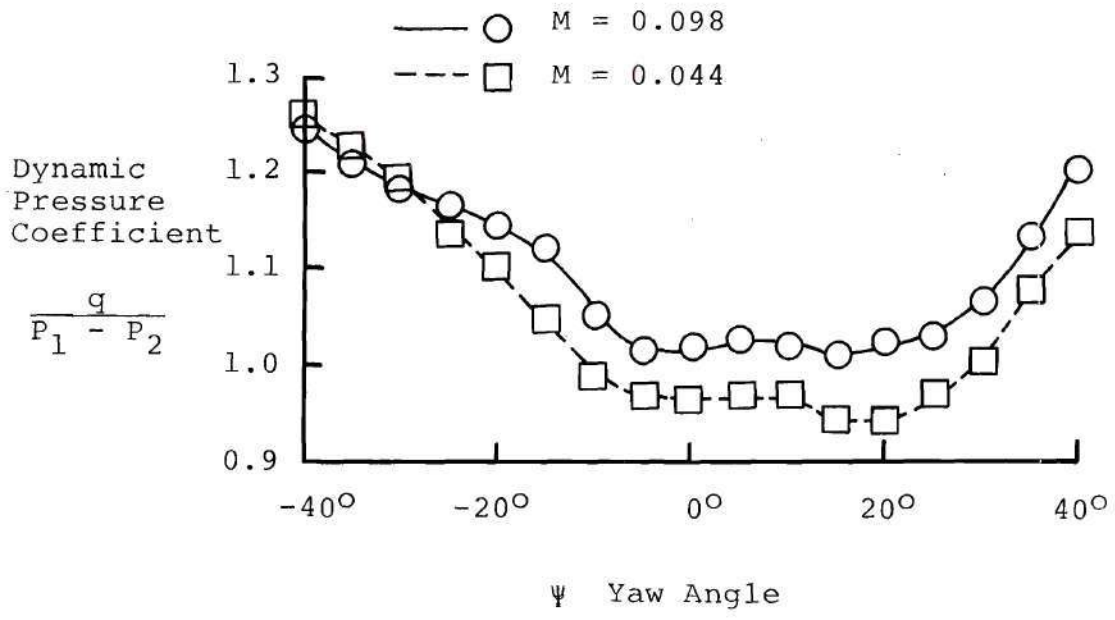

(b) Yaw Angle versus Dynamic Pressure Coefficient

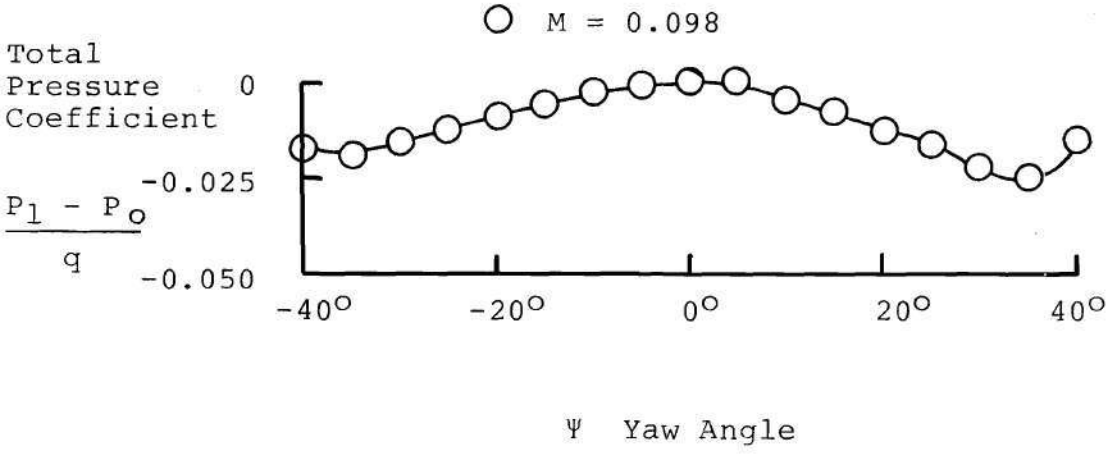

(c) Yaw Angle versus Total Pressure Coefficient

Figure 17. 5-Hole Pressure Probe Calibration Curves (Concluded).

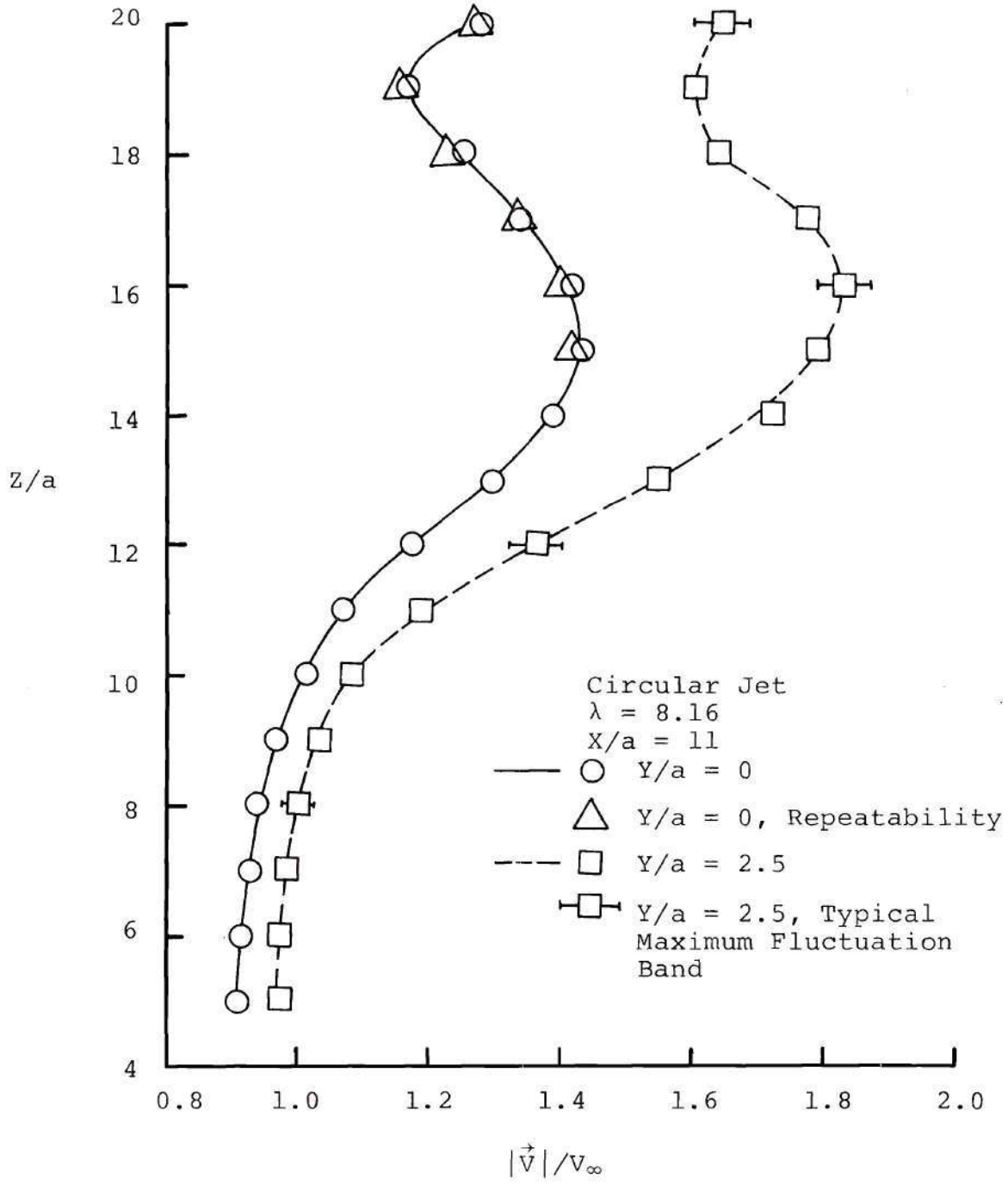

Figure 18. Typical Fluctuations and Repeatability in 5-Hole Pressure Probe Velocity Measurements.

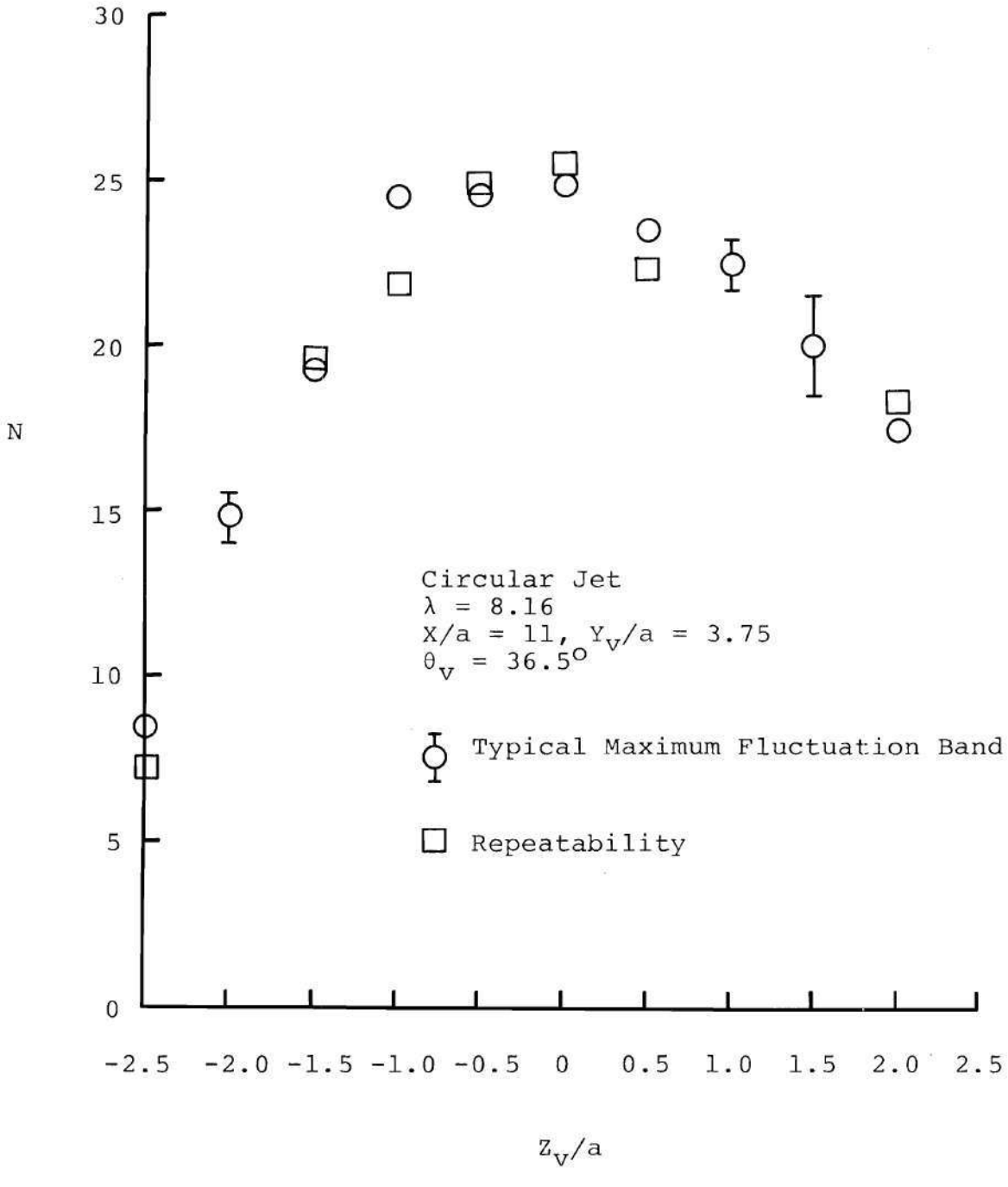

Figure 19. Typical Fluctuations and Repeatability in Vortex Meter Measurements, Units of N (CPS).

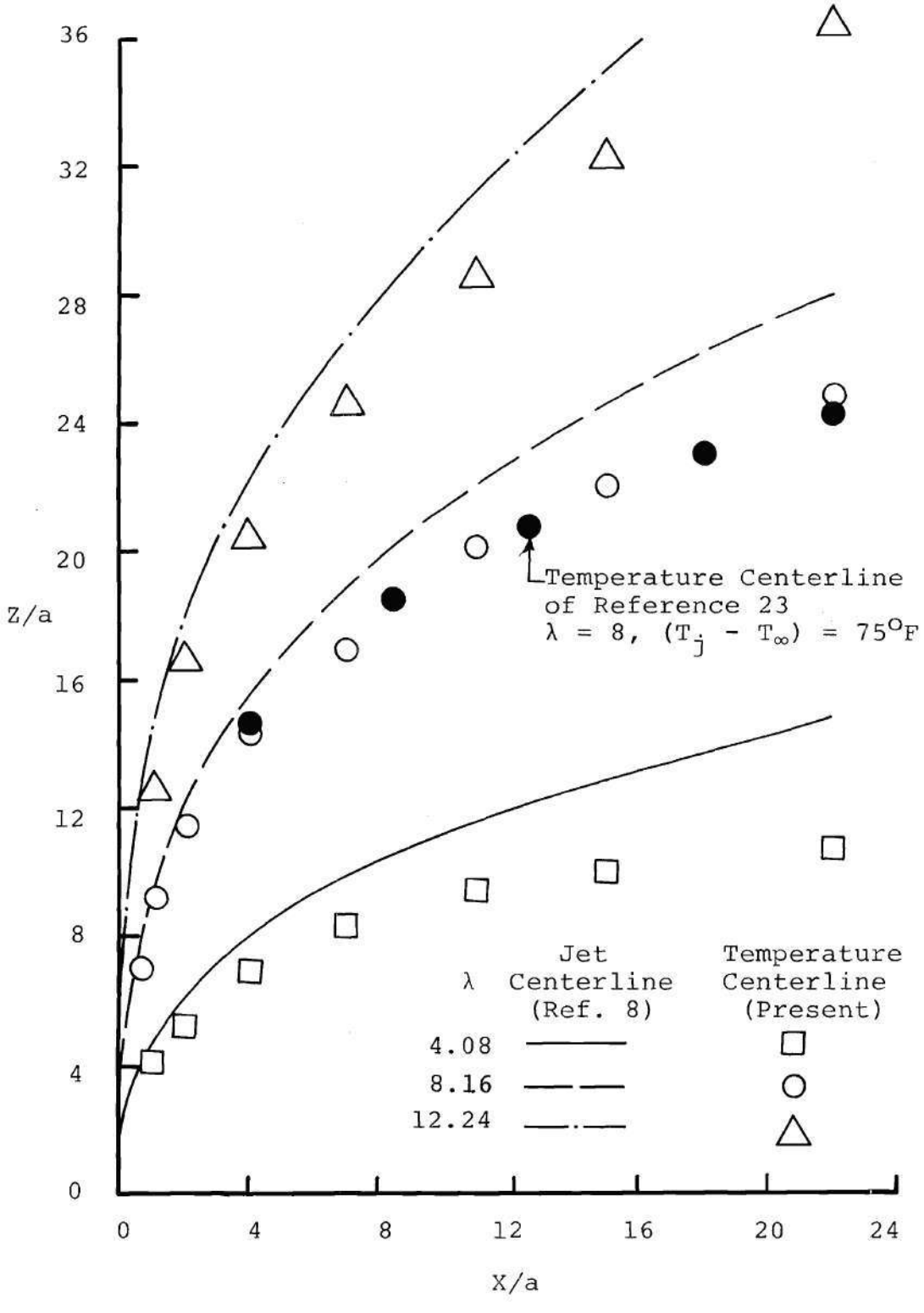

Figure 20. Jet Centerlines versus Temperature Centerlines.

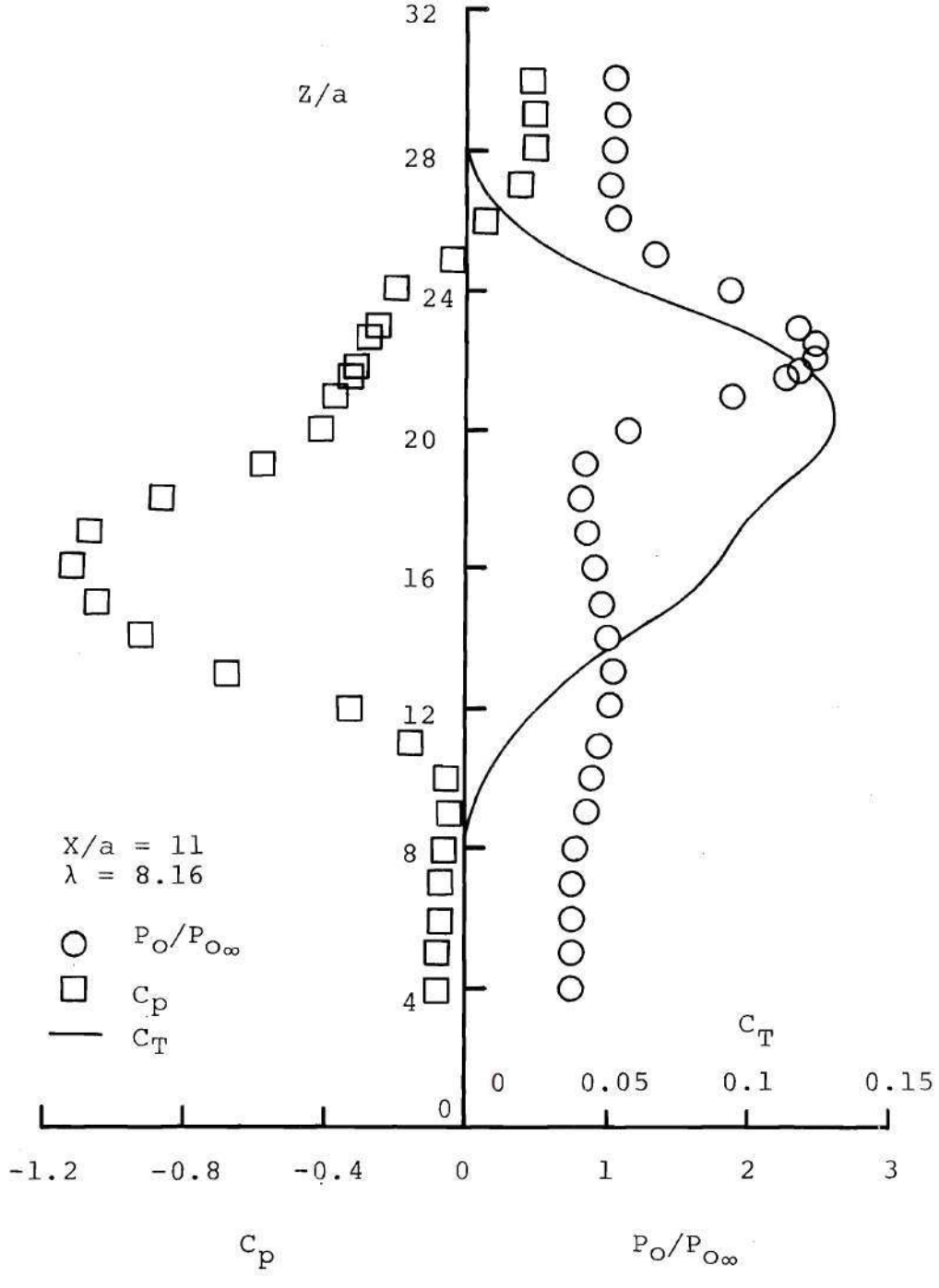

Figure 21. Typical Distributions of Pressure and Temperature in the Plane of Symmetry (Y/a = 0).

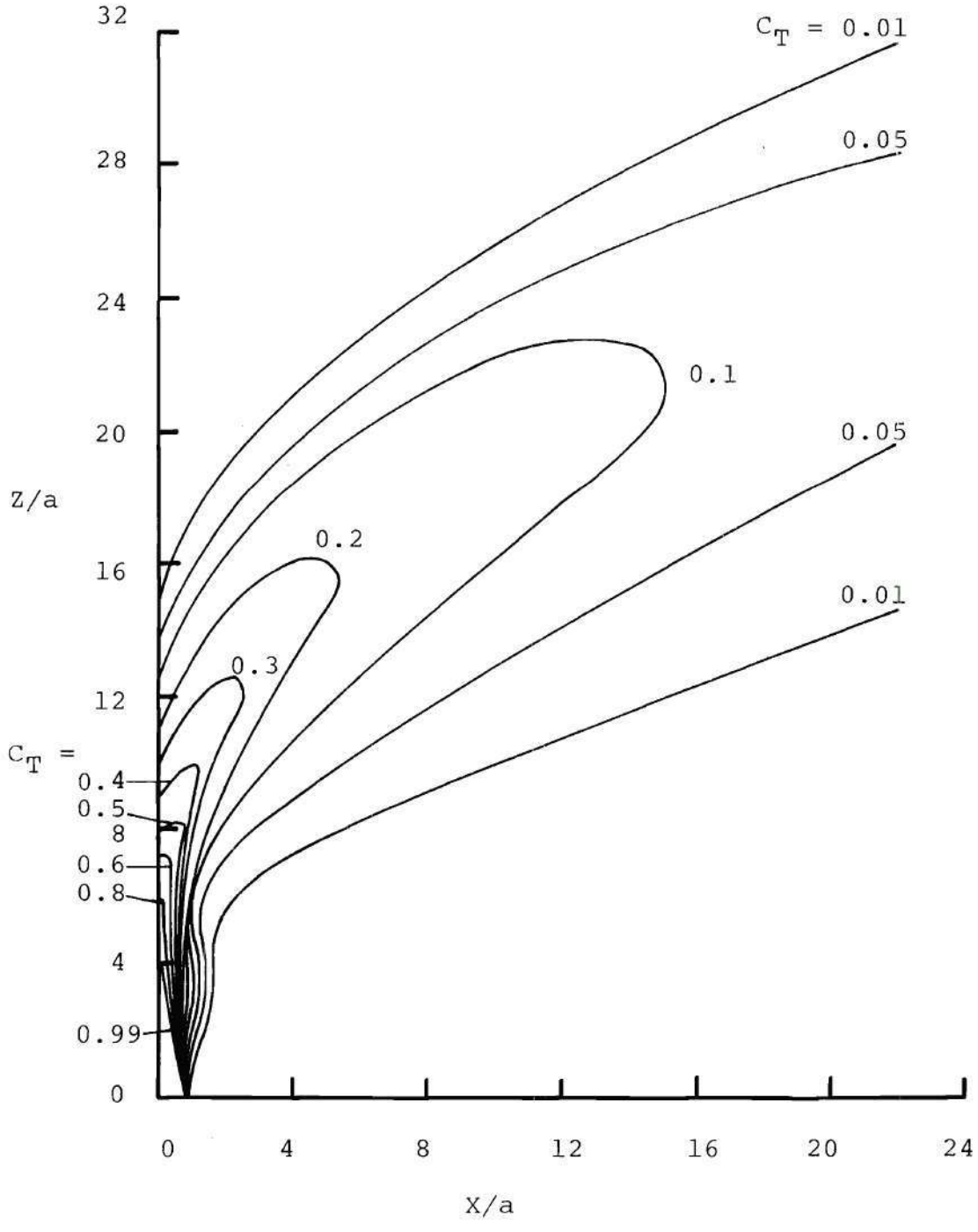

Figure 22. Jet Cross Section in X-Z Plane - C_T Contours, Y/a = 0, λ = 8.16.

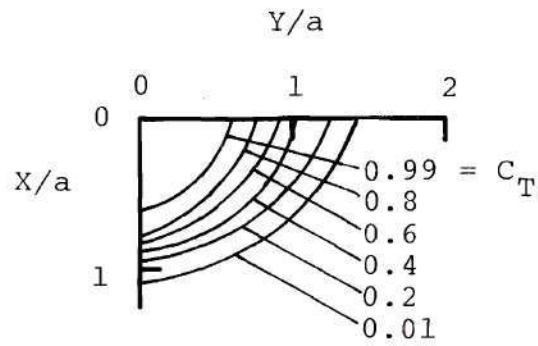

(a) Z/d = 0.5

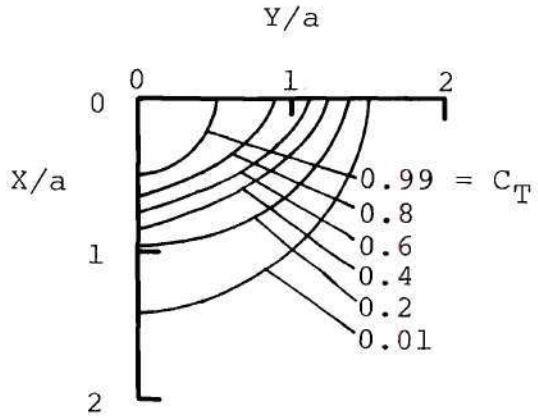

(b) Z/d = 1.0

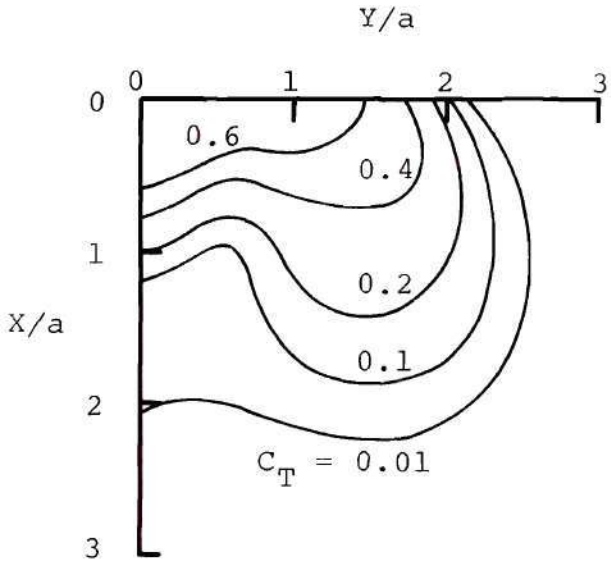

(c) Z/d = 2.0

Figure 23. Jet Cross Section in X-Y Plane - C_T Contours, λ = 8.16.

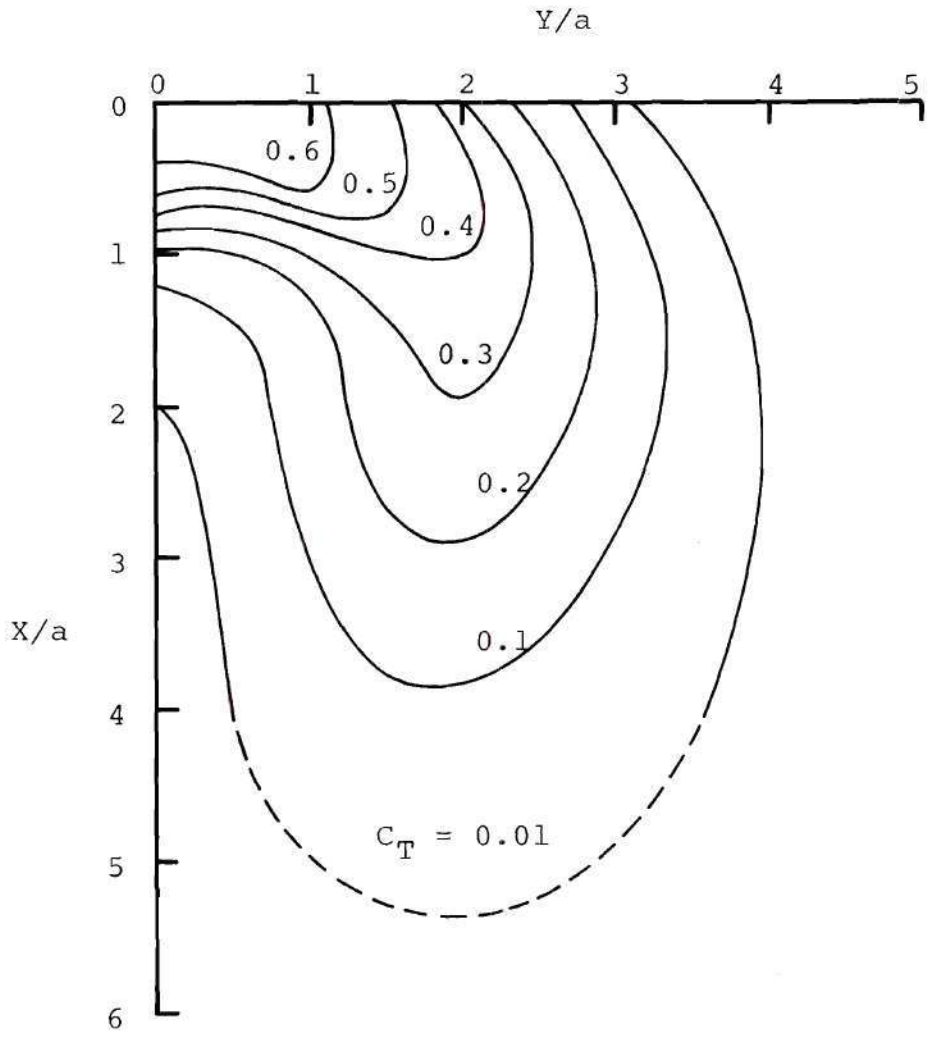

(d) Z/d = 3.0

Figure 23. Jet Cross Section in X-Y Plane - C_T Contours, λ = 8.16 (Continued).

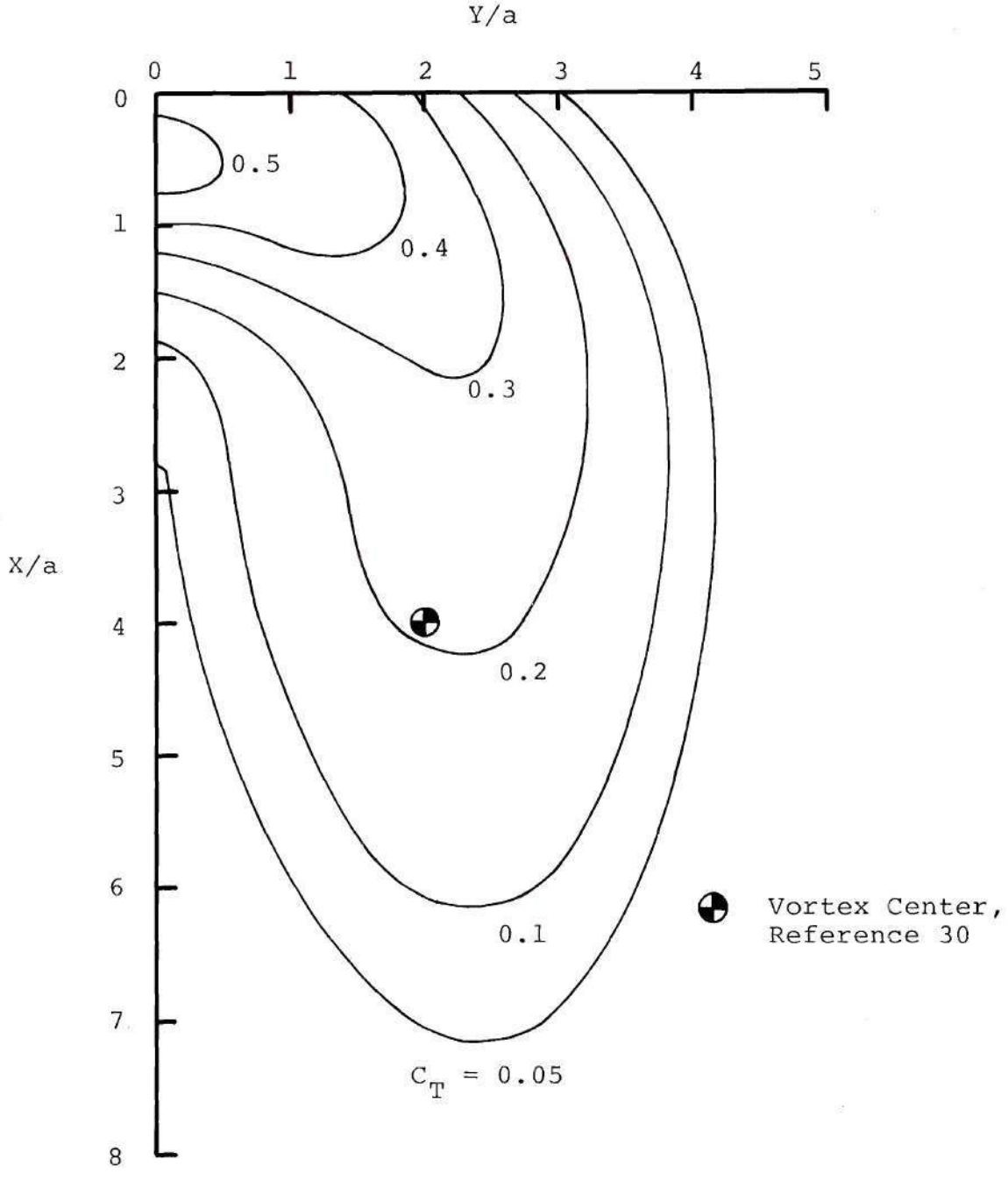

(e) Z/d = 4.0

Figure 23. Jet Cross Section in X-Y Plane - C_T Contours, λ = 8.16 (Concluded).

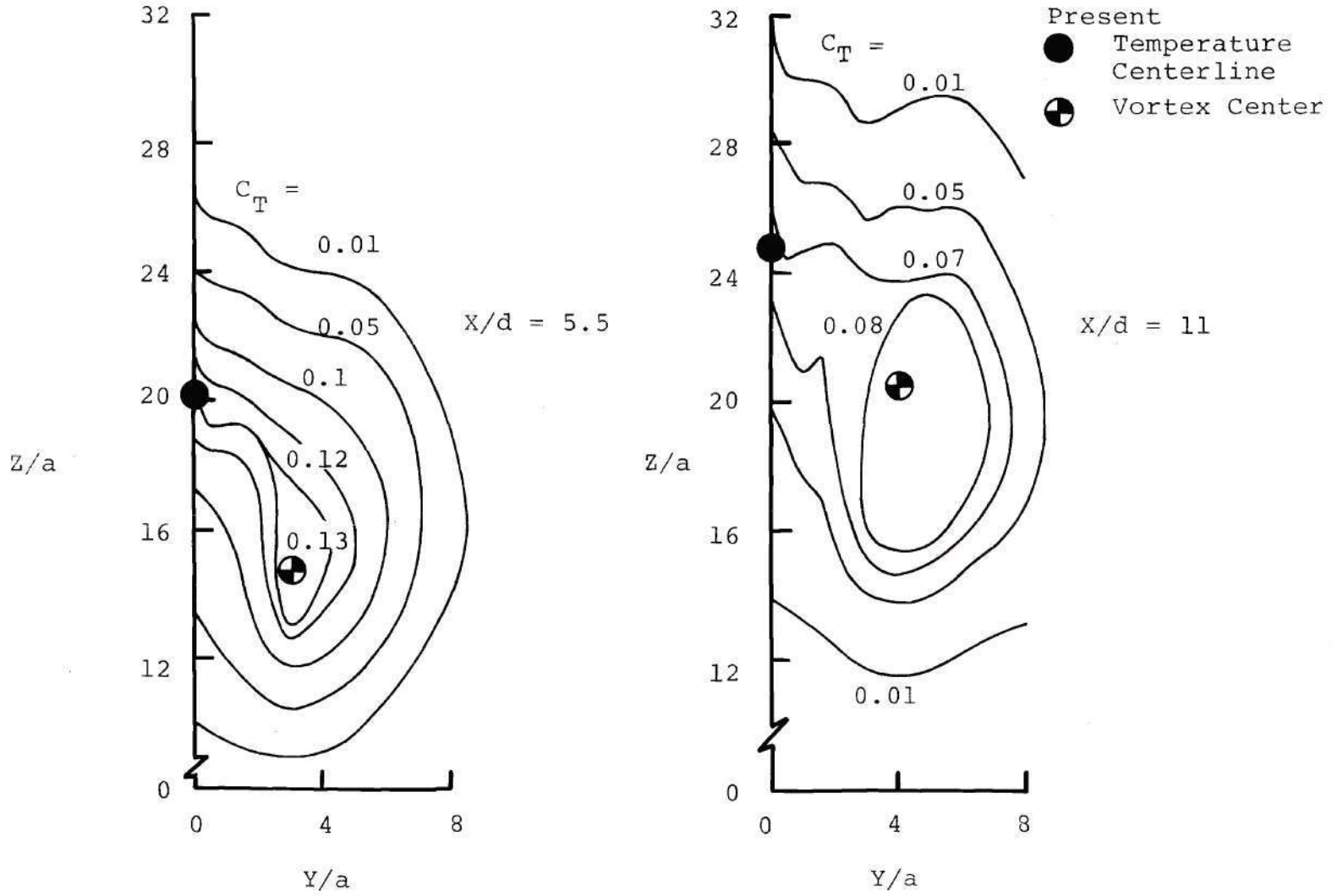

Figure 24. Jet Cross Section in Y-Z Plane - C_T Contours, λ = 8.16.

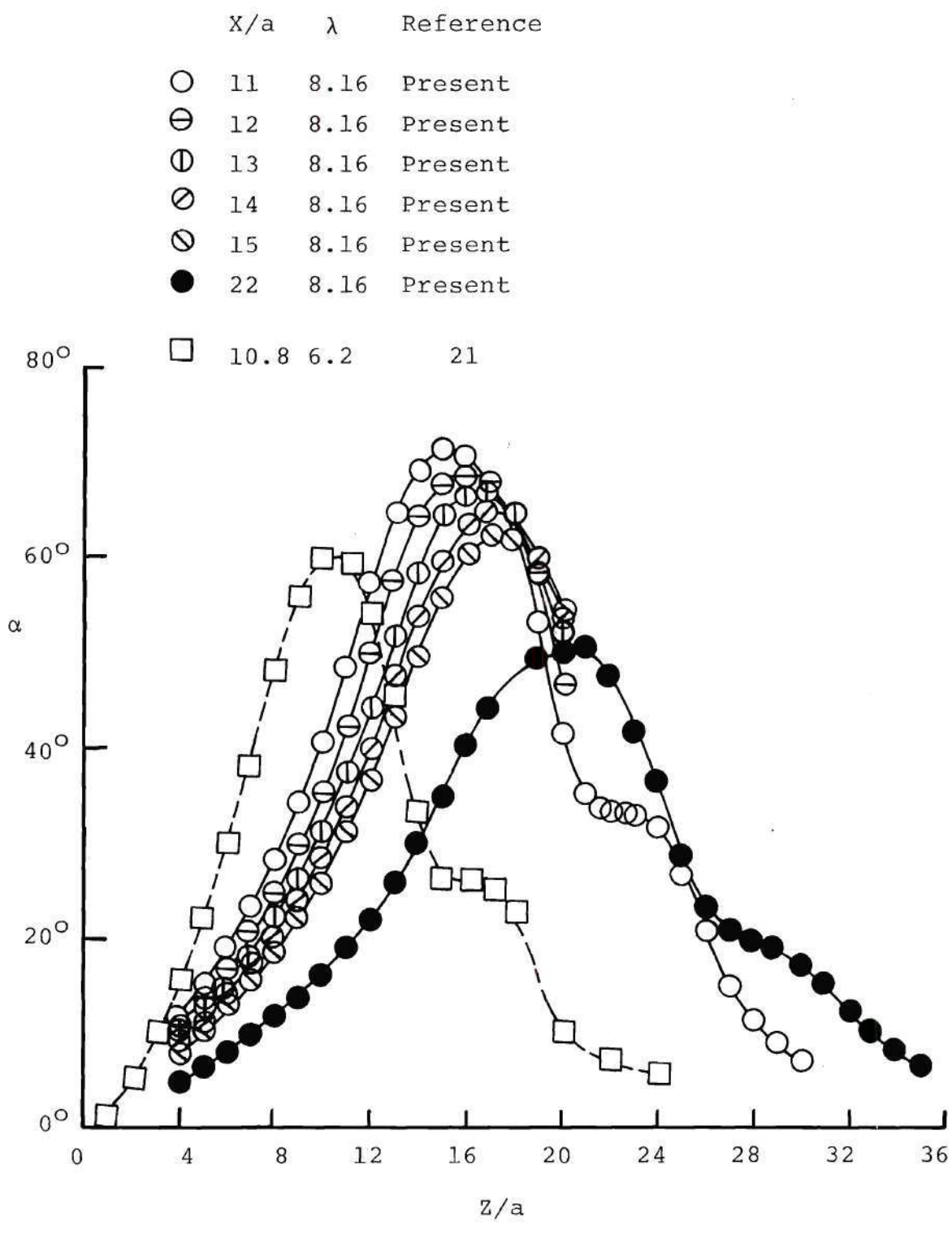

Figure 25. Upwash Angle Distributions for the Plane of Symmetry (Y/a = 0).

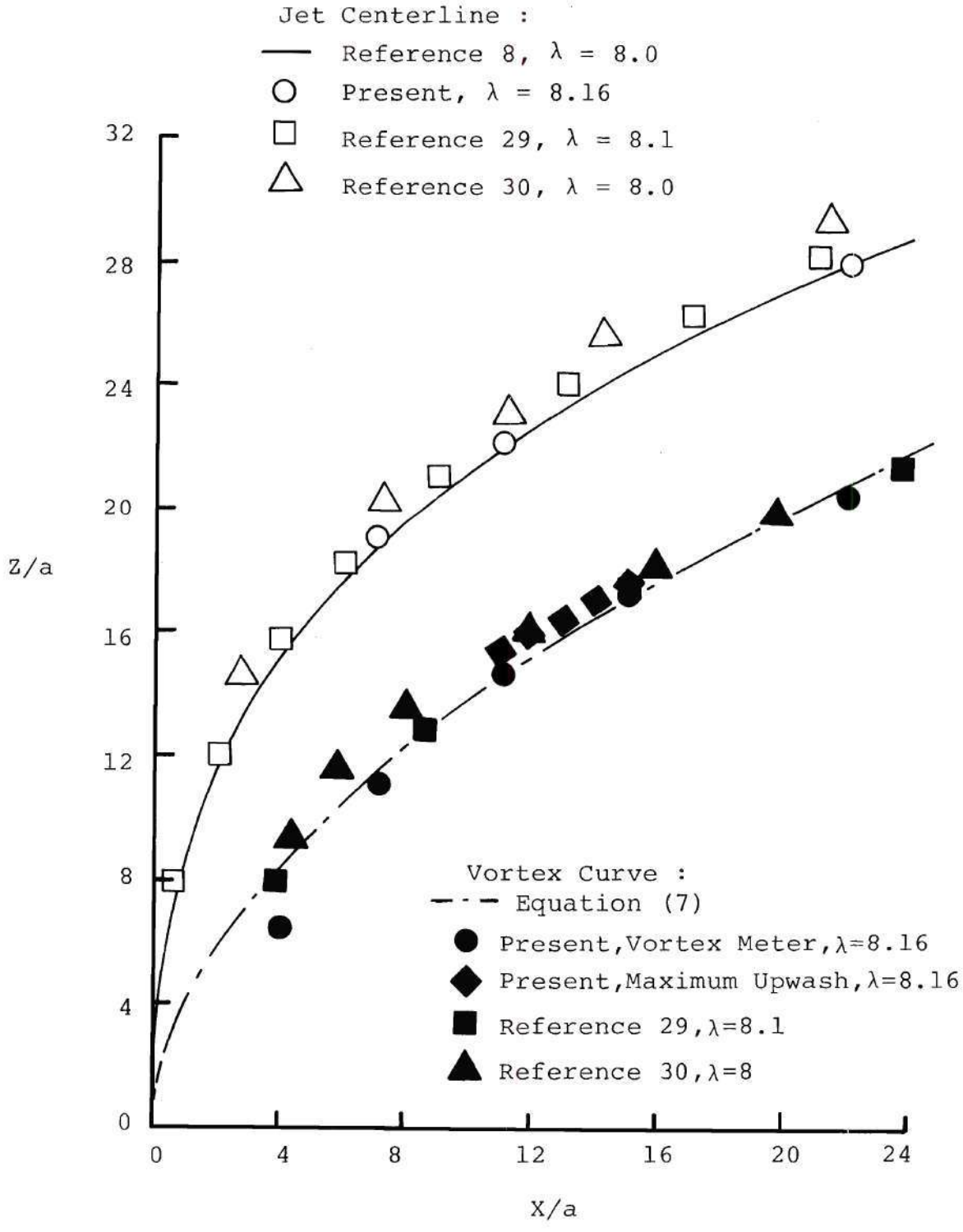

Figure 26. Projection of Vortex Centerline on X-Z Plane (Vortex Curve).

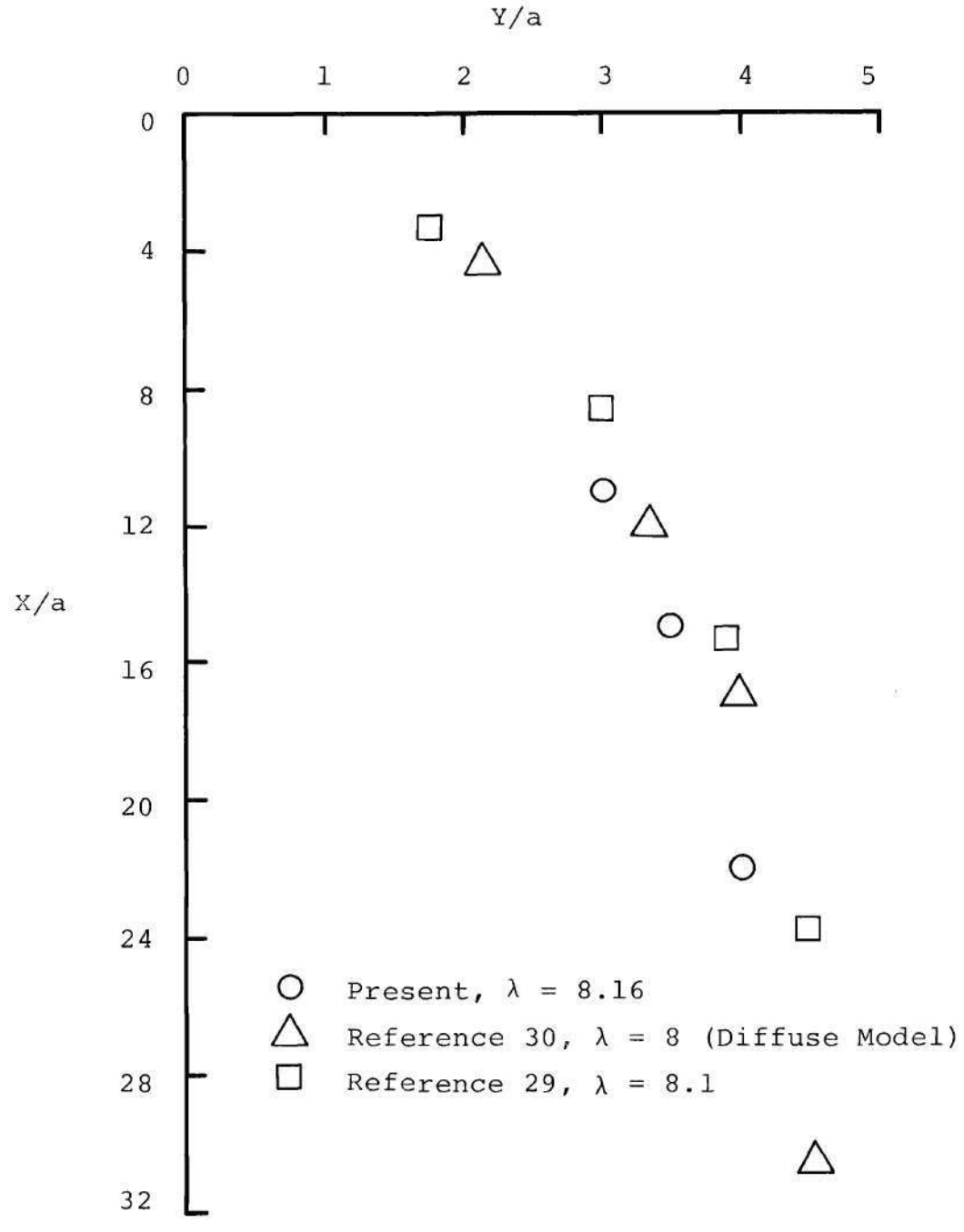

Figure 27. Projection of Vortex Centerline on X-Y Plane (Vortex Spacing).

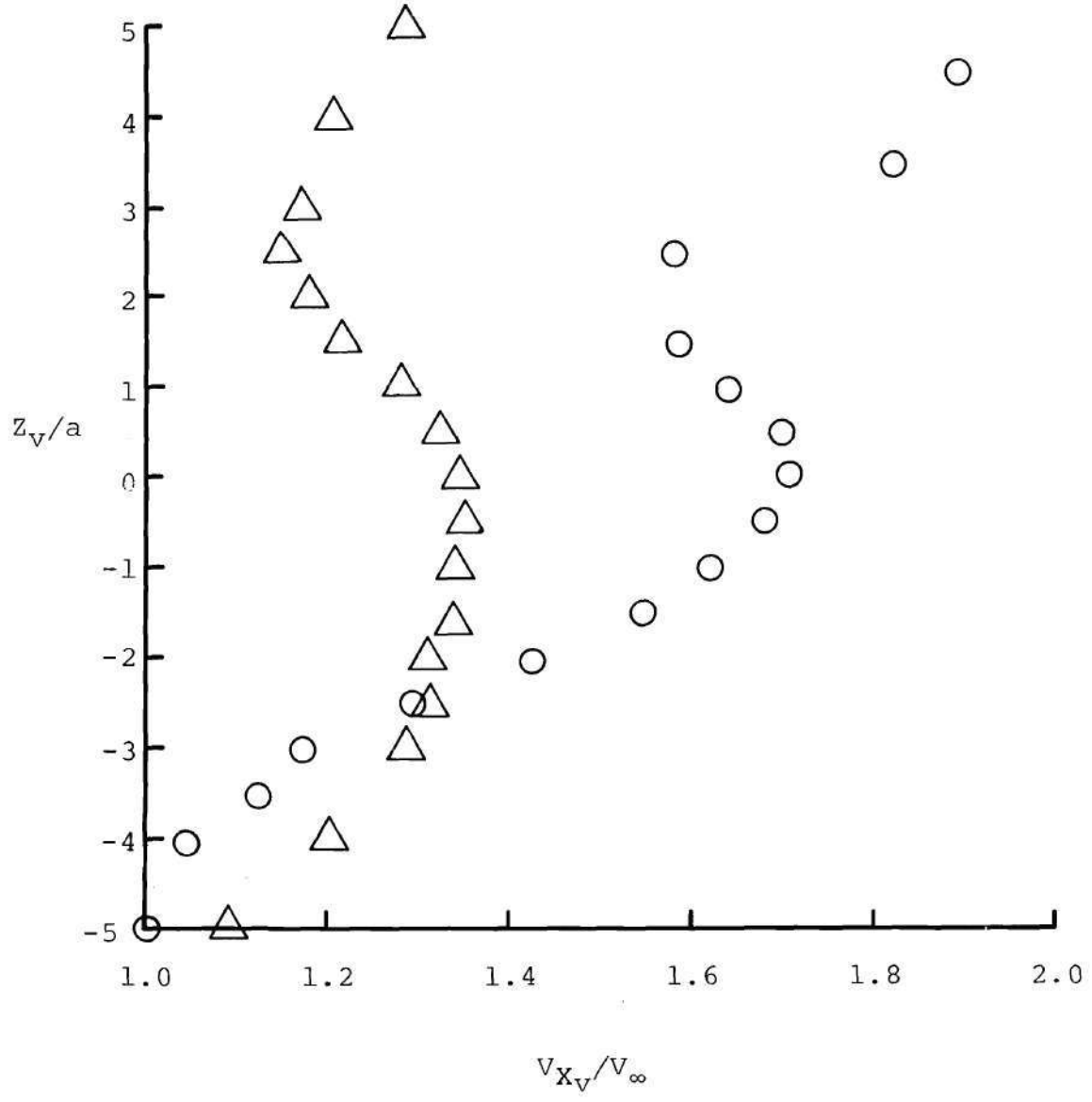

Figure 28. Axial (X_V) Velocity Distributions.

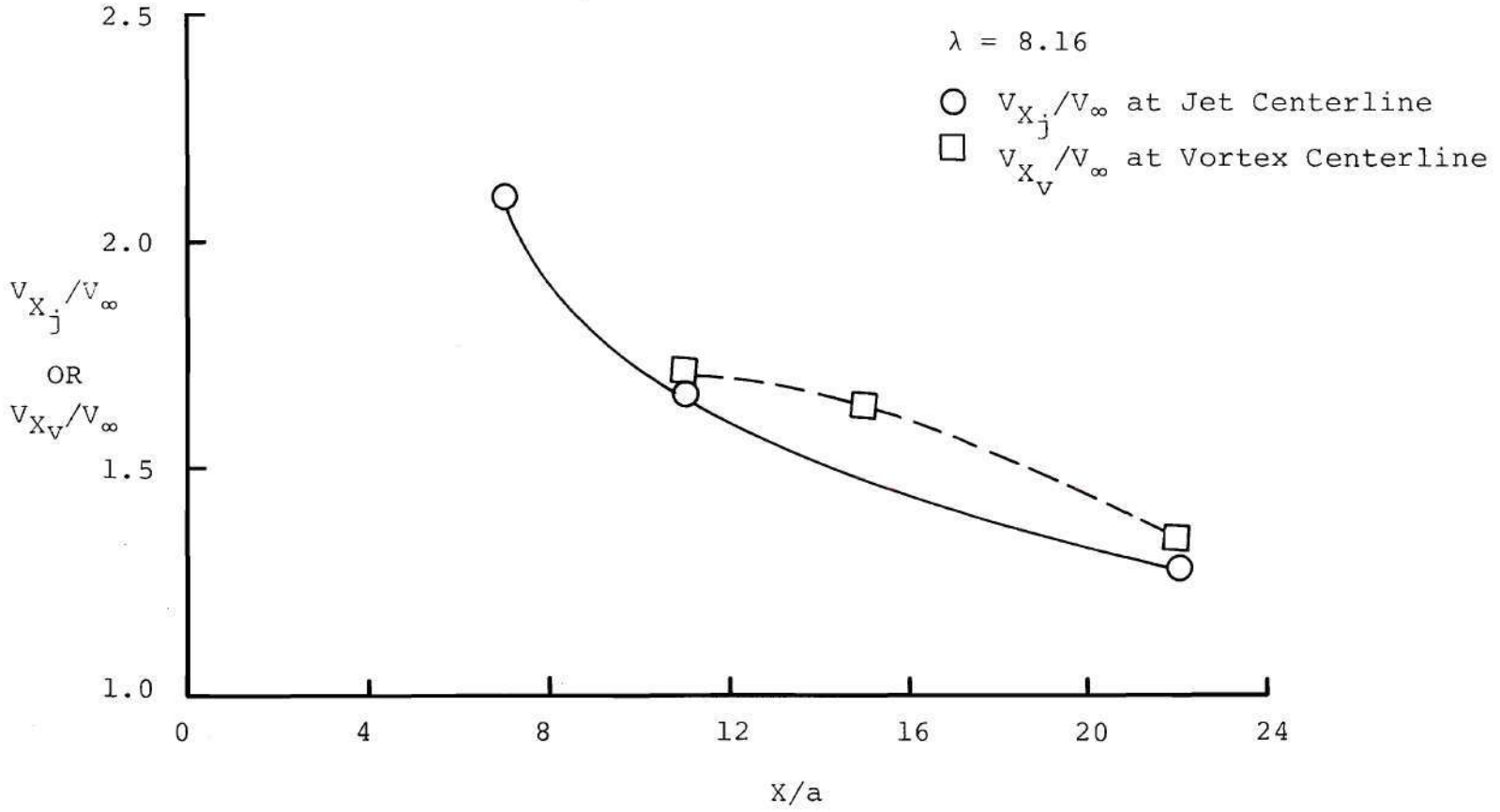

Figure 29. Axial Velocities Along Jet and Vortex Centerlines.

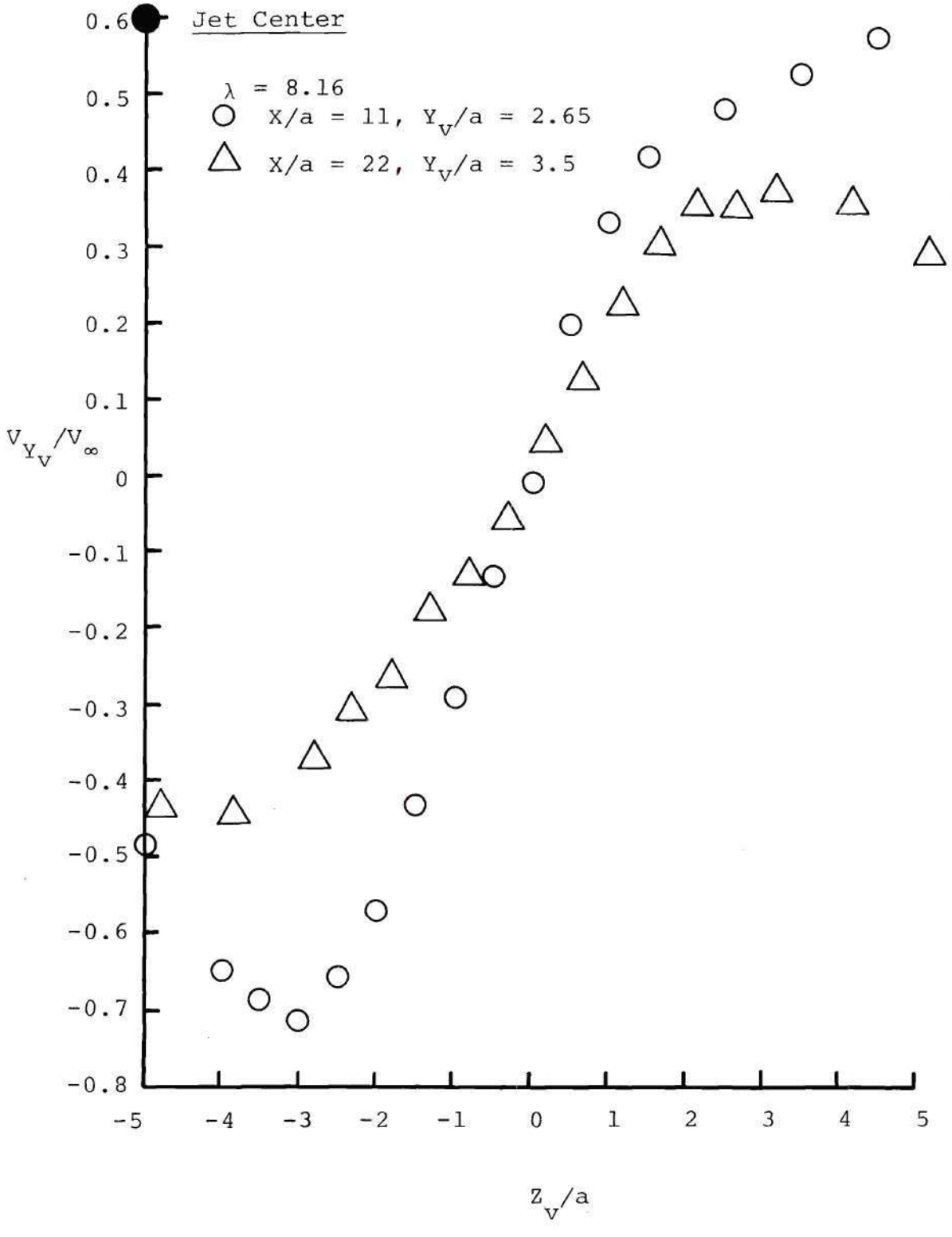

Figure 30. Circumferential Velocity Distributions.

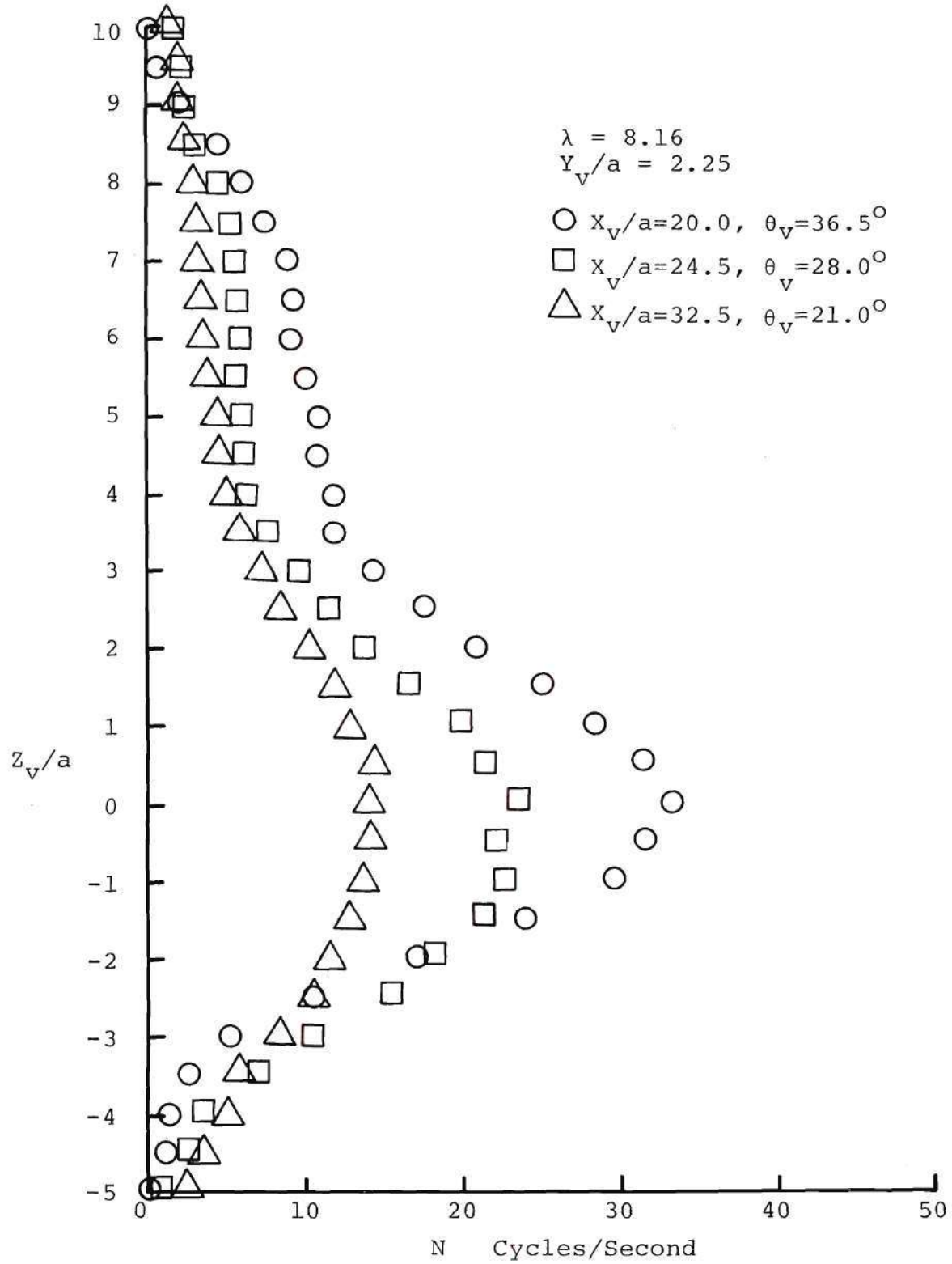

Figure 31. Typical Distributions of N.

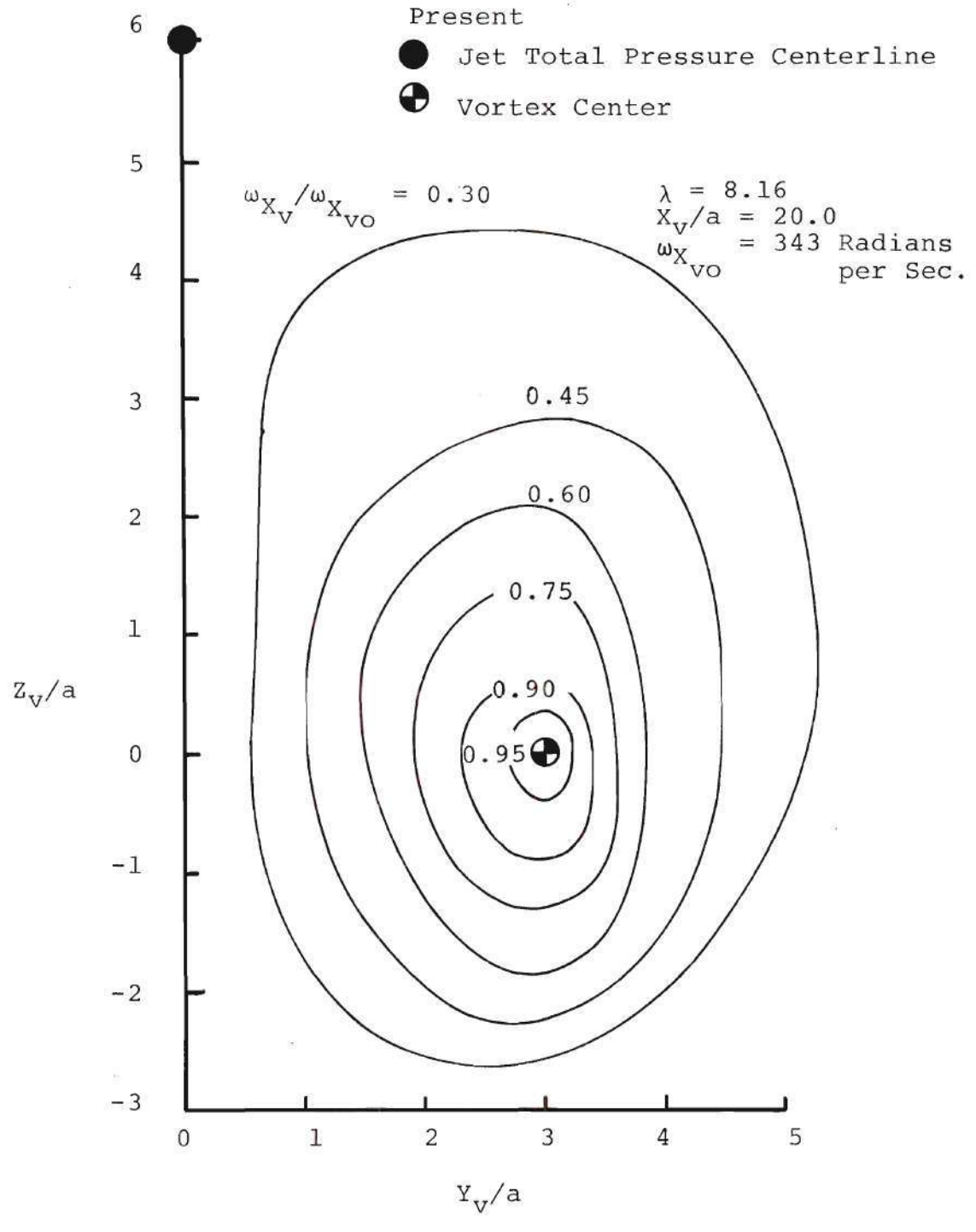

Figure 32. Contours of Constant Vorticity.

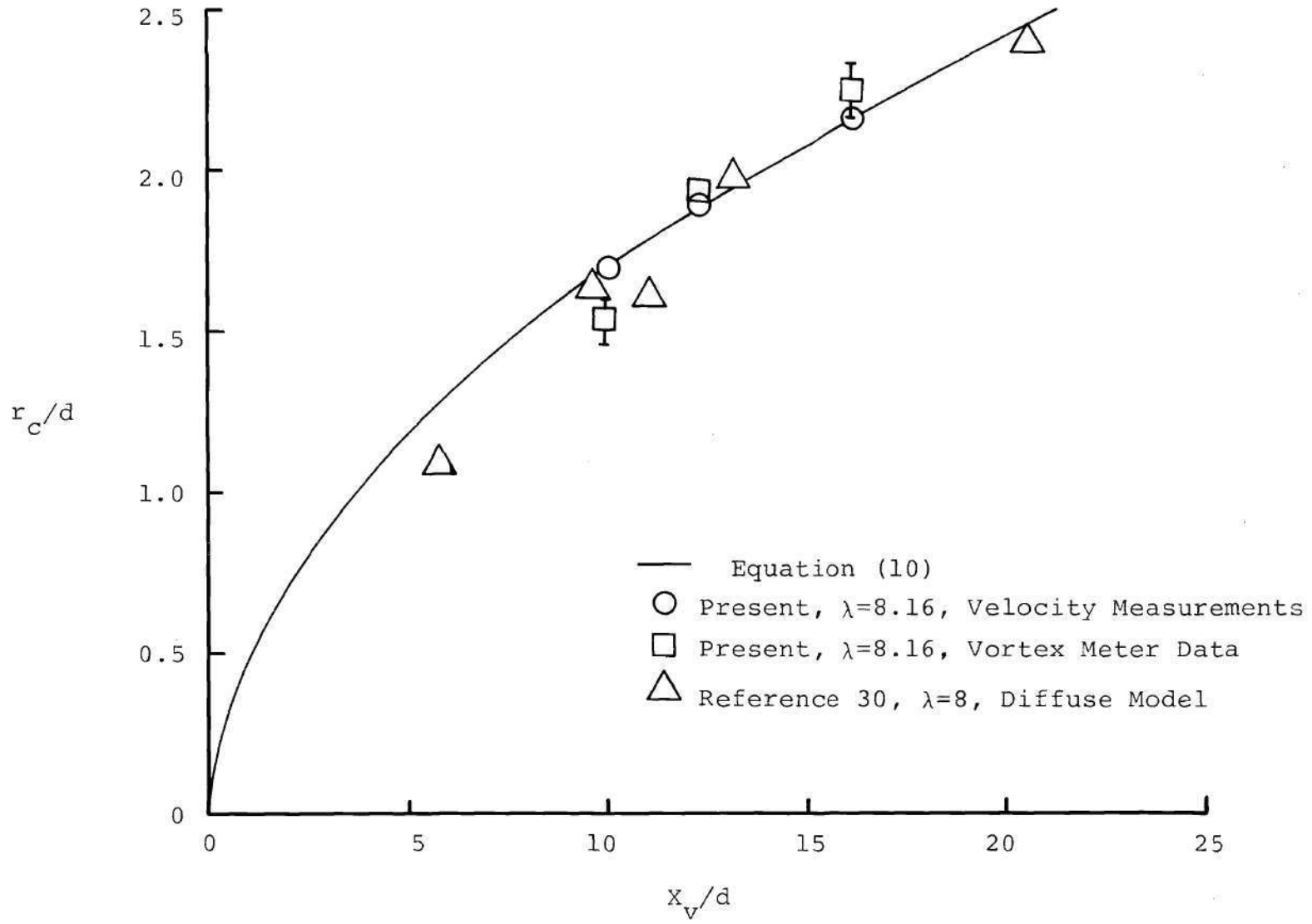

Figure 33. Vortex Core Radius Distribution.

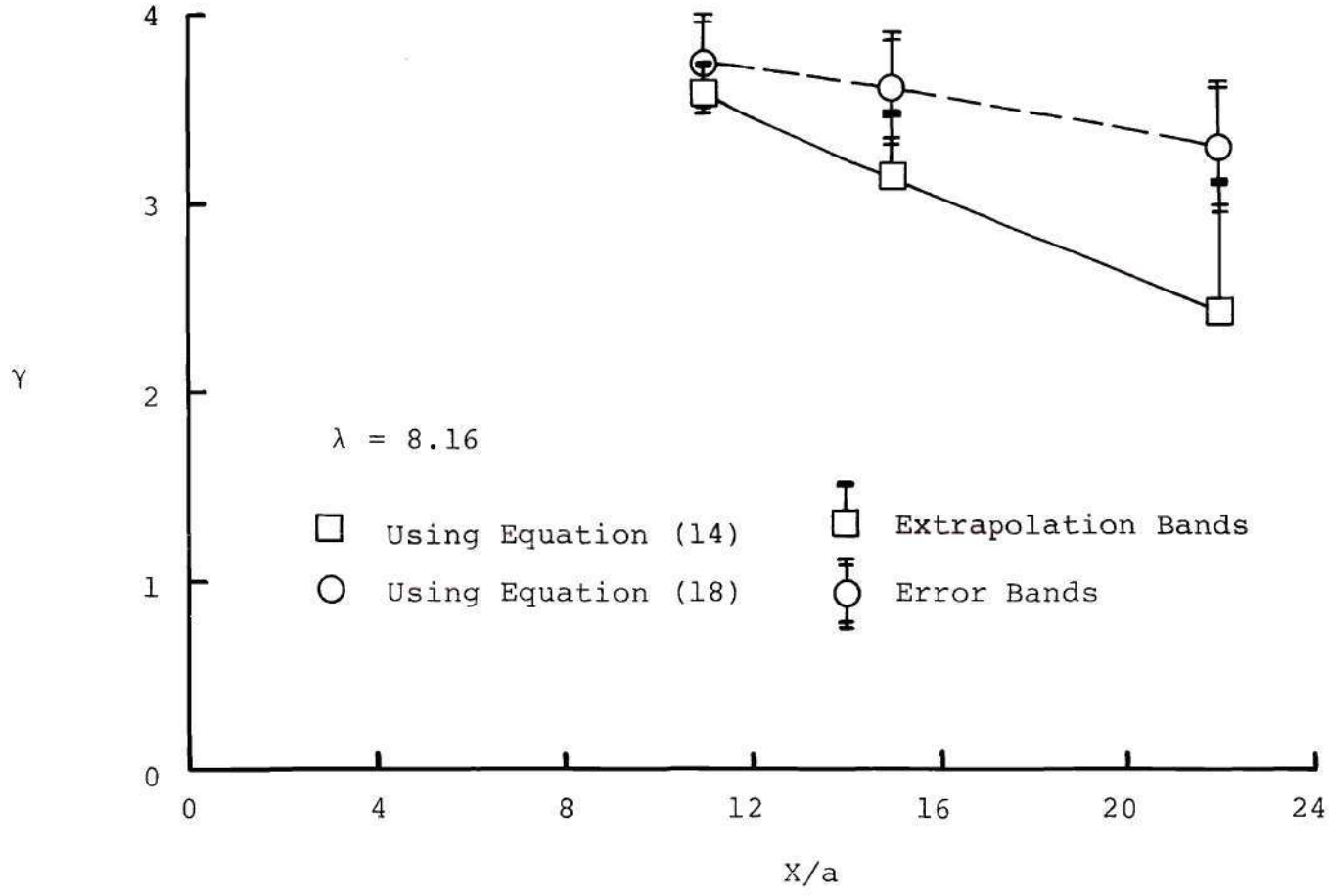

Figure 34. Estimation of Vortex Strength Distribution.

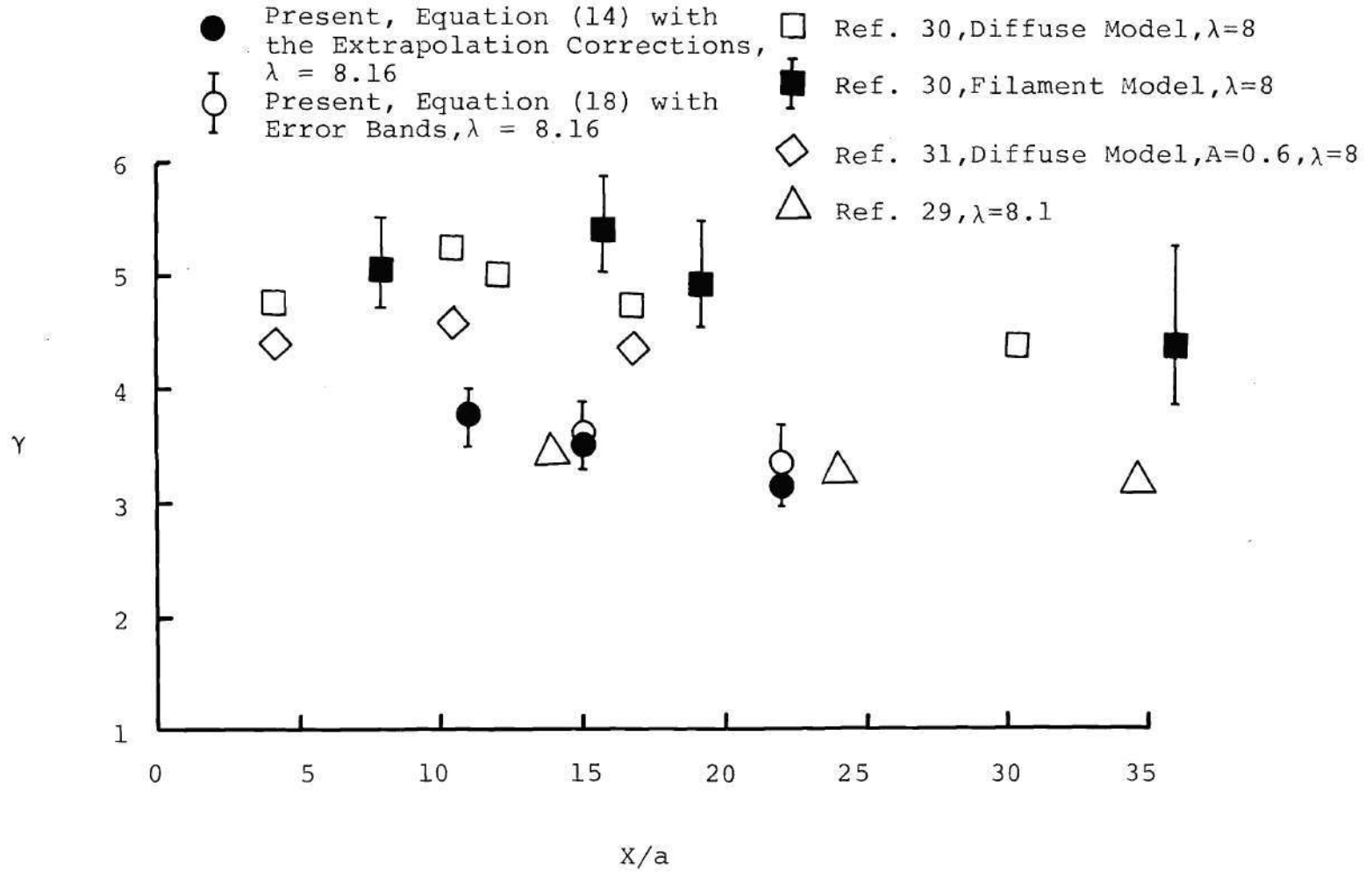

Figure 35. Vortex Strength Distribution - Comparison with Other Investigations.

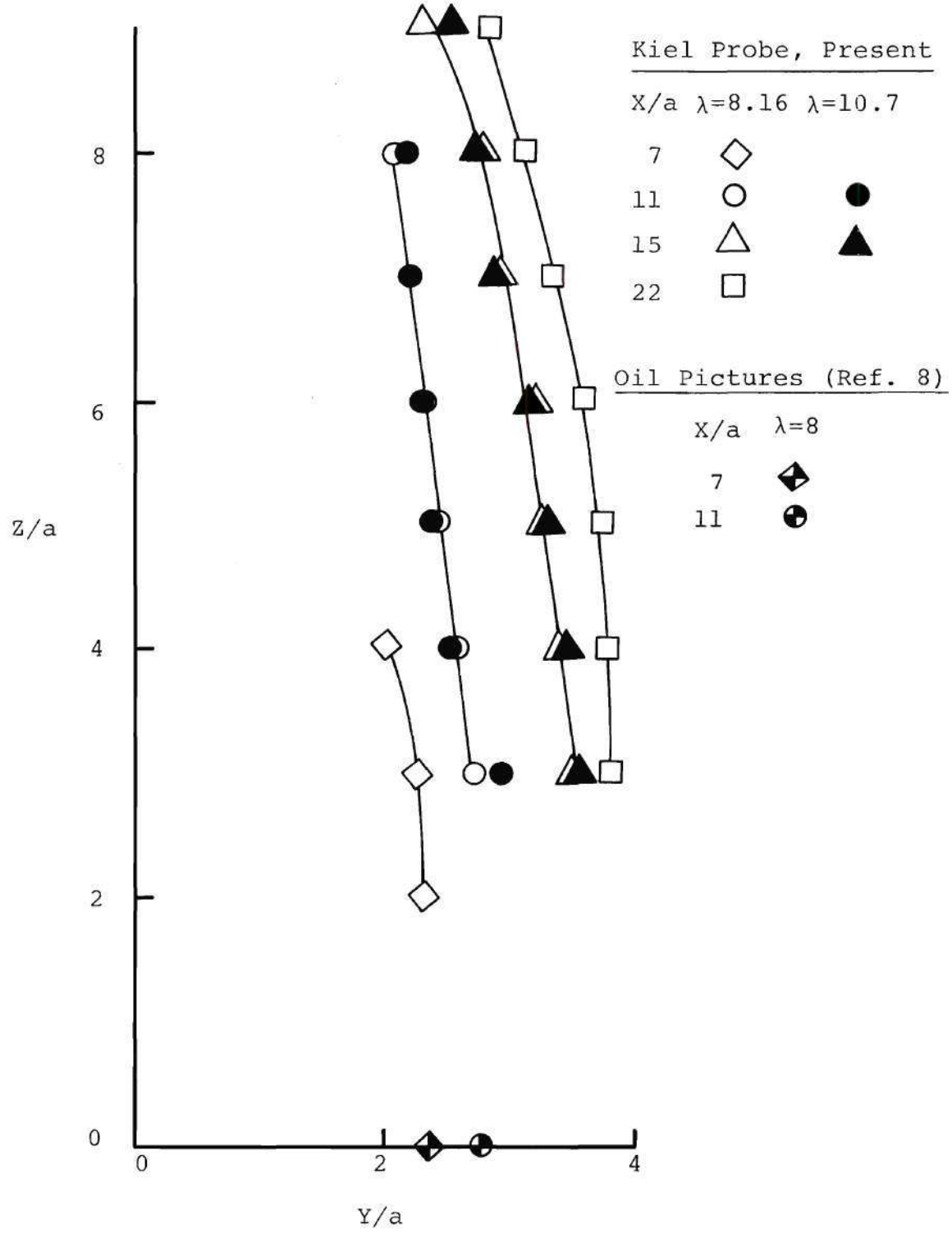

Figure 36. Wake Edge.

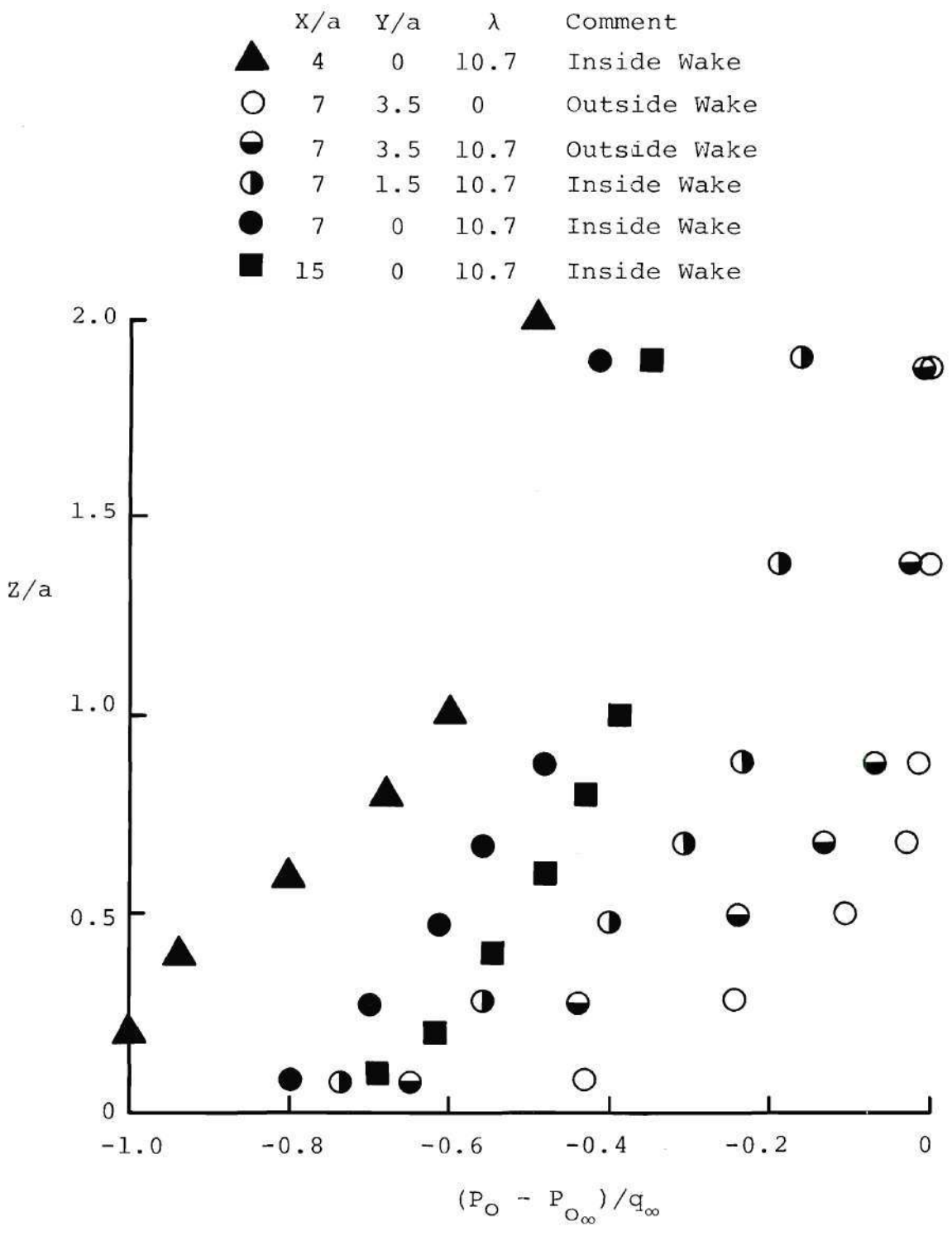

Figure 37. Total Pressure Profiles Near Flat Plate.

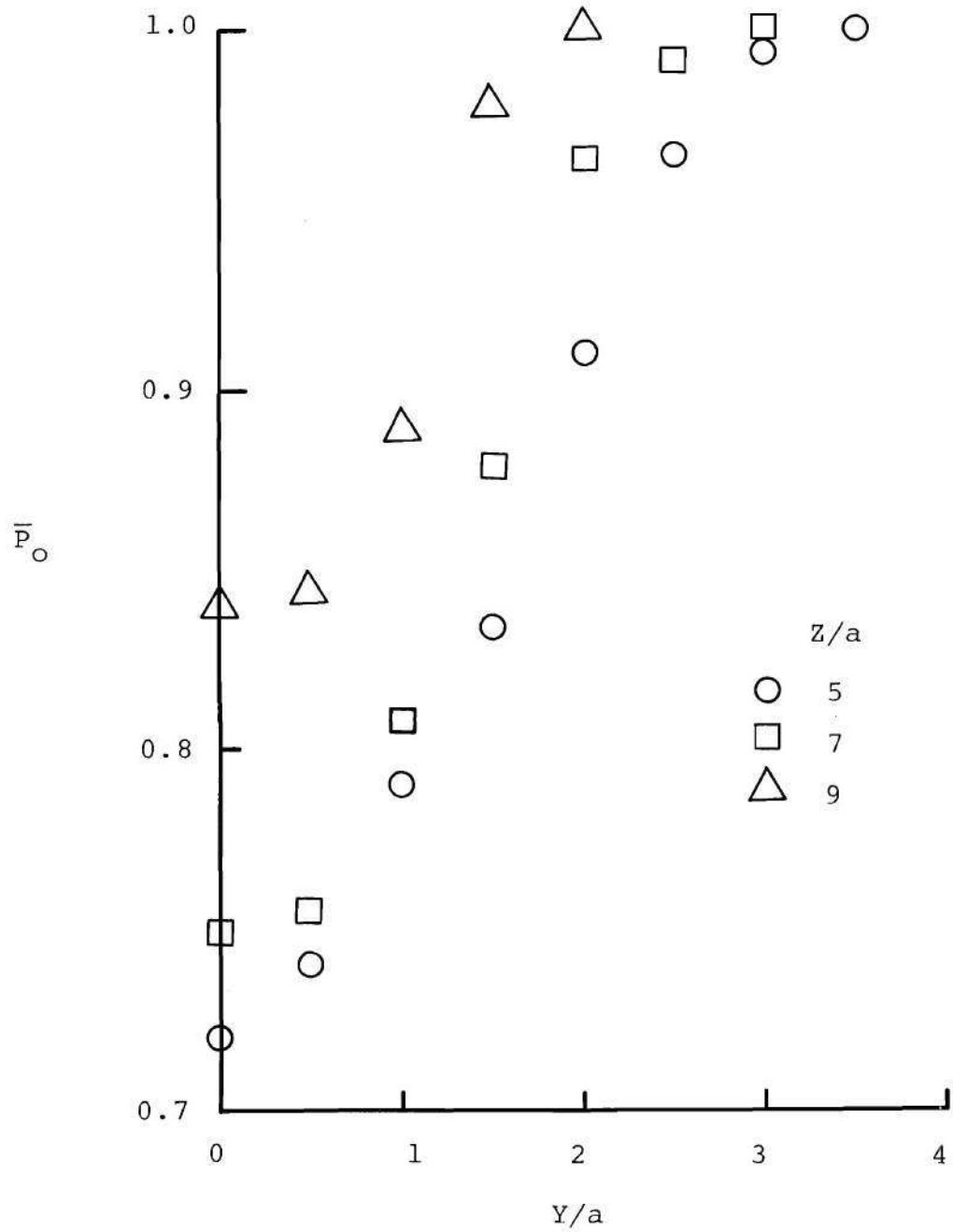

Figure 38. Total Pressure Distributions in the Wake, X/a = 11, λ = 8.16.

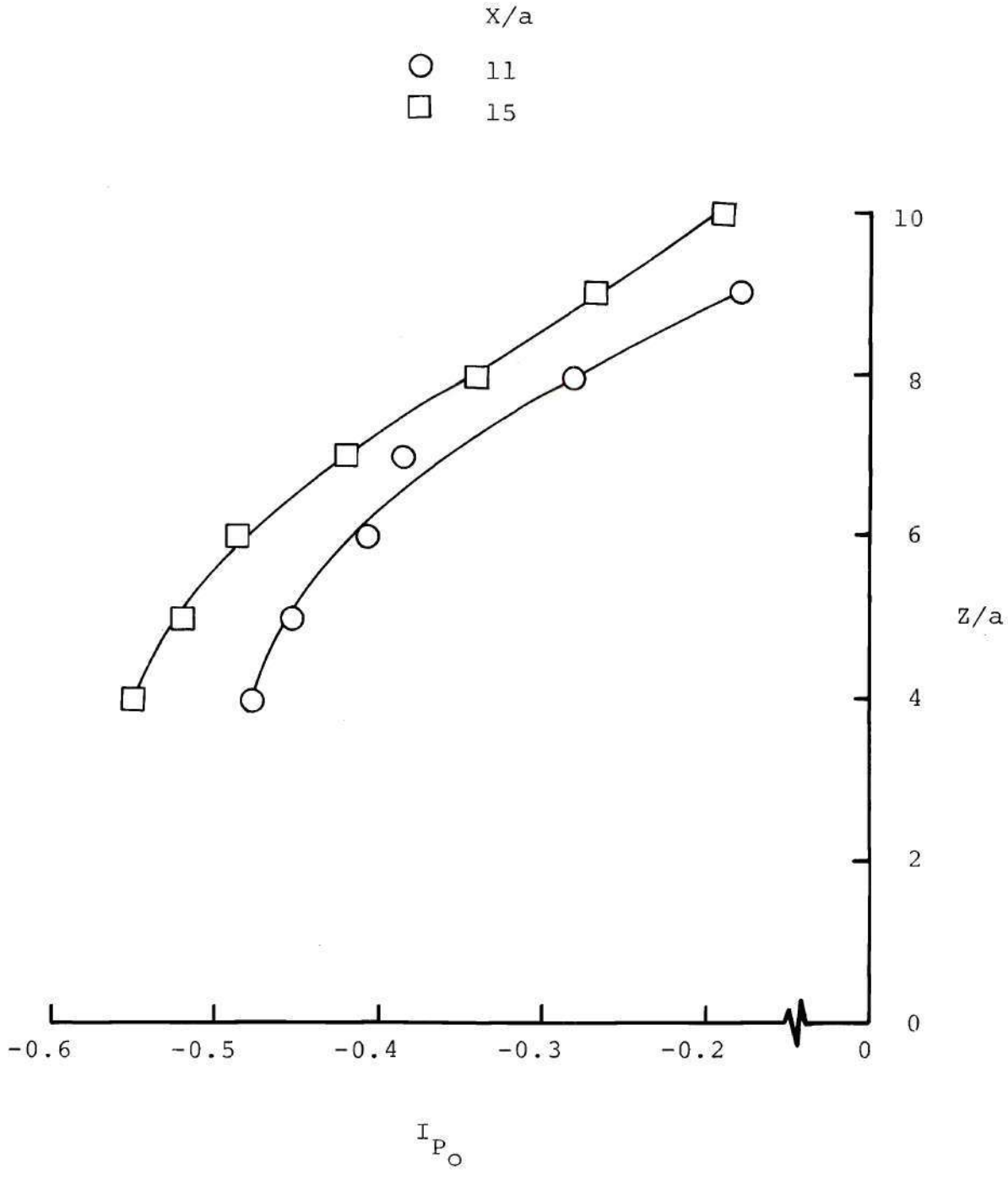

Figure 39. Integrated Total Pressure Loss in the Wake, $\lambda = 8.16$.

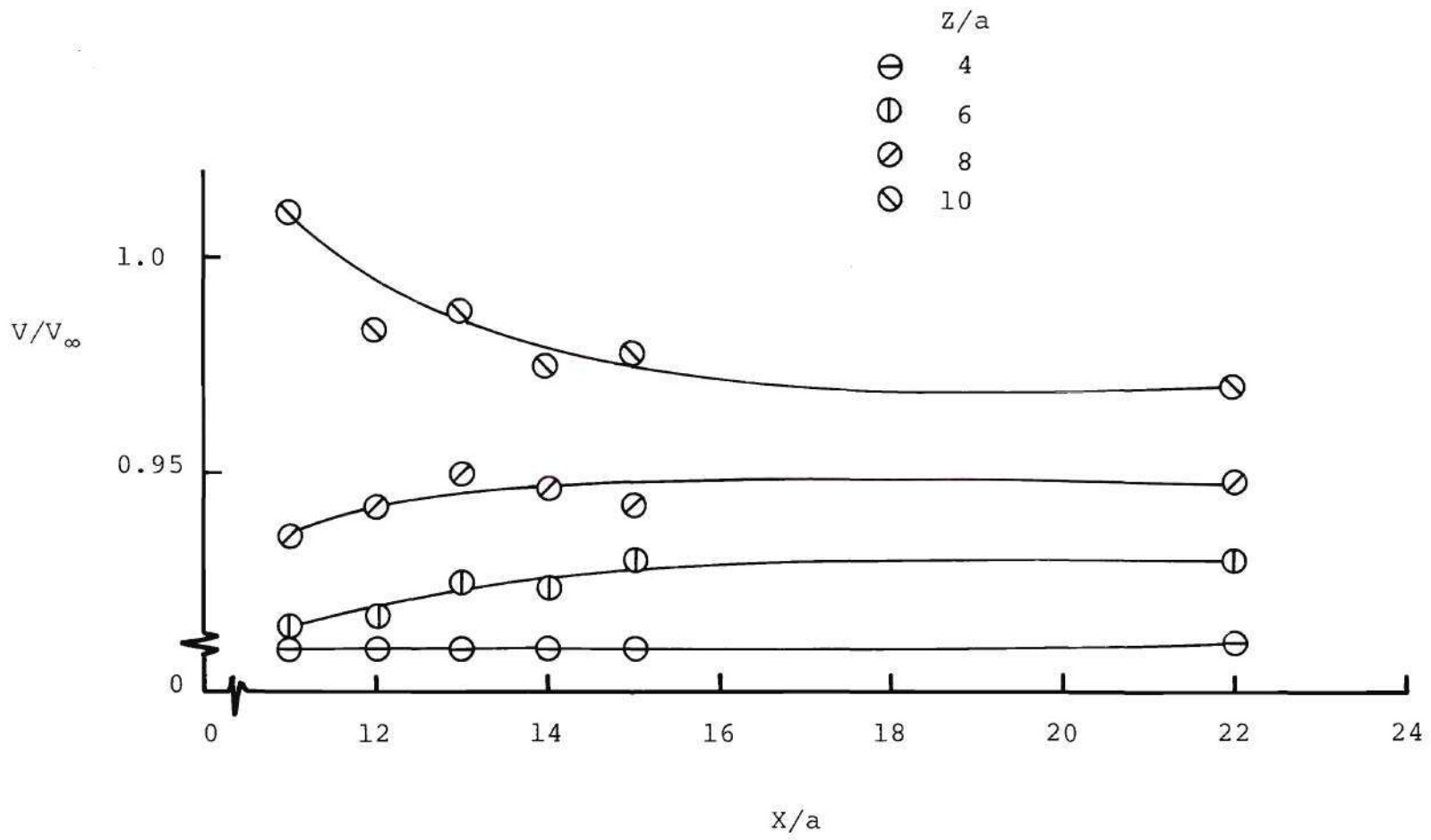

Figure 40. Symmetry-Plane Total Velocity Distributions in the Wake, Y/a = 0, λ = 8.16.

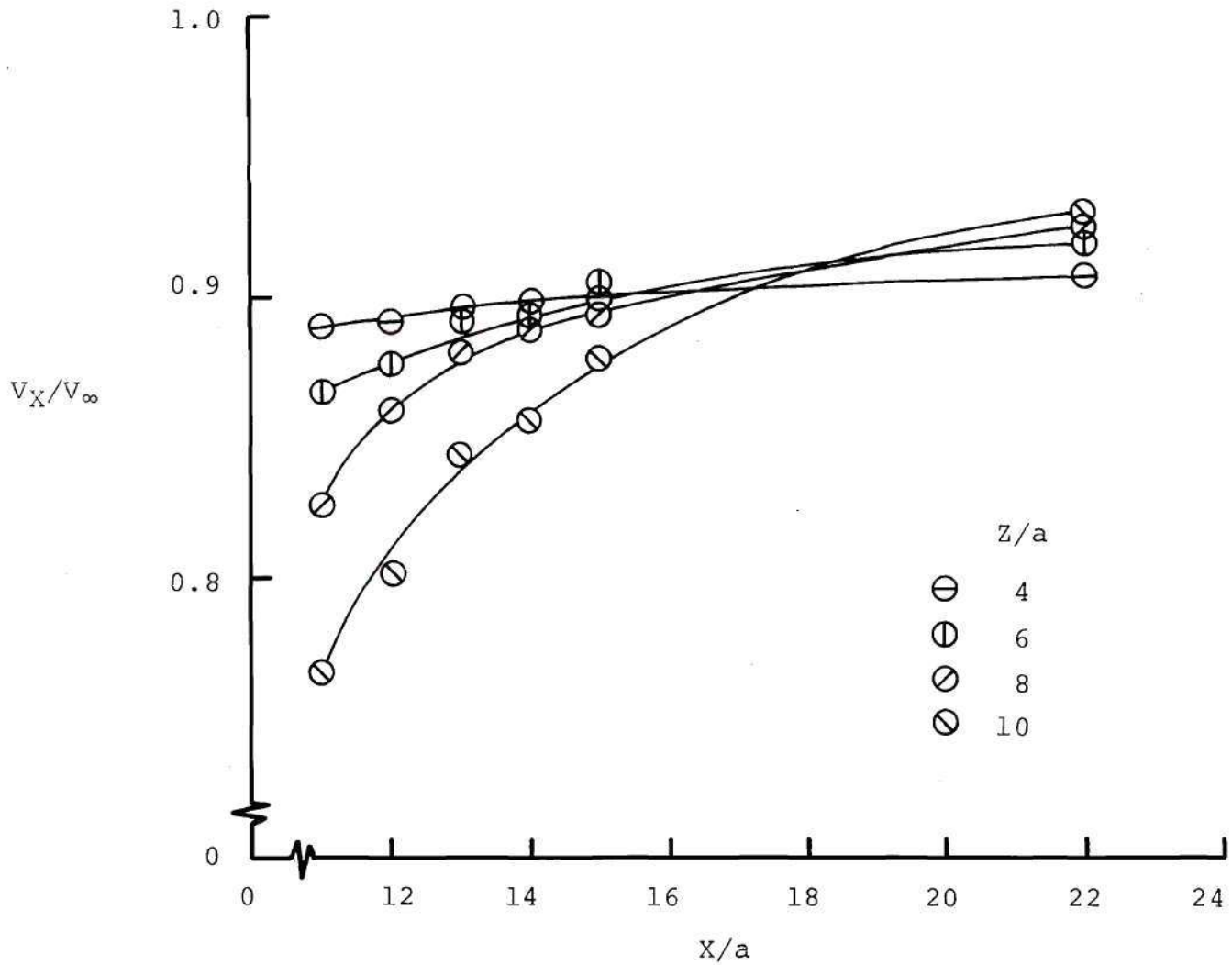

Figure 41. Symmetry-Plane Axial Velocity Distributions in the Wake, Y/a = 0, λ = 8.16.

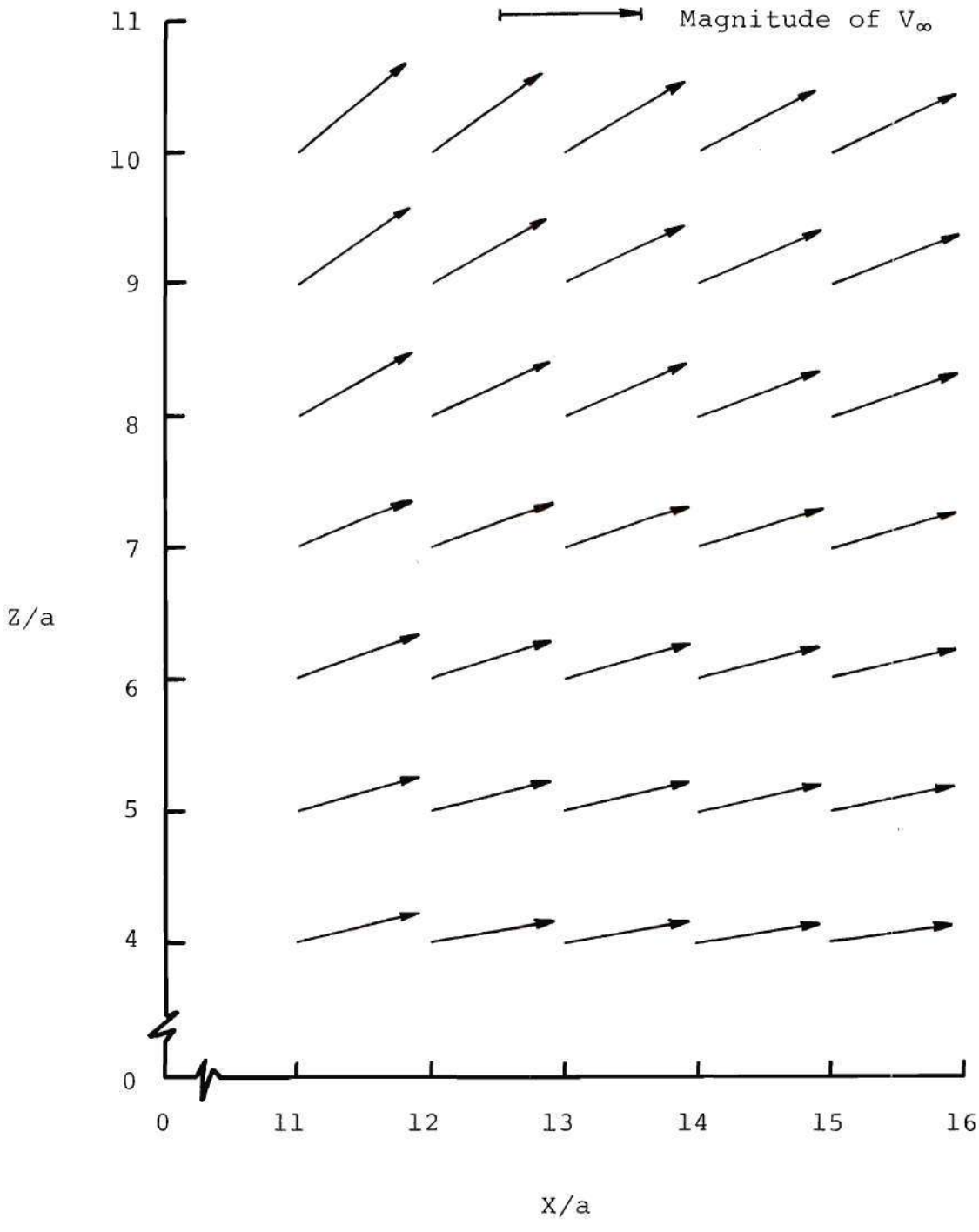

Figure 42. Symmetry-Plane Velocity Vectors in the Wake, Y/a = 0, λ = 8.16.

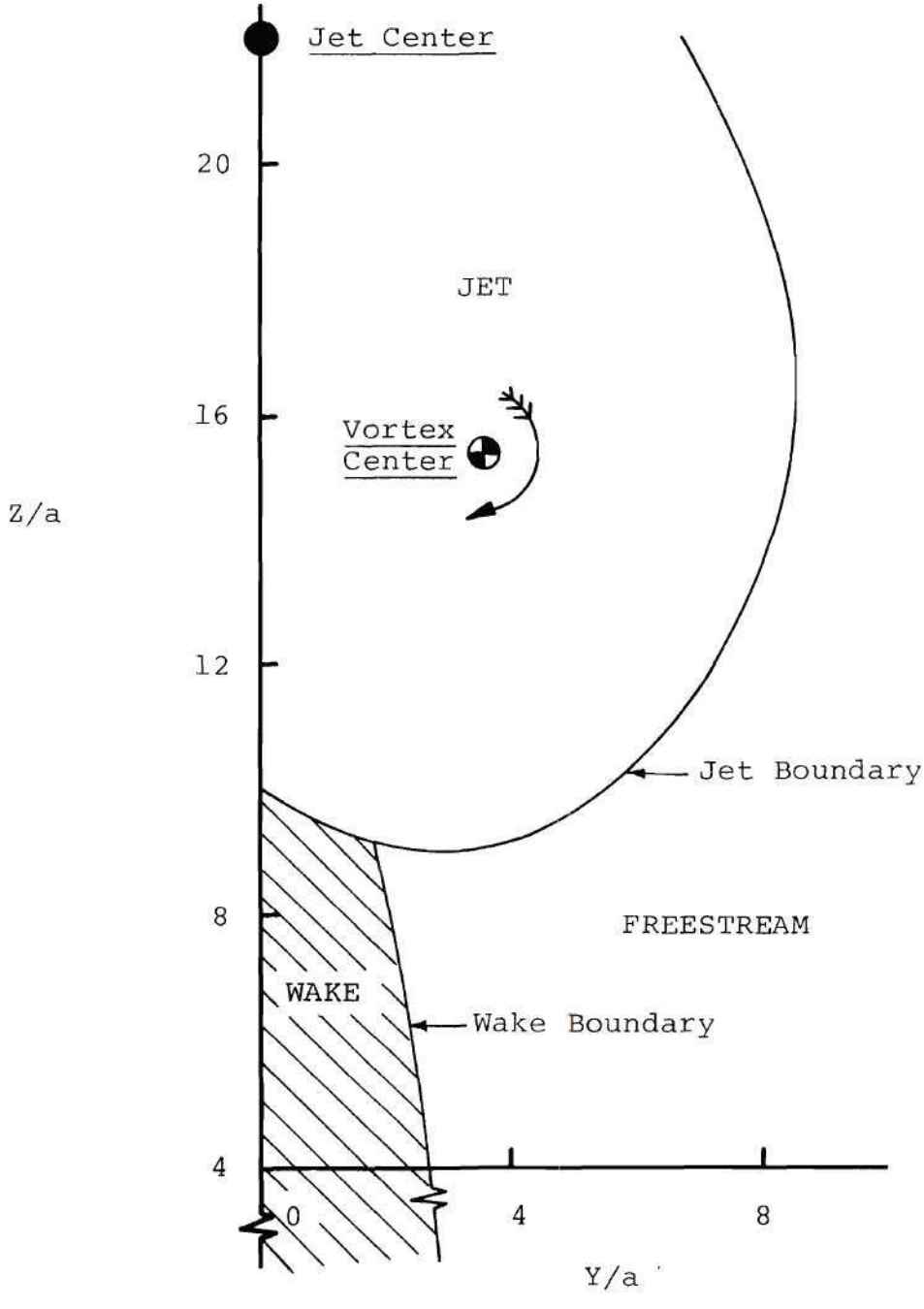

Figure 43. Jet and Wake Regions, X/d = 5.5, λ = 8.16.

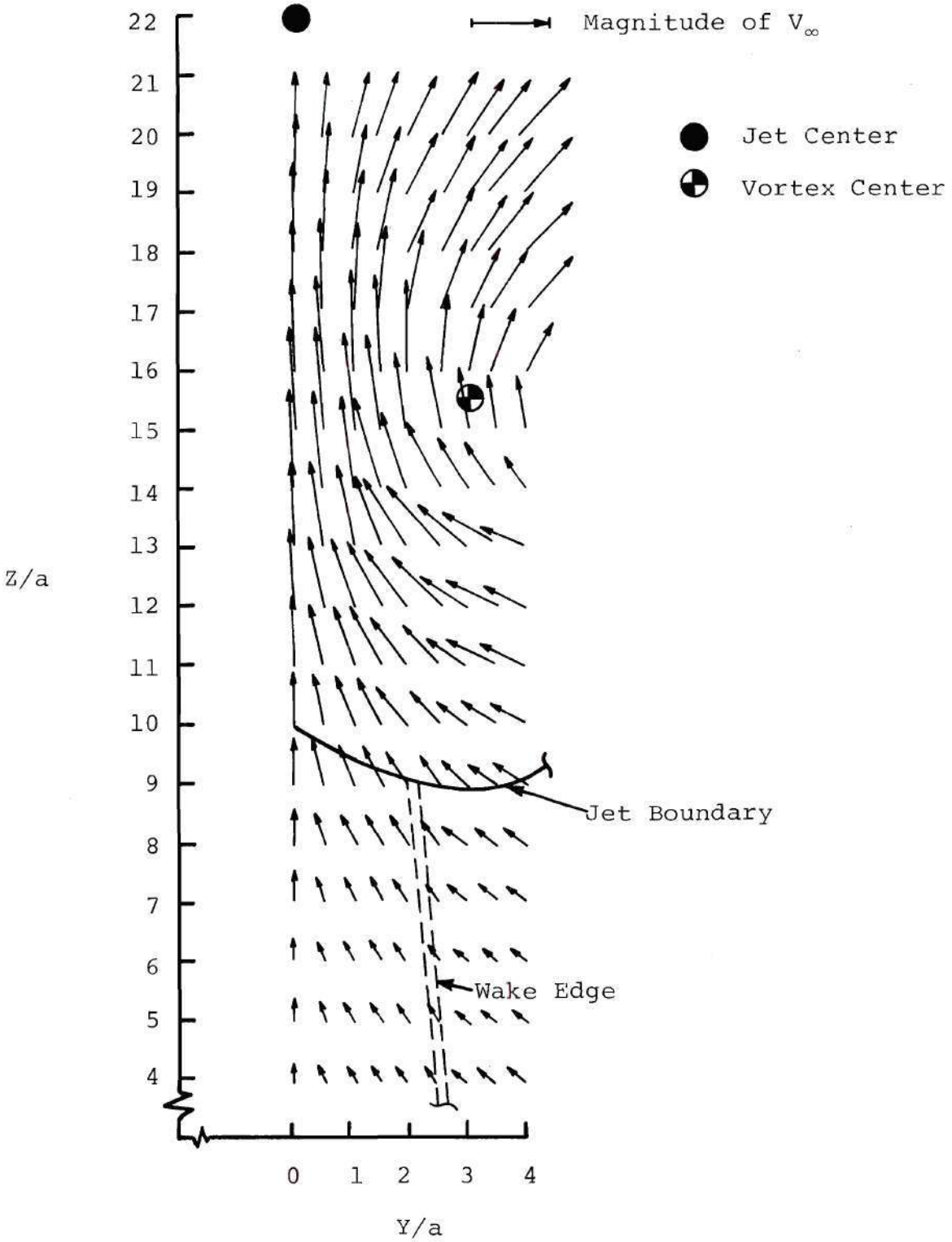

Figure 44. Velocity Vectors, X/d = 5.5, λ = 8.16.

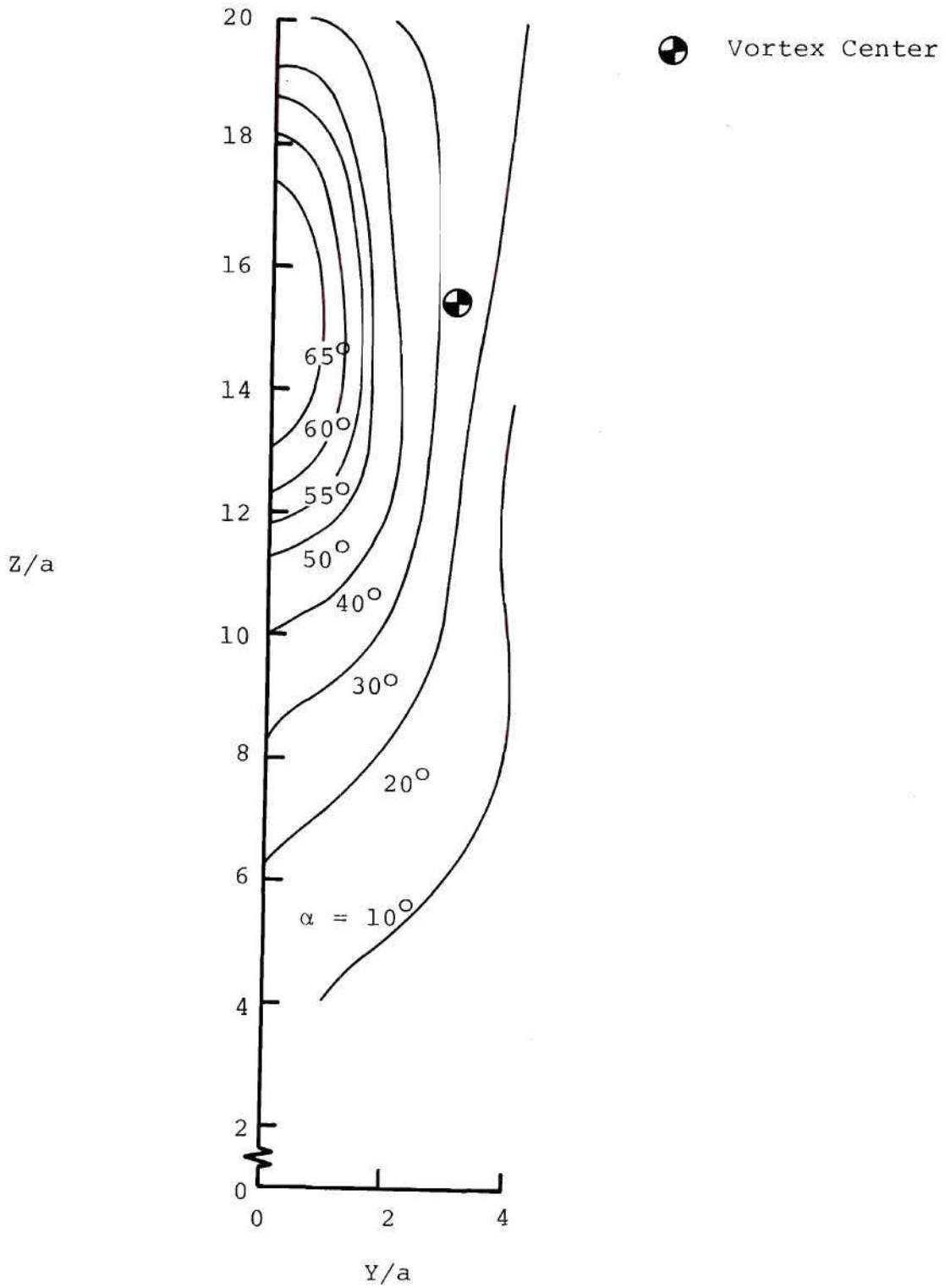

Figure 45. Upwash Angle Contours, X/d = 5.5, λ = 8.16.

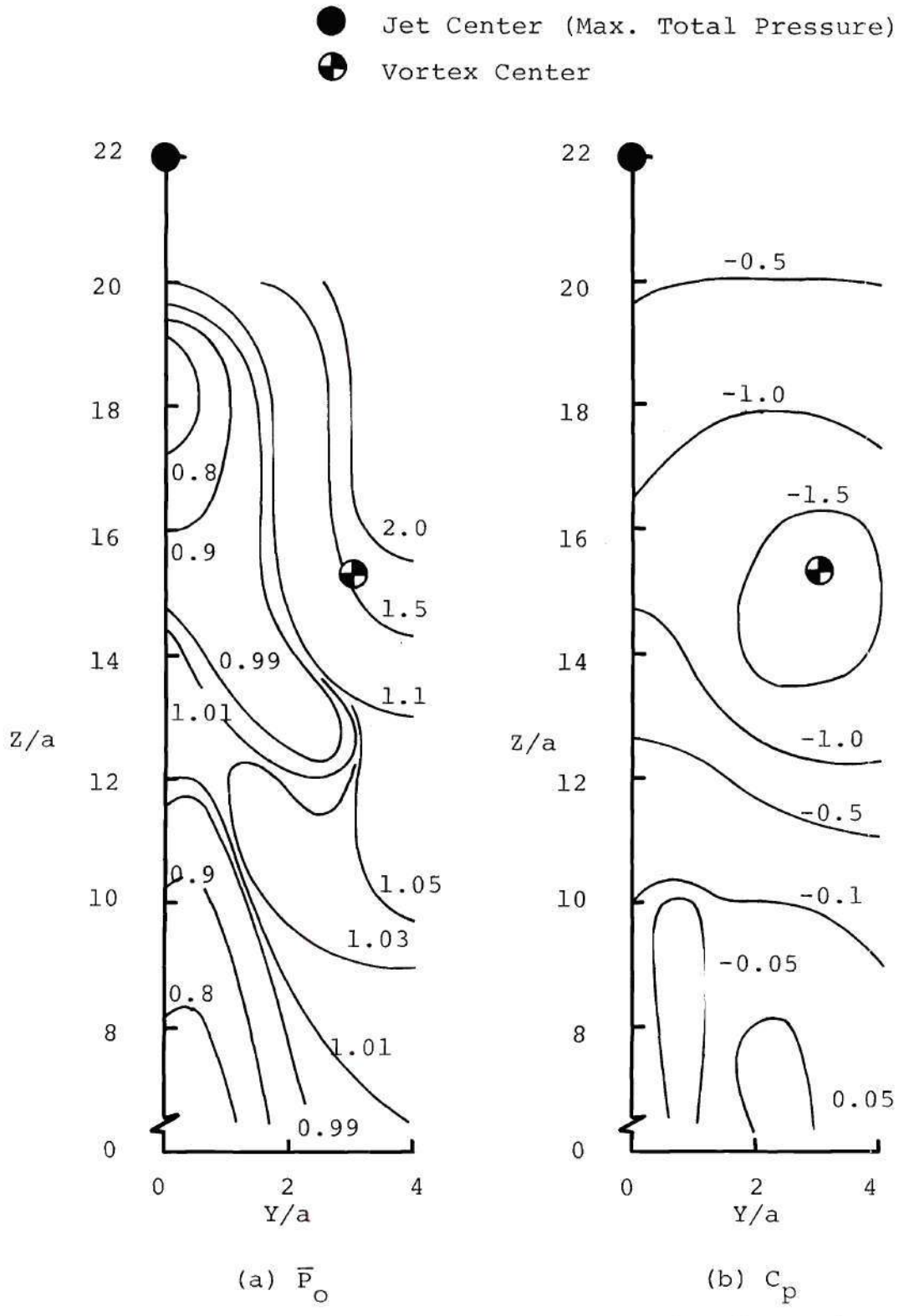

(a) $\bar{P}_o$ (b) C_p

Figure 46. Curves of Constant Total and Static Pressure, X/d = 5.5, λ = 8.16.

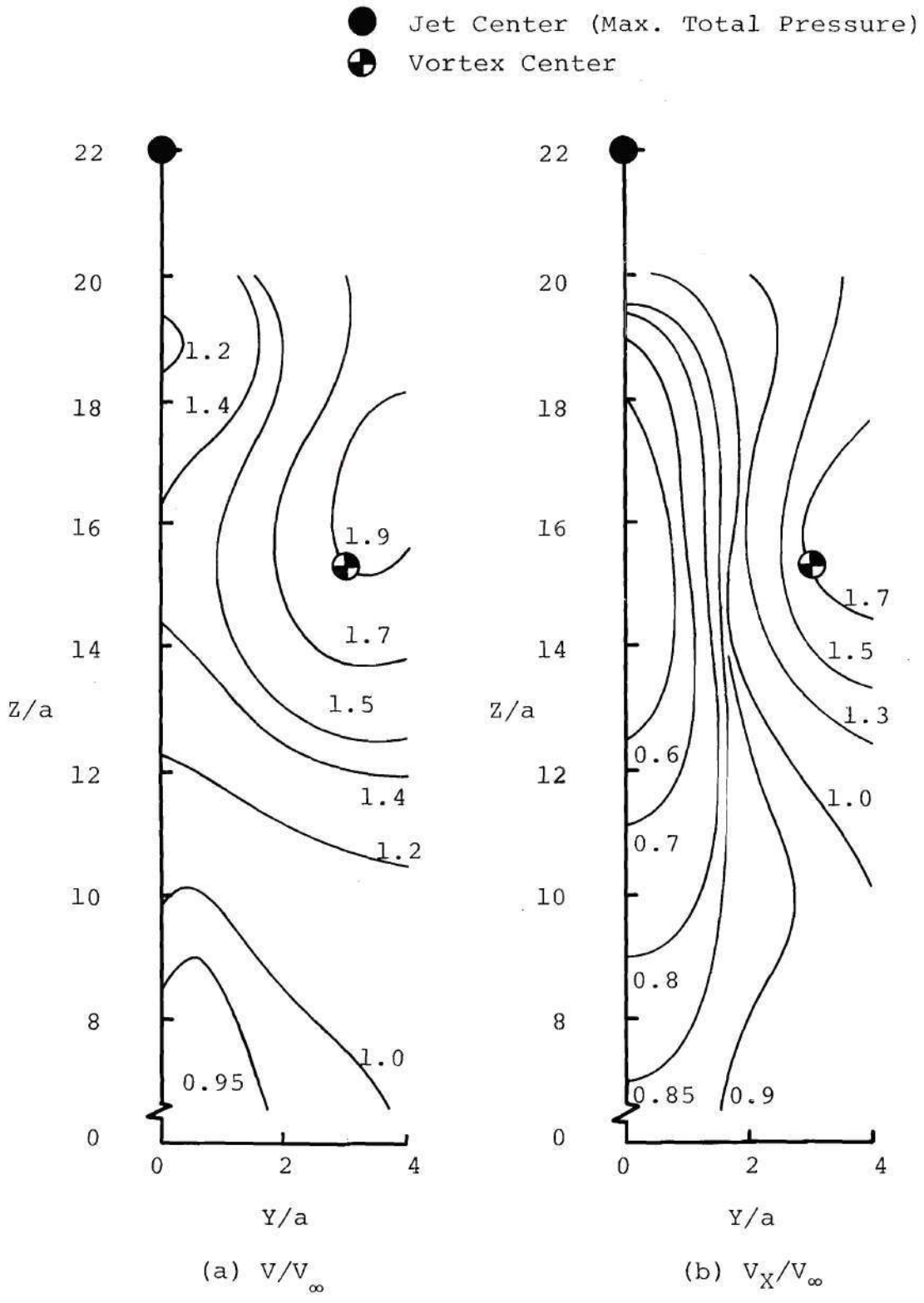

Figure 47. Curves of Constant Total and Axial Velocities, X/d = 5.5, λ = 8.16.

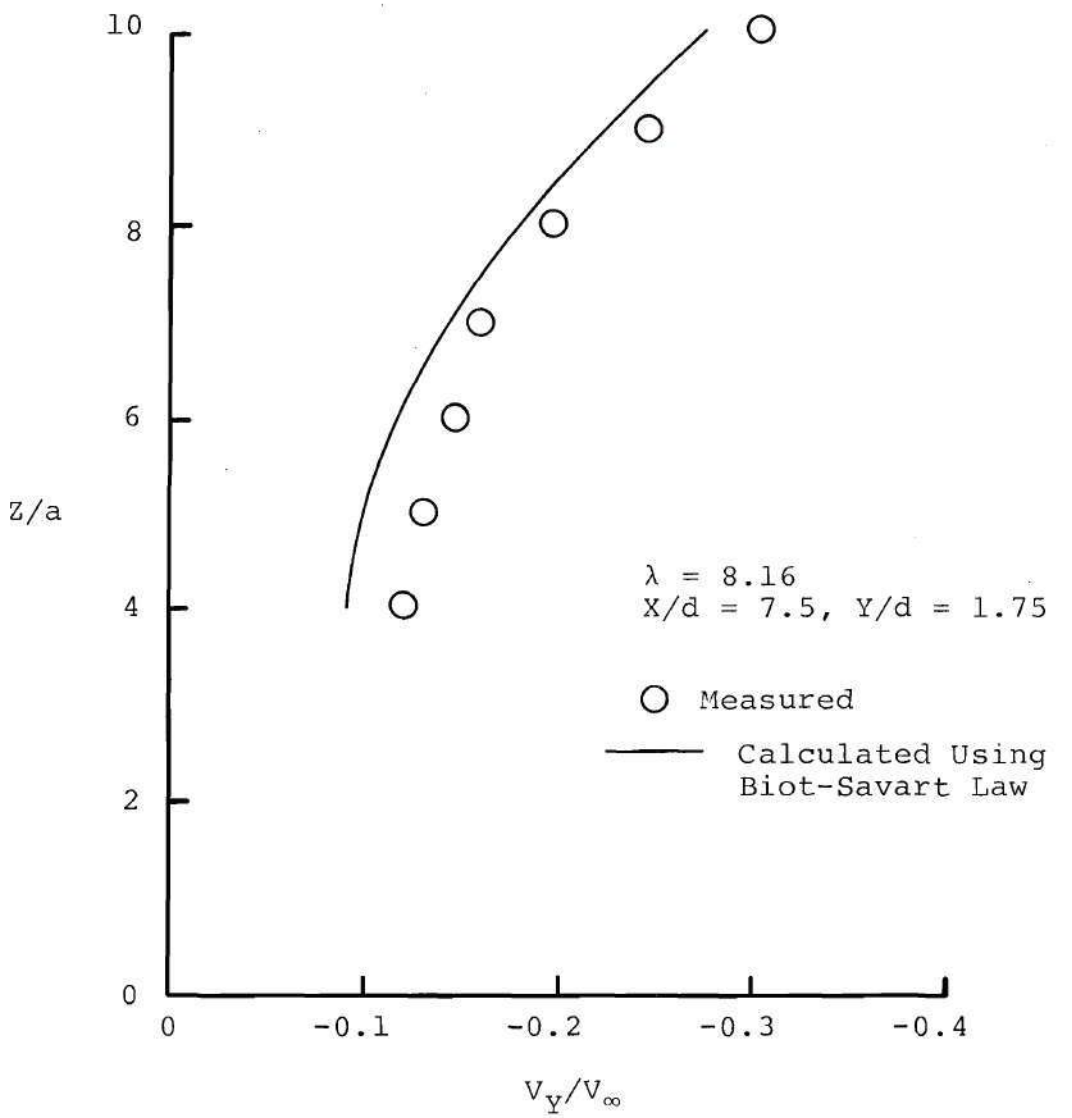

Figure 48. Lateral Inflow Velocity Distribution.

APPENDIX A

USE OF THE VORTEX METER

In this Appendix, the vortex meter support design first is discussed and then certain problems encountered in the use of the vortex meter as regards its handling, lubrication, and instrumentation are discussed.

Vortex Meter Support System

Figure 10 shows the vortex meter and its support system. The main requirement of the support is that, when it is necessary to orient the vortex meter so as to be able to make vorticity measurements in planes normal to the vortex curve, the spatial location of the blade vanes of the meter should not change. This aspect was taken care of by holding the meter at its threaded section so that the blade vanes of the meter always remained aligned with the axis about which the probe was rotated by the actuator.

Another aspect of importance is that the electrical leads for the photocell and the battery connections for the vortex meter should come out of the meter through the same threaded section which is used to hold the meter. The vortex meter had to be removed from its support for lubrication very frequently. Care was taken in the support design

to ensure that the leads did not get twisted and cut when mounting the vortex meter back on its support.

Handling, Lubrication, and Read-Out Instrumentation

The most time-consuming problems in using the vortex meter were the lubrication and the checks of performance with the calibrating device. As mentioned elsewhere, the performance of the vortex meter had to be checked very frequently (every 2 to 5 hours of use) by putting the calibrating device on the meter and testing the assembly in the wind tunnel flow (jet off). One encounters difficulty in putting the calibrating device on the vortex meter and then taking it off again without damaging the blade vanes or the delicate shaft on which the hub of the vanes is mounted. The clearance between the tip of the vanes and the internal diameter of that portion of the calibrating device which goes over the vanes is only about 0.063 inch. The mounting of the calibrating device was accomplished with the aid of a wooden block with a V-groove to support the calibrating device and a table which could be adjusted in height.

Frequent checks on the lubrication of the vortex meter were made during the tests. When lubrication was required, the vortex meter had to be opened and a very small amount of commercial oil put in the rear thrust bearing and in the front bearing (which can be lubricated without opening).

The main problem encountered was the tendency to overlubricate the rear bearing. In the jet in crossflow, because measurements were made with the axis of the meter oriented downwards, a very slight excess of oil resulted in the oil running down the shaft and impairing the passage of the light from the bulb to the photocell. The normal voltage output of the photocell was about 40 mv d.c., and the trigger level on the counter was set so as to sense pulses of magnitude of about 25 mv d.c. or higher. Any overlubrication was found to reduce the voltage output considerably (to less than 5 mv d.c.). At such a low output level the counter would not respond accurately. The time taken in making sure that the lubrication was precisely correct was considerable.

The main problem encountered with regard to the instrumentation was that noise could significantly affect the triggering of the counter. A filter was used to eliminate high-frequency noise. A low-pass setting of 400 Hz was maintained on the filter so that the input to the counter was restricted to the vortex meter pulses within the frequency range of 0 to about 400 Hz. This frequency range was found to be quite adequate for the values of vorticity measured in the tests.

It was found during the tests that the quality of data could only be assured by a constant monitoring of the vortex meter output on a dual-beam oscilloscope both before

amplification and filtering and afterwards. The levels of the vortex meter output and the quality of the data read by the counter were displayed on an oscilloscope throughout the tests.

APPENDIX B

EVALUATION OF VORTEX METER BY MEASUREMENTS IN A WING TRAILING VORTEX

In this Appendix, measurements of the strength of a trailing tip vortex shed from a finite wing are discussed. These measurements were made using the vortex meter (giving local mean flow vorticity) and the 5-hole pressure probe (giving velocity, hence circulation). As mentioned in Chapter III, the aim of this investigation was to verify the calibration of the vortex meter, evaluate the constants supplied with the vortex meter, and check the accuracy of the vortex strength values predicted by the vortex meter.

Generation of Vortex

It is difficult to generate flows containing vortices of precisely known strength. For the vortex meter to be able to sense vorticity, the vorticity filament should have motion in the direction of the vortex meter axis with a significant axial velocity of known value. This suggested utilizing the trailing vortex behind a wing. However, for a wing trailing vortex, theoretical predictions of the vortex strength of the rolled-up vortex at any chord length downstream are not very reliable. For example, May[42] compared theoretical

predictions of the strength of the trailing vortex behind a wing of known geometry at an angle of attack with that measured by a vortex meter. The discrepancy in the comparison was significant, with the measured value of the vortex strength being lower than the predicted value by 30%. In order to utilize the trailing vortex sheet behind a wing to calibrate a vortex meter, Margason and Fearn[32] measured (immediately behind the trailing edge) the distribution of the strength of the trailing vortex sheet shed from a rectangular-planform wing. The calibration was accomplished by correlating revolutions of the vortex meter at several spanwise locations with the predicted distribution of the strength of the vortex sheet obtained by using the measured value of the wing lift and a calculated lift distribution. The correlation was good in regions from 30 to 95 percent of the half-span, and these measurements were used to establish the vortex meter calibration.

In the present investigation, vortex meter measurements were compared with values of the vortex strength and local vorticity obtained by using the 5-hole pressure probe described in Chapter II, i.e. with the strength as determined by circulation and the local vorticity as gotten by differentiation. In doing so, the dependence on theoretical predictions is eliminated; however, it is

recognized that measurements with the 5-hole pressure probe are not free from error. The maximum uncertainty in the velocity measured by the 5-hole pressure probe was ± 2.5%.

A half-wing was constructed having a chord of 9.25 inches, semi-span of 21.25 inches, and a maximum thickness of approximately 25 percent of the chord-length. The half-wing had a symmetrical cross section (approximately equivalent to that of the NACA 0025 section) and a rounded tip. The wing was mounted vertically on the flat plate in the Georgia Tech nine-foot wind tunnel and set at an 8^{o} angle of attack.

Procedure

Figure B-1 is a schematic diagram showing the areas of measurement and the axis system employed for the measurements in the wing trailing vortex. The vortex was generated using a constant freestream velocity (V_{∞}) of 113 fps. All of the measurements were made in a plane normal to the freestream (plane Y'-Z') and the plane was located approximately 3.8 chord lengths downstream of the wing trailing edge. The axis of the vortex meter was aligned in the horizontal direction in order to measure vorticity in the direction of the freestream. Data, N, in cycles per second (CPS) were obtained with the vortex meter at about 350 points which were 0.25 inch apart. The 4 inches x 5 inches region (Y'-Z')

within which the vortex meter data were taken was essentially enclosed in the square region C_0 shown in Figure B-1. The center of the vortex was located as the point of maximum vorticity and the vorticity distribution was also measured along the centerline L_0 (on the axis Z'). The vortex meter data were converted from the recorded values of N to vorticity values as explained in a later portion of this Appendix.

Using the 5-hole pressure probe, velocity components were measured along the lines L_0, L_1, and L_2 shown in Figure B-1. These lines are parallel to the Z'-axis and the spacing between L_1 and L_0, and between L_2 and L_0, is 0.125 inch. Velocity components were also measured at points (16 per circuit) on the circuit C_0 of size 5 inches x 5 inches and around one larger circuit C_1 8 inches x 8 inches in size.

The instrumentation and the data acquisition system for the vortex meter are described in Chapters II and III. The values of N which were recorded were the averages of three values, with each value gotten by integration over a ten second period, as explained in Chapter III. The vortex meter was lubricated periodically. Its performance was checked with the calibrating device and found to remain within ± 1 CPS of the standard 260 CPS at 110 fps. The repeatability and the observed fluctuations in the vortex meter data are described in the next section of this Appendix.

For the 5-hole pressure probe, the Barocel pressure measurement system, with a pressure transducer of 10 mm mercury range, was employed. Voltage values were read on a Fluke 8000A digital voltmeter and both the average and the fluctuations in the voltage output were recorded.

The data were reduced and analyzed as follows :

1. Vorticity values were obtained from the values of N recorded from the vortex meter measurements using the equation

$$\omega_{X'} = 2\pi N/\eta \qquad \text{(B1)}$$

where η is the frictional efficiency of the vortex meter and, as defined in Chapter III,

$$\eta = \frac{1}{(1 + K/V_{X'})}$$

where K is the constant supplied by the manufacturer. The value of $V_{X'}$ is needed at every data point to be able to calculate vorticity from the vortex meter data. Measurements with the 5-hole pressure probe showed that the $V_{X'}$ values along lines L_0, L_1, and L_2 varied by a maximum of ± 6 percent of the freestream value. Since it was estimated that this variation in $V_{X'}$ would give only about ± 1.2 percent uncertainty in the local vorticity value, $V_{X'}$ was

considered as a constant with its value as the freestream velocity (V_∞). The value of η was calculated using V_∞ as the axial velocity and was found to be 0.8, and this value was used in the data reduction. Contours of constant vorticity were drawn in the Y'-Z' plane to check the symmetry of the vortex.

2. The vorticity distribution on the centerline, L_0, was expressed mathematically as a Gaussian

$$\omega_{X'} = \omega_{X'_o} e^{-\beta^2 r'^2} \tag{B2}$$

where $\omega_{X'_o}$ is the value of vorticity at r' = 0 and β is the diffusion constant. The value of β was found from curve fits to the measured vorticity distribution.

The Gaussian distribution is used later to predict the vortex strength mathematically.

3. Velocity components obtained by traversing the 5-hole pressure probe along lines L_0, L_1, and L_2 were reduced to give vorticity values on the line L_0, namely

$$\omega_{X'} = \frac{\partial V_{Z'}}{\partial Y'} - \frac{\partial V_{Y'}}{\partial Z'} \quad . \tag{B3}$$

Partial derivatives were calculated using the central difference technique.

4. Using the measured local vorticity values in the region C_0, the vortex strength, Γ, was calculated from the expression

$$\Gamma = \iint_{C_0} \omega_{X'} \, dA \tag{B4}$$

where dA is an elemental area in the region C_0. The numerical value of the double integral was evaluated using mechanical cubature with Simpson's rule.

It is noted here that the error associated with the calculated Γ value due to the variations in V_X, is much less than the ± 1.2 percent possible error in individual vorticity values. The error in the Γ value is estimated to be less than ± 0.5 percent.

5. From the Gaussian distribution (Equation (B2)), assuming that the vortex is symmetric, Γ was calculated as

$$\Gamma = 2\pi \int_0^\infty \omega_{X'_o} e^{-\beta^2 r'^2} \, r' \, dr' = \pi \omega_{X'_o} / \beta^2 \quad . \tag{B5}$$

6. Measurements (using the 5-hole pressure probe) of the velocity components along the closed circuits were used to calculate line integrals for the circuits C_0 and C_1 as

$$\Gamma = \oint_{C_0 \text{ or } C_1} \vec{V} \cdot d\vec{l} \qquad (B6)$$

where dl is an infinitesimal line segment on the circuit C_0 or C_1. Average velocities over segments (1.25 inches long for C_0, 2.0 inches long for C_1) were used to calculate the line intergral.

Results and Discussion

The vorticity distribution obtained by traversing the vortex meter along the line L_0, which passes through the vortex center, is shown in Figure B-2. The maximum error bands shown in the figure are estimated from the observed fluctuations in the values of N for three 10-second-average readings. The figure also shows the repeatability of the vortex meter measurements between different runs. The maximum vorticity obtained at the center of the wing-tip vortex was 1774 radians/sec.

The vortex meter measures vorticity which is really the average over the spinner area. The size of the spinner in comparison to the size of the vortex is shown in Figure B-2. The error in measured vorticity due to the finite size of the spinner is related to the curvature of the vorticity distribution. The vortex meter overpredicts vorticity values for a concave-upward curve and vice versa. Corrections in vorticity

values can be made by iteration, but the procedure is very cumbersome. It is estimated that these corrections are well within the error bands in the present case. In addition, since errors compensate each other, they do not add cumulative error to the total vorticity flux (vortex strength) as much as they affect individual vorticity values.

Figure B-3 shows contours of constant vorticity obtained by the vortex meter in the region enclosed by the circuit C_0. The contours are slightly elliptical rather than the circular curves one would expect in an ideal, isolated, and completely rolled-up vortex.

McCormick and Surendraiah[43] made measurements similar to Figure B-2 with a vortex meter in order to obtain the vorticity distribution on the centerline of a wing-tip vortex. They show that the vorticity distribution is of the form

$$\omega_{x'} = \omega_{x'_o} e^{-(r'/r'_{\frac{1}{2}})^2 \ln 2} \tag{B7}$$

where $r'_{\frac{1}{2}}$ is the value of r' for which $\omega_{x'} = \omega_{x'_o}/2$. Equation (B6) can be expressed as a Gaussian distribution

$$\omega_{x'} = \omega_{x'_o} e^{-\beta^2 r'^2} \tag{B8}$$

where $\beta = (\ln 2)^{1/2} / r'_{\frac{1}{2}}$. In the present case, because the

vorticity distribution shown in Figure B-2 has slight asymmetry about the center of the vortex, different values of $r'_{\frac{1}{2}}$ and hence β are obtained for $r' > 0$ and $r' < 0$. Figure B-2 shows the fit of Equation (B8) for $r' > 0$, where $\beta = 16$ per foot, to the measured vorticity distribution over the entire range of r'. Because β was calculated for $r' > 0$, the above distribution fits the measured distribution more closely on the wing-tip side of the rolled-up vortex ($r' > 0$). Considering both the sides, the average value of β is 17.1 per foot, and this value is considered to represent correctly the vorticity distribution over the entire range of r'.

Figure B-4 is a distribution of circumferential velocity along the centerline L_0 as measured by the 5-hole pressure probe. The average core radius (defined as the r' for which V_{θ}, is a maximum) is 0.625 inch, with the maximum circumferential velocities being about 30 percent of the freestream velocity. It can be seen that the distribution is fairly symmetric about the vortex center. This is expected, because the traverse through the rolled-up vortex is in a spanwise direction with respect to the wing and hence any asymmetry which can be caused by the presence of the inboard vortex sheet merging with the rolled-up vortex is not present (Reference 44). The presence of the inboard vortex sheet is discussed more fully later in this Appendix.

The vorticity distribution for the line L_0 is

calculated, using Equation (B3), from the 5-hole pressure probe data and is compared in Figure B-5 with the vortex meter data. Note that the pressure probe vorticity values are divided by the same factor $2\pi/\eta$ as are the vortex meter vorticity values. The factor $2\pi/\eta$ is considered as a constant for these tests behind the wing. The error bands for the pressure probe values were calculated based on the uncertainty ($\pm$ 2.5%) in the velocity values. The figure shows that the comparison is only qualitative because of the fact that large inaccuracies are associated with calculating the velocity derivatives needed for Equation (B3). However, the comparison does serve the purpose of offering evidence that the vortex meter is not insensitive to the small vorticity values at the edges of the wing-tip vortex.

Using the vortex meter measurements, the surface integral in Equation (B4) was evaluated to give the strength of the wing-tip vortex and it was found that the vortex strength, Γ, was 18.5 ft^2/sec. The vortex strength value was also evaluated, using Equation (B5), from the Gaussian distribution fit to the vorticity distribution on the line L_0. It is found that for β = 17.1 per foot, Γ was 19.1 ft^2/sec. Although, the latter method yields a Γ value larger by about three percent, closer inspection reveals that this small increment in the value is not because of vorticity of very small magnitude spreading outside the region C_0.

It is estimated that even though the vorticity outside the region C_0 is spread over a very large area, this does not contribute more than 0.001 percent of the total vortex strength. Hence, it was concluded that the cause of the small discrepancy can be associated with the fact that the Gaussian-fit method assumed that the wing-tip vortex is symmetric, whereas Figure B-3 reveals a slight asymmetry.

Using Equation (B6), line integrals were evaluated to obtain the vortex strength using the 5-hole pressure probe measurements for the circuits C_0 and C_1. The value of Γ obtained for the circuit C_0 (5 inches x 5 inches), which enclosed the region (4 inches x 5 inches) of the vortex meter measurements, was 18.3 ft^2/sec and is well within one percent of the value measured by the vortex meter using Equation (B4). However, when the integral was evaluated for the circuit C_1, the value of Γ obtained was 21.2 ft^2/sec, an increase of about 14% in the vortex strength. It is noted that for this large circuit C_1, any error in velocity is magnified because the length scale is larger for the same number of data points. However, this is not expected to give an increased uncertainty in the Γ value for C_1 in comparison to that for C_0 of more than about 4%. Therefore, it is suspected that the circuit C_1 enclosed more vorticity than circuit C_0. Time did not allow investigation of the region outside circuit C_0 by means of

the vortex meter.

It is suspected that if there is any part of the wing vortex sheet which is not enclosed in the vortex within C_0, this should fall between regions C_0 and C_1. To evaluate this suspicion, a test was made to see in what regions there could possibly be the presence of some vorticity which is not accounted for within the circuit C_0. Firstly, a closer look at the velocity distributions on C_0 and C_1 reveals that the relative concentration of vorticity between C_0 and C_1 is essentially in the region towards the higher surface-pressure side of the wing and also in the region corresponding to the tip of the wing (in Figure B-1, the regions between C_1 and C_0 which are shaded). The authors of reference 44 showed, by means of a sketch, that the inboard vortex sheet which is not rolled-up lies mainly in the above-mentioned regions. Moreover, Chigier and Corsiglia[46] pointed out the possible existence of a secondary vortex (of a smaller strength and core but rotating in the same direction as the main vortex) in the tip region of the wing. Spreiter and Sacks[45] provided an estimation for the roll-up of the vortex sheet behind an elliptic wing and concluded that it may take 8 to 10 chord lengths for the vortex sheet to become completely rolled-up. Recent velocity measurements made by Sampson[49] showed that, besides the presence of a well-defined and approximately axisymmetric

wing-tip vortex, significant amounts of vorticity can be found in the non-rolled-up vortex sheet five chords downstream of a lifting wing. The measurements in the present tests were made at 3.8 chord lengths behind the wing trailing edge because of the limitation on the length of the flat plate upon which the wing was mounted. Thus, it is reasonable to assume that the circuit C_1 contained more vorticity than the circuit C_0. The good agreement between the vortex strength obtained by using the vortex meter and the circulation obtained from the velocity measurements, for the same region bounded by the circuit C_0, leads to the conclusion that the vortex strength obtained with the vortex meter is reasonably accurate if the area coverage extends out to at least a value of N equal to 1 CPS. It is also concluded that the predicted performance and the frictional constant provided by the meter manufacturer are satisfactory.

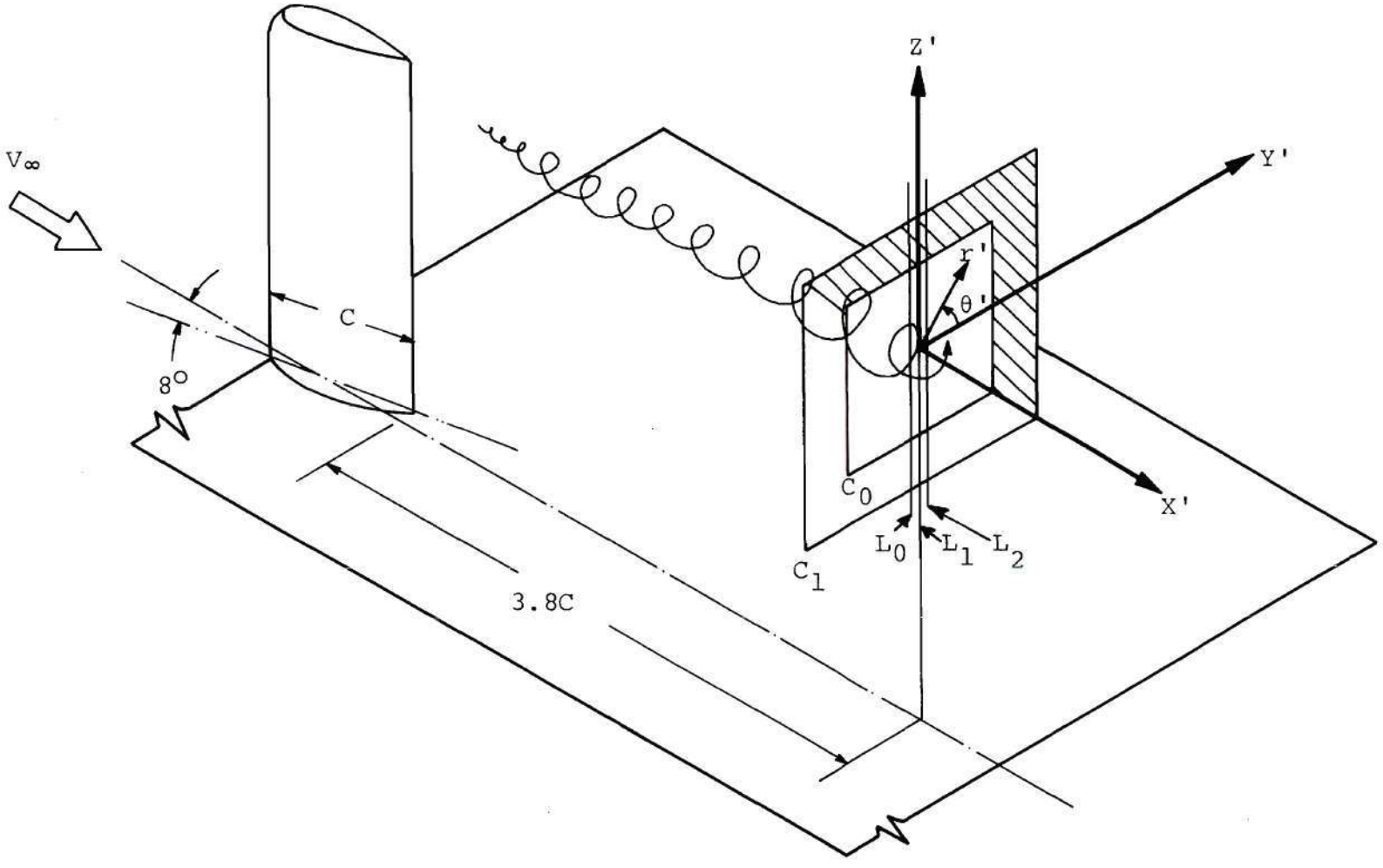

Figure B-1. Areas of Measurement and Axis System for Wing Trailing Vortex.

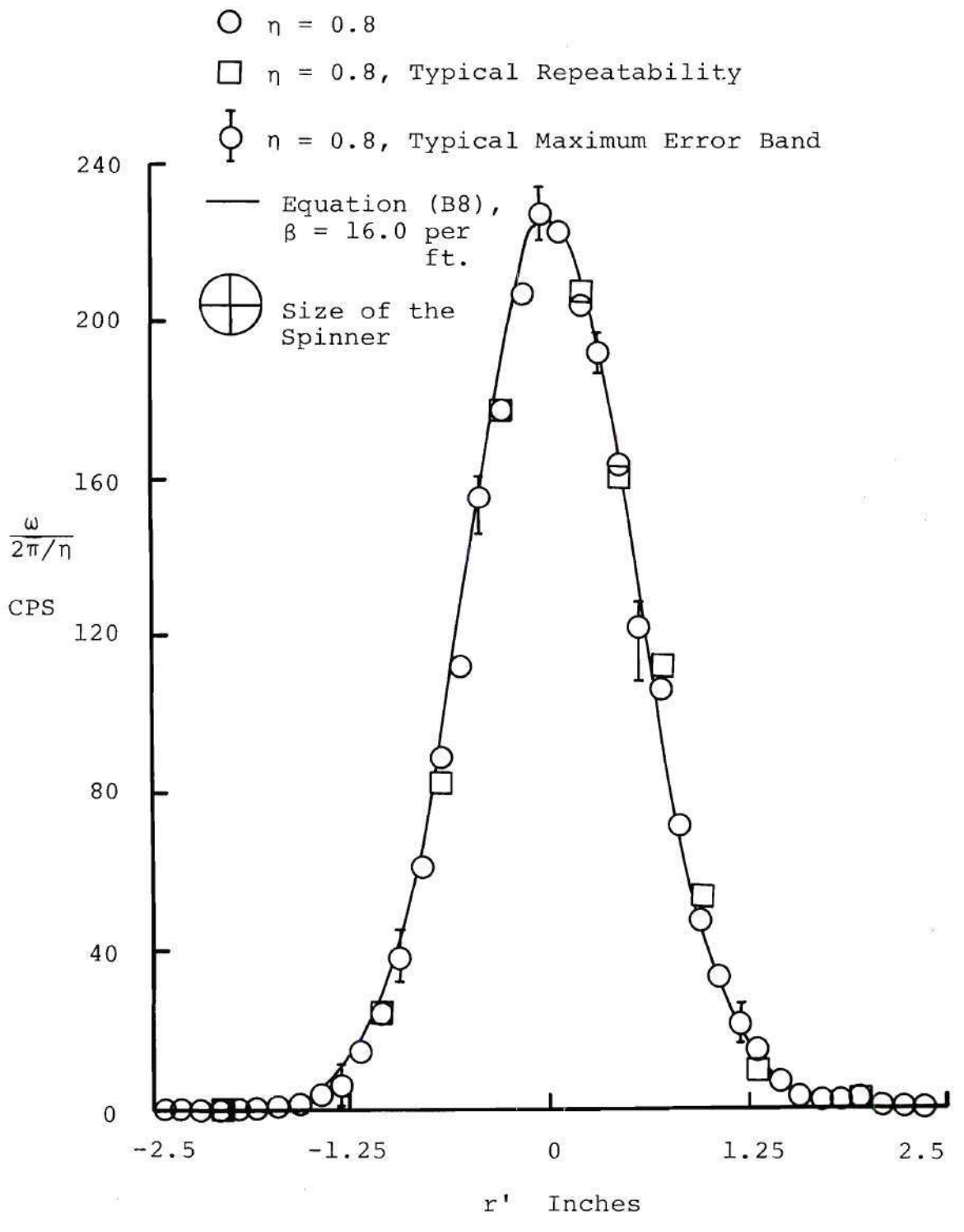

Figure B-2. Vorticity Distribution for Line L_0 Passing Through Vortex Center - Vortex Meter Data.

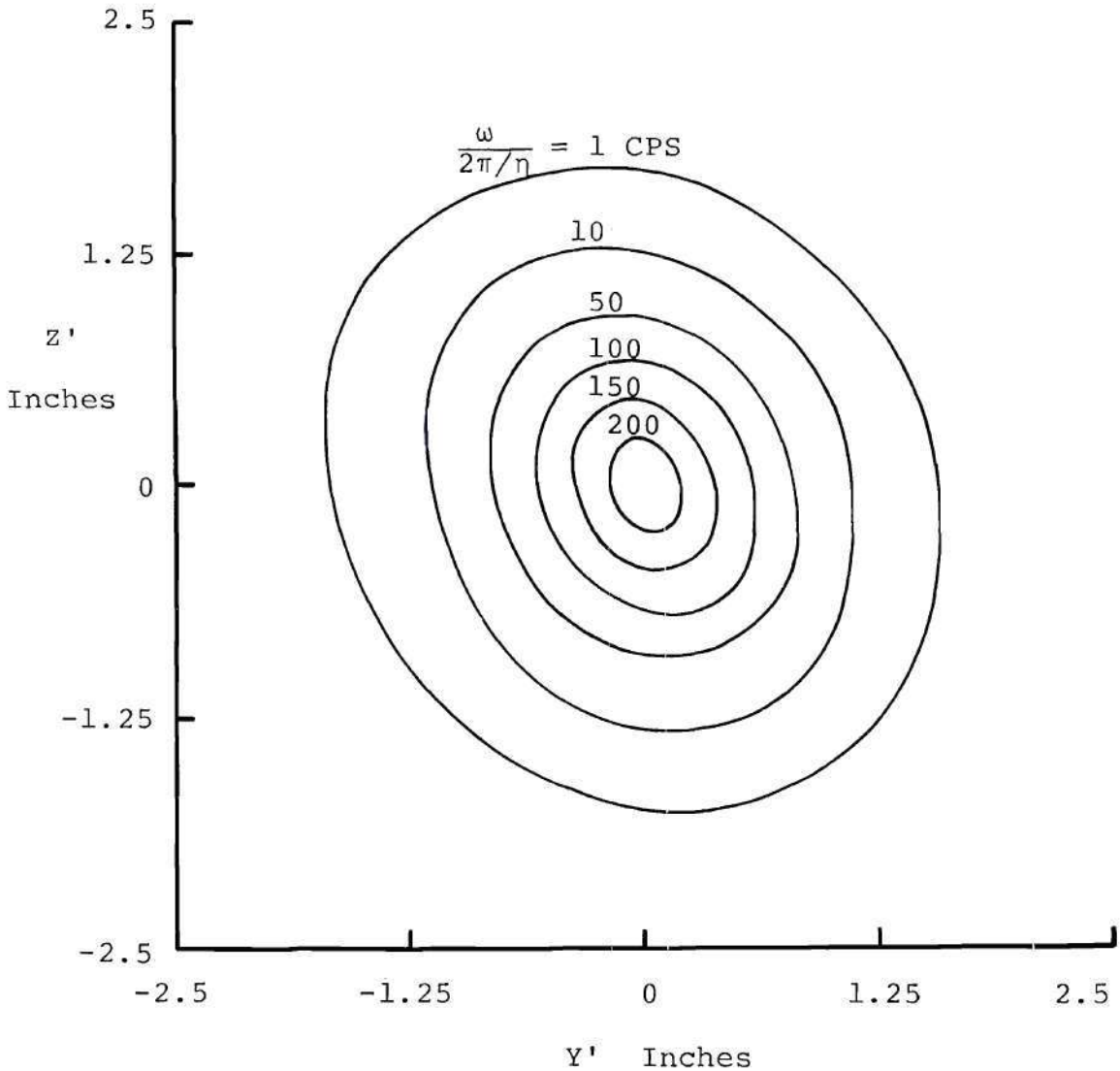

Figure B-3. Contours of Constant Vorticity for Wing Trailing Vortex.

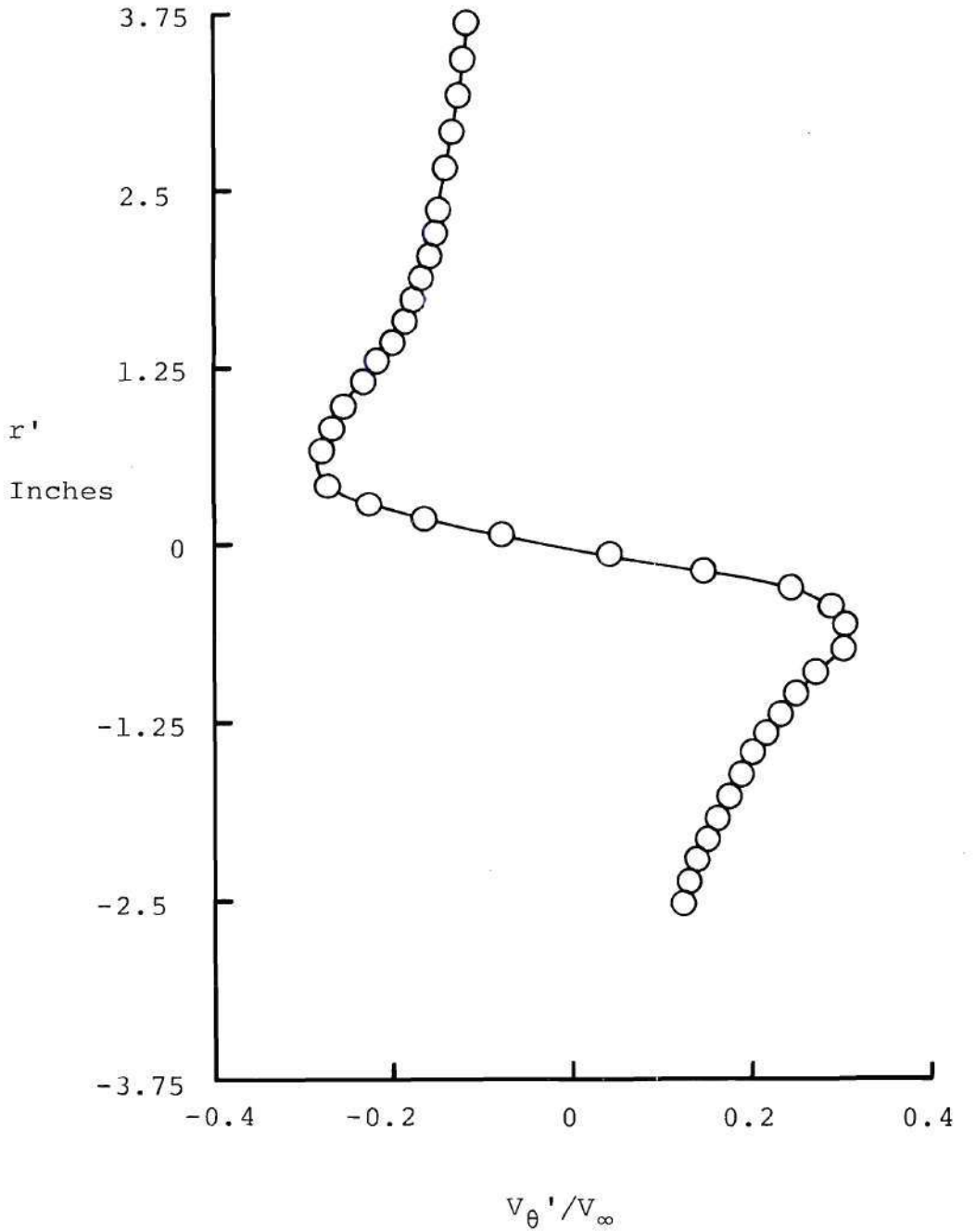

Figure B-4. Circumferential Velocity Distribution Along a Traverse Through Vortex Center.

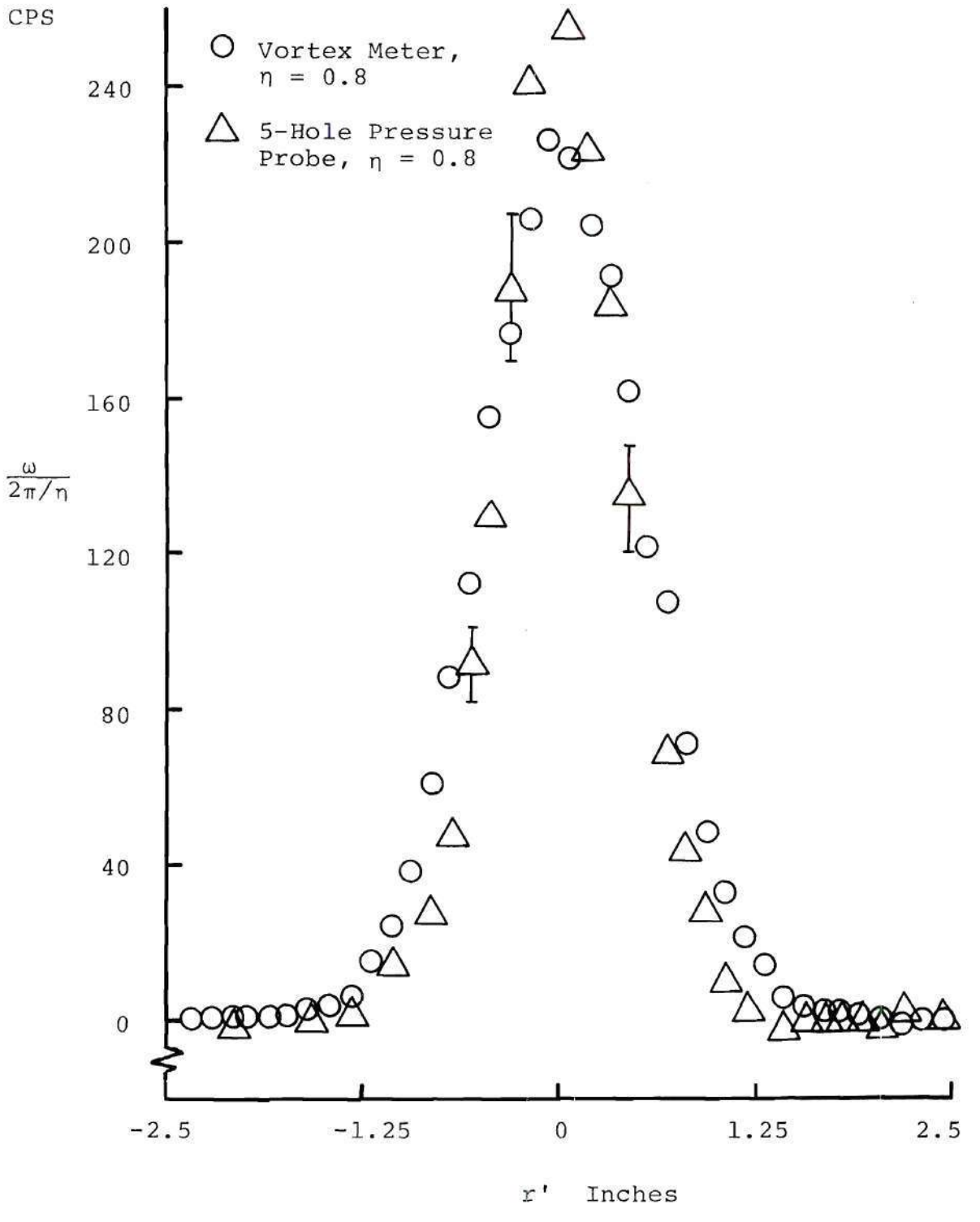

Figure B-5. Comparison of Vorticity Distribution - Vortex Meter Data versus 5-Hole Pressure Probe Data.

APPENDIX C

THE BEHAVIOR OF THE STREAMLINED JET IN CROSSFLOW

The behavior of the streamlined jet was determined from temperature measurements, and the results are discussed in this Appendix. A comparison of the behavior of the streamlined jet with that of the circular jet is made.

Temperature Centerline

Recall that for the circular jet it was observed that the temperature centerlines did not coincide with the jet centerlines. For the streamlined jet, it was found that such is not the case. As is seen in Figure C-1, the temperature and the jet centerlines are very close to one other for the streamlined jet.

Figure C-2 shows the decay of total pressure (as obtained from reference 8) along the total pressure centerline (s/d) compared to the decay of the temperature along the temperature centerline (s_T/d) for both the circular and the streamlined jet. As might be expected, the decay (of both P_o and T) for the streamlined jet is less than that for the circular jet because of greater penetration by the streamlined jet. Furthermore, the temperature in both the jets seems to decay at a lower rate than the total pressure.

Extent and Shape of Streamlined Jet

Figure C-3 illustrates the extent and shape of the streamlined jet for a cross section in the plane of symmetry. A comparison of this figure with the corresponding symmetry-plane behavior of the circular jet as given in Figure 22 reveals some differences. In the case of the streamlined jet, the shape of the temperature core is different than that of the circular jet, having a flat tip rather than a sharp conical shape. The length of the core is slightly smaller in the streamlined jet case than in the circular jet case. Also, it is observed that the mixing, at least near the plane of symmetry, is more intense in the downstream regions of the streamlined jet, and a much larger "hump" is present in the contours. If the cross sections of the streamlined jet in the Y-Z plane are studied, Figures C-4(a) through C-4(c), it can be seen that the streamlined jet has a distinct, thin region in the rear of the jet and near the flat plate surface. Such a region persists at least up to $X/d = 3.5$, and later ($X/d = 7.5$) the thin region vanishes as shown in Figure C-4(c). At $X/d = 7.5$, the cross-sectional shape of the streamlined jet in the Y-Z plane is not very different from that of the circular jet.

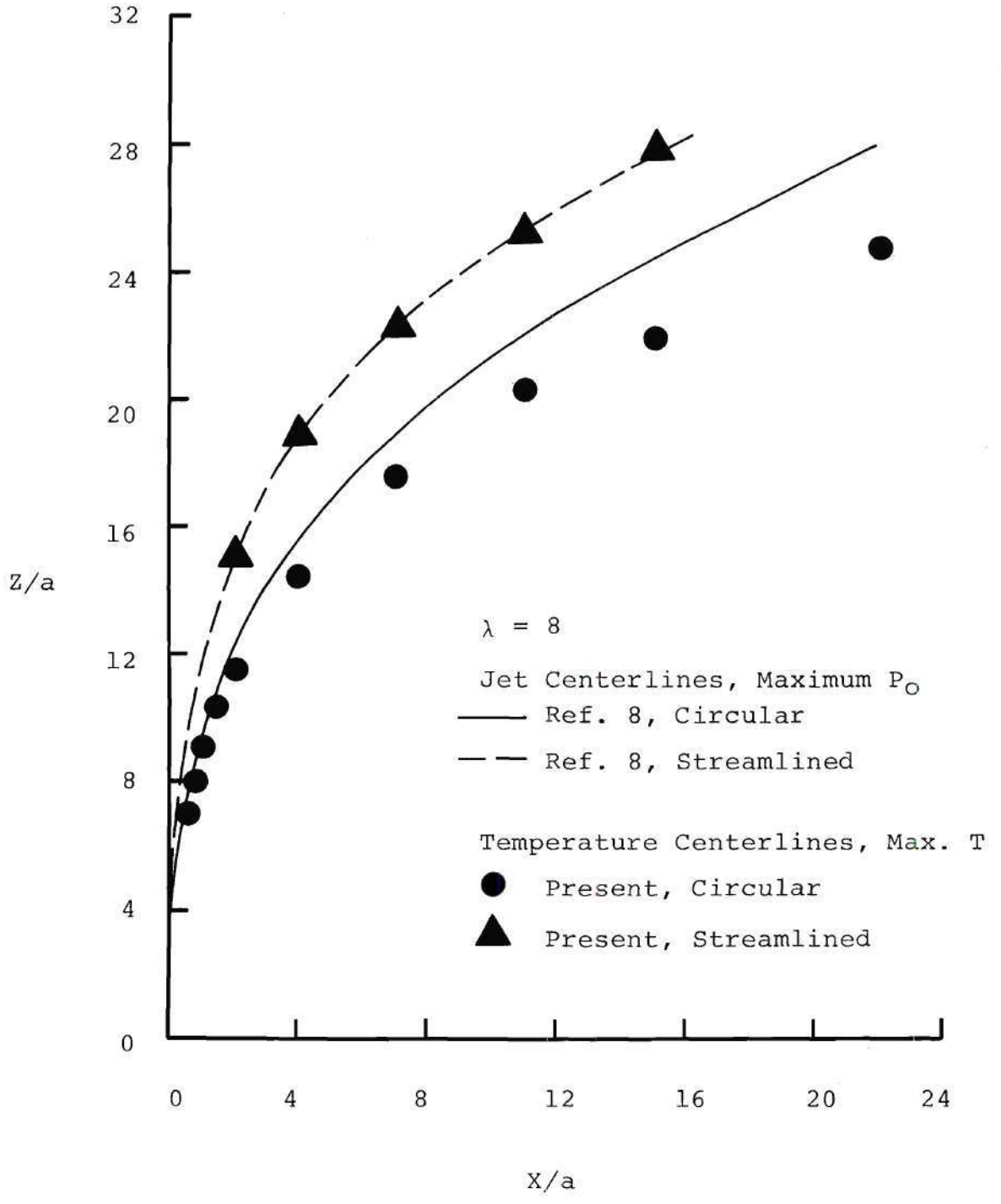

Figure C-1. Temperature Centerlines - Circular versus Streamlined Jet.

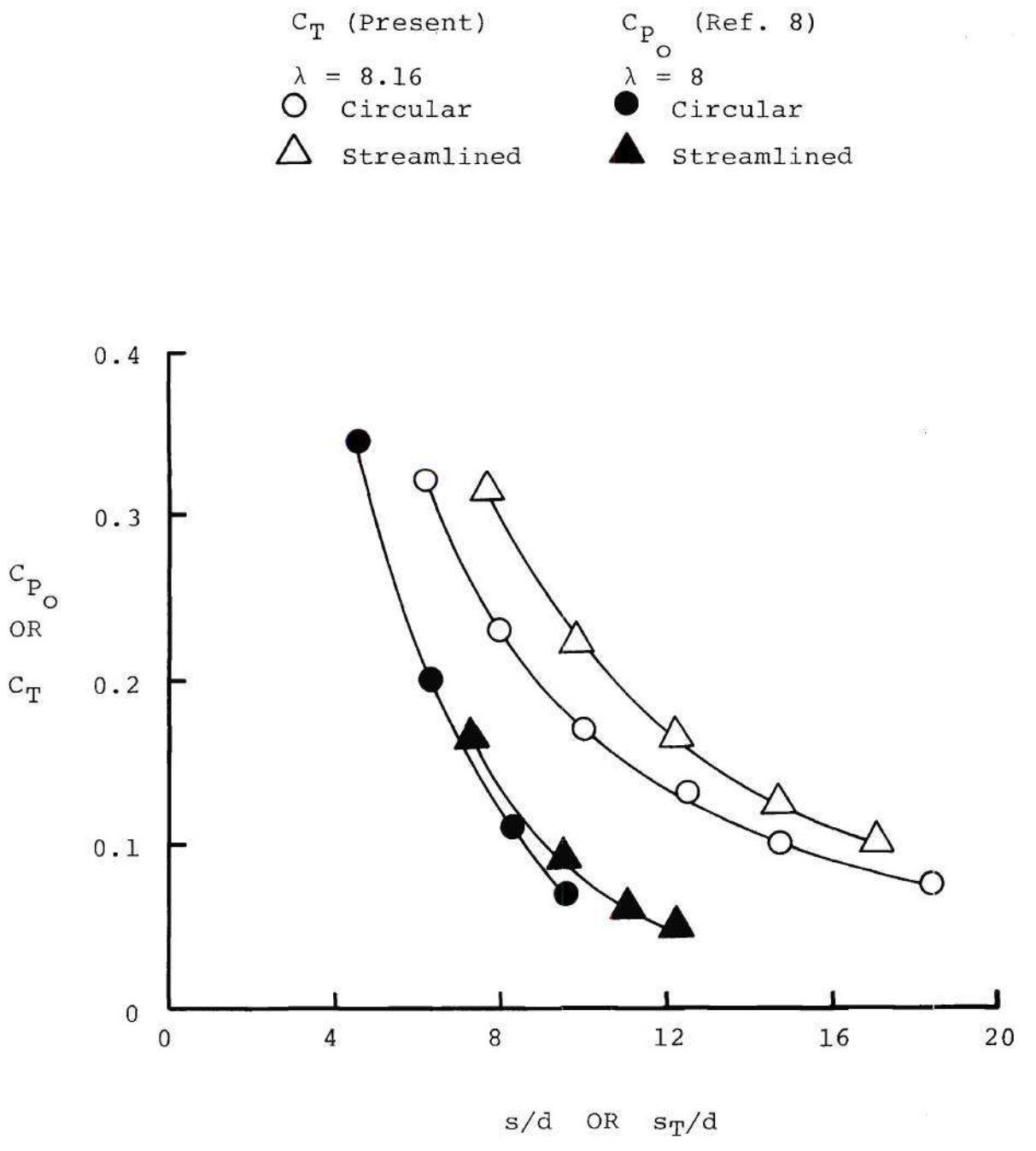

Figure C-2. Decay of Total Pressure and Temperature for Circular and Streamlined Jet.

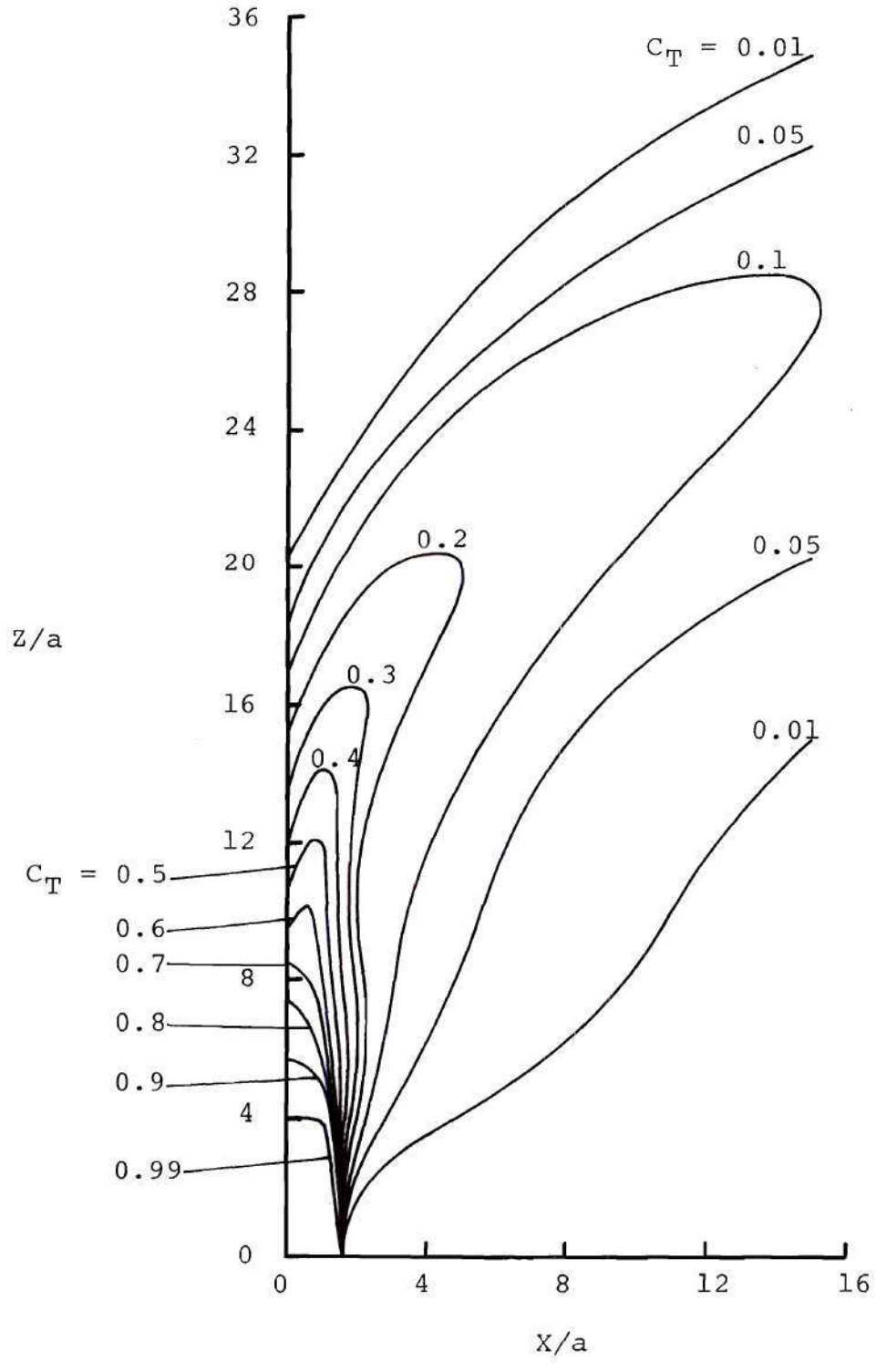

Figure C-3. Contours of C_T in the Plane of Symmetry for Streamlined Jet, λ = 8.16.

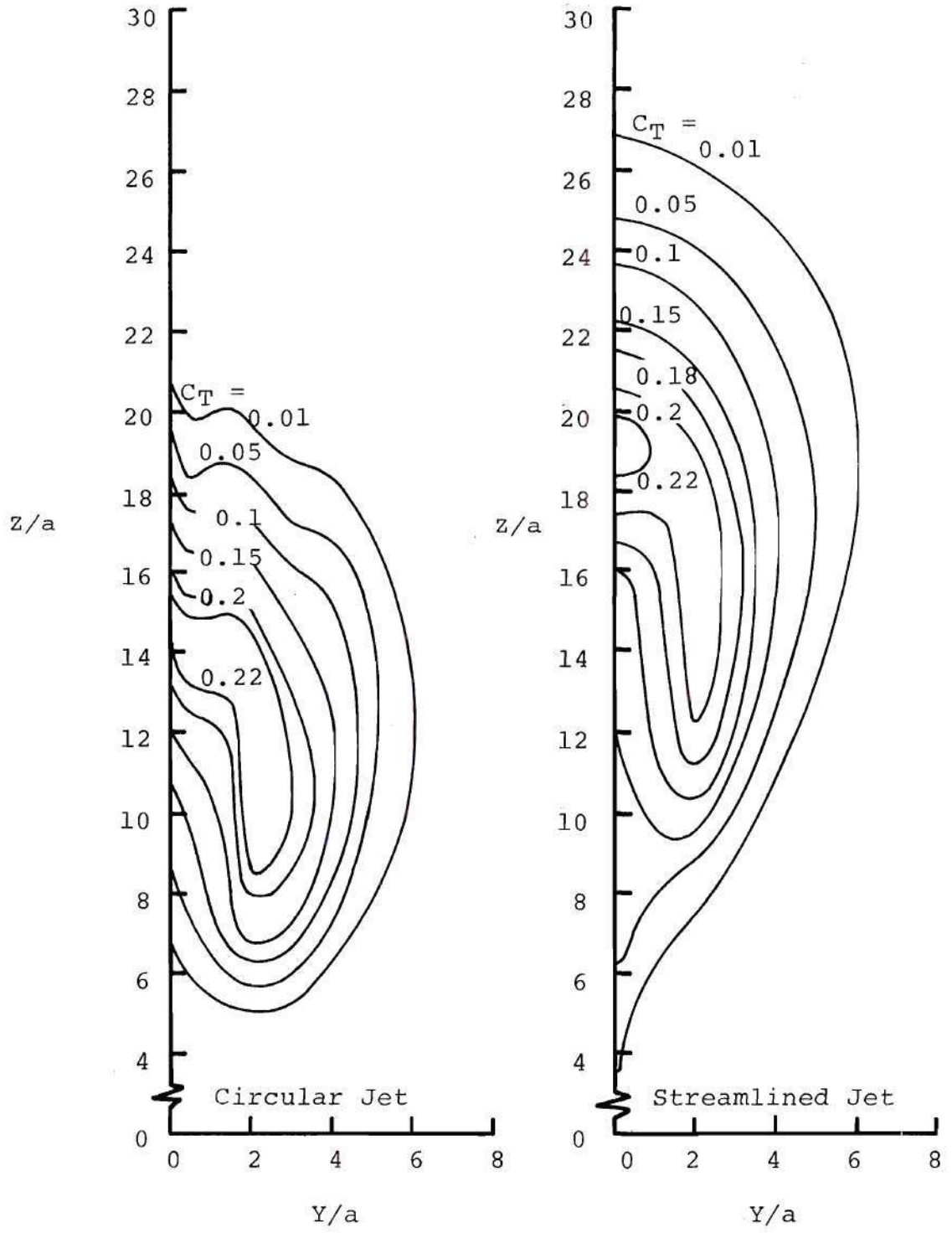

(a) X/d = 2.0

Figure C-4. Contours of C_T in Y-Z Plane for Circular and Streamlined Jet, λ = 8.16.

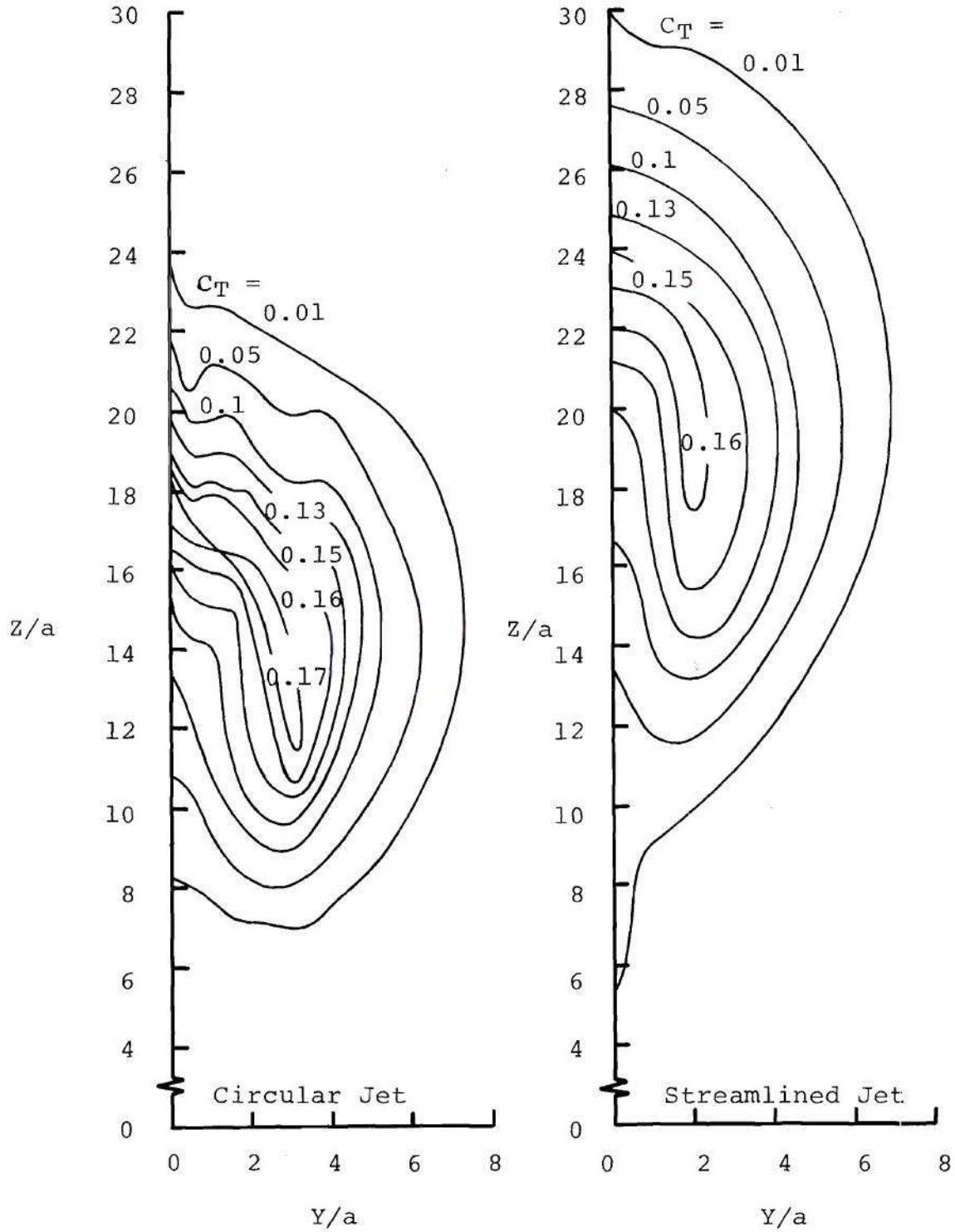

(b) X/d = 3.5

Figure C-4. Contours of C_T in Y-Z Plane for Circular and Streamlined Jet, λ = 8.16 (Continued).

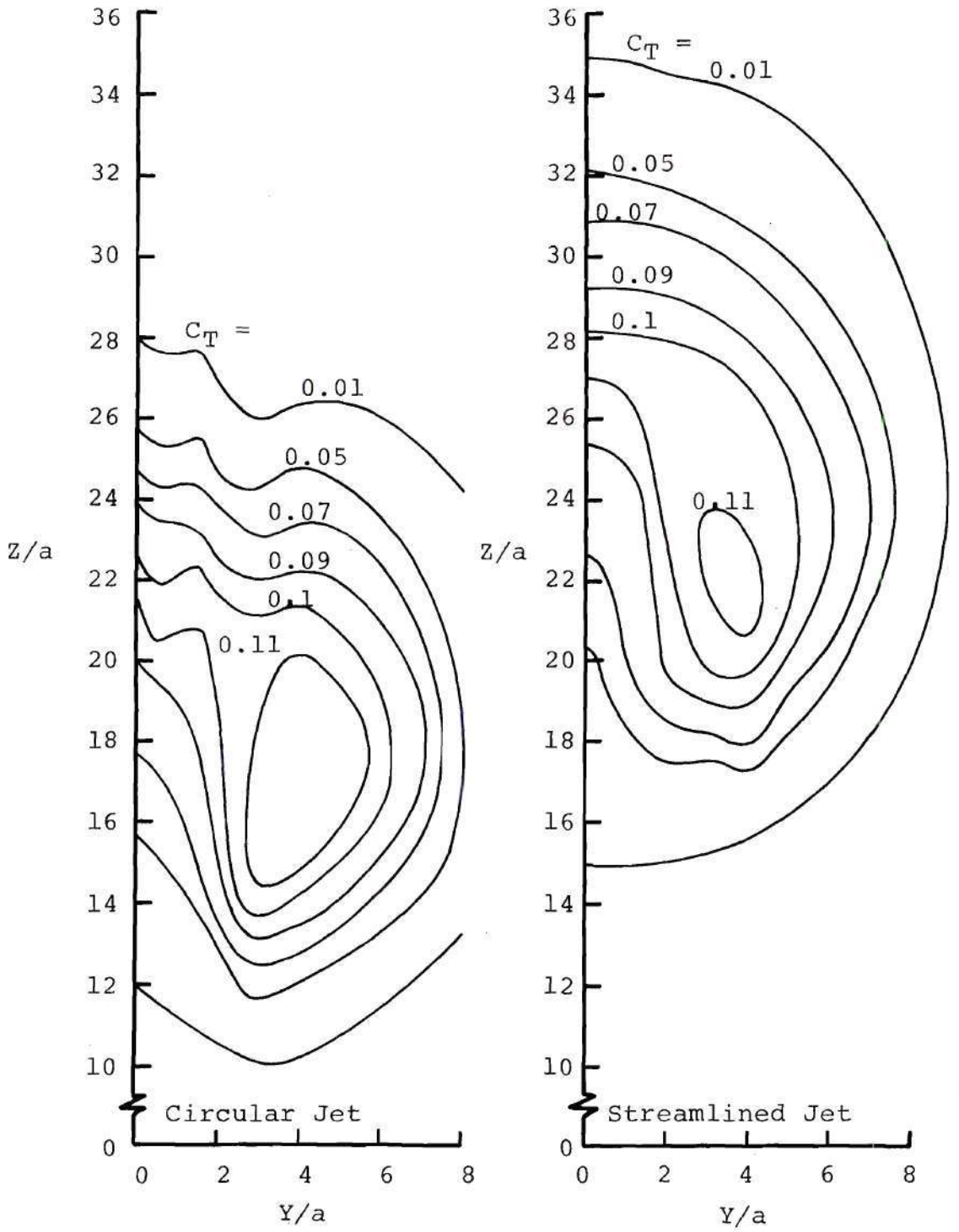

(c) X/d = 7.5

Figure C-4. Contours of C_T in Y-Z Plane for Circular and Streamlined Jet, λ = 8.16 (Concluded).

LITERATURE CITED

1. Williams, J. and Wood, M. N., "Aerodynamic Interference Effects with Jet-Lift V/STOL Aircraft under Static and Forward-Speed Conditions," Zeitschrift fur Flugwissenshaften, Vol. 15, No. 7, July 1967, pp. 237-256.

2. Margason, R. J., "Jet-Induced Effects in Transition Flight," SP-116, April 1966, NASA.

3. Carter, A., "Effects of Jet-Exhaust Location on the Longitudinal Aerodynamic Characteristics of a Jet V/STOL Model," TN D-5333, July 1969, NASA.

4. Mikolowsky, W. T., "An Experimental Investigation of a Jet Issuing from a Wing in Crossflow," Ph.D. Thesis, May 1972, Georgia Institute of Technology.

5. Vogler, R. D., "Surface Pressure Distribution Induced on a Flat Plate by a Cold Air Jet Issuing Perpendicularly from the Plate and Normal to a Low Speed Free Stream Flow," TN D-1629, March 1963, NASA.

6. Bradbury, L. J. S. and Wood, M. N., "The Static Pressure Distribution Around a Circular Jet Exhausting Normally from a Plane Wall into an Airstream," Tech. Note No. Aero 2978, August 1964, British Royal Aircraft Establishment.

7. Gelb, G. H. and Martin, W. A., "An Experimental Investigation of the Flow Field about a Subsonic Jet Exhausting into a Quiescent and a Low Velocity Air Stream," Canadian Aeronautics and Space Journal, Vol. 12, No. 8, October 1966, pp. 333-342.

8. Mosher, D. K., "An Experimental Investigation of a Turbulent Jet in a Cross Flow," Ph.D. Thesis, December 1970, Georgia Institute of Technology.

9. McMahon, H. M. and Mosher, D. K., "Experimental Investigation of Pressures Induced on a Flat Plate by a Jet Issuing into a Subsonic Crosswind," Analysis of a Jet in a Subsonic Crosswind, SP-218, September 1969, NASA.

10. Wright, M. A., "A Two-Dimensional Representation of the Crosswind for the Jet Interference Problem," Ph.D. Thesis, June 1970, Georgia Institute of Technology.

11. Wu, J. C. and Wright, M. A., "A Blockage-Sink Representation of Jet Interference Effects for Noncircular Jet Orifices," Analysis of a Jet in a Subsonic Crosswind, SP-218, September 1969, NASA.

12. Wooler, P. T., "Development of an Analytical Model for the Flow of a Jet into a Subsonic Crosswind," Analysis of a Jet in a Subsonic Crosswind, SP-218, September 1969, NASA.

13. Wooler, P. T., "On the Flow Past a Circular Jet Exhausting at Right Angles from a Flat Plate or a Wing," Journal of the Royal Aeronautical Society, Vol. 71, March 1967, pp. 216-218.

14. Callaghan, E. E. and Ruggeri, R. S., "Investigation of the Penetration of an Air Jet Directed Perpendicularly to an Air Stream," TN 1615, June 1948, NACA.

15. Callaghan, E. E. and Bowden, D. T., "Investigation of Flow Coefficients of Circular, Square, and Elliptical Orifices at High Pressure Ratios," TN 1947, September 1949, NACA.

16. Ruggeri, R., Callaghan, E., and Bowden, D., "Penetration of Air Jets Issuing from Circular, Square, and Elliptical Orifices Directed Perpendicularly to an Air Stream," TN 2019, February 1950, NACA.

17. Chassaing, P., George, J., Claria, A., and Sananes, F., "Physical Characteristics of Subsonic Jets in a Cross-Stream," Journal of Fluid Mechanics, Vol. 62, Part 1, January 1974, pp. 41-64.

18. Platten, J. L. and Keffer, J. F., "Entrainment in Deflected Axisymmetric Jets at Various Angles to the Stream," UTME-TP 6808, June 1968, University of Toronto.

19. Endo, H., "A Working Hypothesis for Predicting the Path and Induced Velocity of a Jet Exhausting at a Large Angle into a Uniform Cross-Flow," Transactions of the Japan Society for Aeronautical and Space Sciences, Vol. 17, No. 36, 1974, pp. 45-64.

20. Hardy, W. G., "Non-Parallel Flow Interactions," M.A.E. Thesis, 1967, University of Virginia.

21. Jordinson, R., "Flow in a Jet Directed Normal to the Wind," R & M 3074, October 1956, British Aero. Res. Council.

22. Gordier, R., "Studies of Fluid Jets Discharging Normally into Moving Liquid," Technical Paper No. 28, Series B, 1959, St. Anthony Falls Hydro Lab, University of Minnesota.

23. Kamotani, Y. and Greber, I., "Experiments on a Turbulent Jet in a Cross Flow," FTAS/TR-71-62, June 1971, Case Western Reserve University.

24. Reilly, R. S., "Investigation of the Deformation and Penetration of a Turbulent, Subsonic Jet Issuing Transversely into a Uniform, Subsonic Main Stream," Ph.D. Thesis, 1968, University of Maryland.

25. Crawford, R. A., "A Combined Potential and Momentum Roll-Up Model for the Jet in Cross-Flow," Ph.D. Thesis, August 1971, University of Tennessee.

26. Pratte, B. D. and Baines, W. D., "Profiles of the Round Turbulent Jet in a Cross Flow," Journal of the Hydraulics Division, Proceedings of the ASCE, Vol. 92, No. HY6, November 1967, pp. 53-64.

27. Tipping, J. C., "The Induced Flow Effects of a Round Turbulent Jet Issuing Normally from a Flat Plate into a Mainstream Parallel to the Plate," Ph.D. Thesis, 1965, University of Bristol.

28. Endo, H., "Theory and Experiments on the Turbulent Round Jet in a Cross Wind," Private Communication, National Aerospace Laboratory, Tokyo, Japan.

29. Thompson, A. M., "The Flow Induced by Jets Exhausting Normally from a Plane Wall into an Airstream," Ph.D. Thesis, September 1971, University of London.

30. Fearn, R. and Weston, R. P., "Vorticity Associated with a Jet in a Cross Flow," AIAA Journal, Vol. 12, No. 12, December 1974, pp. 1666-1671.

31. Sellers, W. L., "A Model for the Vortex Pair Associated with a Jet in a Crossflow," CR-136756, 1975, NASA.

32. Margason, R. J. and Fearn, R., "Jet Wake Characteristics and Their Induced Aerodynamic Effects on V/STOL Aircraft in Transition Flight," Analysis of a Jet in a Subsonic Crosswind, SP-218, September 1969, NASA.

33. Crowe, C. T. and Riesebieter, H., "An Analytical and Experimental Study of Jet Deflection in a Cross-Flow," Fluid Dynamics of Rotor and Fan Supported Aircraft at Subsonic Speeds, Paris: Advisory Group for Aerospace Research and Development Preprint, 1967.

34. Keffer, J. F. and Baines, W. D., "The Round Turbulent Jet in a Cross Wind," Journal of Fluid Mechanics, Vol. 15, Part 4, 1963, pp. 481-496.

35. McAllister, J. D., "A Momentum Theory for the Effects of Cross Flow on Incompressible Turbulent Jets," Ph.D. Thesis, August 1968, University of Tennessee.

36. Fan, L. N., "Turbulent Buoyant Jets into Stratified or Flowing Ambient Fluids," Rep. No. KH-R-15, 1967, Keck Hyd. Lab., California Institute of Technology.

37. Butkewicz, P. J., "An Investigation of the Vortex Wake and Induced Entrainment for a Jet in Low Reynolds Number Cross Flow," Ph.D. Thesis, August 1970, University of Tennessee.

38. Soukup, S. M., "Potential Flow Aspects of the Cross-Sectional Deformation of Jet Configurations in Cross-Flow," M.S. Thesis, December 1968, University of Tennessee.

39. McMahon, H. M., Hester, D. D., and Palfery, J. G., "Vortex Shedding from a Turbulent Jet in a Cross-Wind," Journal of Fluid Mechanics, Vol. 48, Part 1, 1971, pp. 73-80.

40. Owen, P. R., "Decay of a Turbulent Trailing Vortex," Aeronautical Quarterly, Vol. XXI, February 1970.

41. Squire, H. B., "The Growth of a Vortex in Turbulent Flow," Aeronautical Quarterly, Vol. XVI, August 1965.

42. May, D. M., "The Development of a Vortex Meter," M.S. Thesis, June 1964, Pennsylvania State University.

43. McCormick, B. W. and Surendraiah, M., "A Study of Rotor Blade-Vortex Interaction," Presented at the 26th Annual National Forum of the American Helicopter Society (Washington, D.C.), June 1970.

44. Rorke, J. B. and Moffitt, R. C., "Wind Tunnel Simulation of Full Scale Vortices," CR-2180, March 1973, NASA.

45. Spreiter, J. R. and Sacks, A. H., "The Rolling Up of the Trailing Vortex Sheet and Its Effect on the Downwash Behind Wings," Journal of the Aeronautical Sciences, January 1951.

46. Chigier, N. A. and Corsiglia, V. R., "Tip Vortices-Velocity Distributions," Presented at the 27th Annual National V/STOL Forum of the American Helicopter Society (Washington, D.C.), May 1971.

47. Wu, J. C., McMahon, H. M., Mosher, D. K., and Wright, M. A., "Experimental and Analytical Investigation of Jets Exhausting into a Deflecting Stream," Presented at AIAA/AHS VTOL Research, Design, and Operations Meeting (Atlanta, Ga.), February 1969.

48. "Flows with Large Velocity Fluctuations," Film No. 575, O.N.E.R.A., France.

49. Sampson, R. G., "An Experimental and Theoretical Investigation of the Structure of a Trailing Vortex Wake," Aeronautical Quarterly, February 1977.

50. Moussa, J. M., Trischka, J. W., and Eskinazi, S., "The Near Field in the Mixing of a Round Jet with a Cross-Stream," Journal of Fluid Mechanics, Vol. 80, Part 1, 1977, pp. 49-80.

VITA

Dharmanshu L. Antani was born in India on October 2, 1946. After completing his elementary and high school education, Mr. Antani entered the Sardar Patel University, Vallabh Vidyanagar, in 1962 and received his Bachelor of Engineering (Mechanical) with Distinction in 1967. He entered the Indian Institute of Science, Bangalore, in 1967 and received his Master of Engineering (Aeronautical) in 1969. In September, 1969, Mr. Antani entered the doctoral program in Aerospace Engineering at the Georgia Institute of Technology. He served as a graduate research assistant while pursuing his studies, and was appointed as an Assistant Research Engineer in the School of Aerospace Engineering during the period January, 1976 to October, 1976.

Mr. Antani married the former Vandana Vaishnav on April 2, 1977.